UNIVERSIDAD DEL PAÍS VASCO
EUSKAL HERRIKO UNIBERTSITATEA

Department of Physics

CAMPUS OF INTERNATIONAL EXCELLENCE

Layered Transition Metal Oxides: Magnetic Properties and Excitations

Thesis by

Mikel Arruabarrena Larrarte

Supervised by

Prof. Andrés Ayuela Fernández

and

Dr. Aritz Leonardo Liceranzu

Donostia-San Sebastián, March 2023

Contents

Resumen **1**

I Magnetic properties of layered oxides **5**

1 Introduction **7**

2 Numerical Methods **13**
2.1 The Quantum Many-Body Problem 13
2.1.1 The Born-Oppenheimer Approximation 14
2.1.2 Hartree-Fock method 15
2.2 Density Functional Theory 16
2.2.1 Hohenberg-Kohn Theorems 16
2.2.2 Kohn-Sham ansatz 17
2.2.3 Exchange and correlation functionals: LDA and GGA . . . 18
2.2.4 Spin in DFT 20
2.2.5 Strongly correlated systems: DFT+U method 20
2.3 Magnetic Properties From First-Principles 23
2.3.1 Magnetic Ordering and Ground State 23
2.3.2 Spin-orbit coupling and MAE 24

3 Magnetic Properties of Bulk Ilmenite $CoTiO_3$ **27**
3.1 Theoretical Details 28
3.1.1 Chemical and magnetic structures of $CoTiO_3$ 28
3.1.2 Computational methodology 29
3.2 Magnetic ordering 30
3.3 Magnetic anisotropy 33
3.3.1 Conclusions 36

4 Characterization of the 3d Transition Metal Ilmenenes **37**
4.1 Theoretical details 38
4.2 Crystalline structure and distortions 39
4.3 Electronic properties: magnetic semiconductors 41
4.4 Magnetism 43
4.4.1 Magnetic Order 43

4.4.2 Magnetic Anisotropy 44
4.5 Conclusions 46

5 Strain-induced magnetic anisotropy transitions in layered $CaMn_2Bi_2$ 47
5.1 Numerical details 48
5.2 Magnetic order 48
5.3 Strain-induced magnetic anisotropy change 50
5.4 Conclusions 51

II Excitons in TDDFT 53

6 Introduction 55

7 Numerical Methods 59
7.1 Time Dependent Density Functional Theory 59
7.2 Linear Response TDDFT 60
7.2.1 Dyson equation: optical absorption 61
7.2.2 Casida equation: excitation energies 63
7.2.3 f_{xc} kernel and excitons 64
7.3 Excitation energies beyond TDDFT 65

8 Direct calculation of exciton binding energies from first-principles 67
8.1 TDDFT approach: LRC kernel 67
8.2 Hybrid TDDFT 71
8.2.1 Wigner-Seitz truncation of the kernel 71
8.3 Conclusions 75

Conclusions and Outlook 77

Appendices

A $CoTiO_3$: All-electron test for the band structure 81

B $CoTiO_3$: Convergence of the MAE 83

C $CoTiO_3$: Effect of U in the MAE 85

D $CoTiO_3$: Orbital moment and non-collinearity 87

E TM Ilmenenes: PDOS and band structures 89

F EXCITONS: Computation of the Correction Terms C_{cv} 97

List of publications 99

Bibliography **101**

RESUMEN

La investigación de las propiedades fundamentales de los materiales es un pilar imprescindible en el desarrollo de la ciencia. Para crear dispositivos con nuevas e interesantes aplicaciones es necesario un conocimiento profundo de los materiales que los componen. En la actualidad, en los laboratorios del mundo se producen e investigan nuevos materiales diariamente, y este proceso necesita inevitablemente un estudio teórico que dé explicación a los fenómenos físicos observados. Los modelos teóricos, además de ayudar comprender las mediciones, también sirven para generalizar las observaciones y hacer predicciones, ayudando en la búsqueda de nuevos materiales. No hay que olvidar el trabajo y el coste de producir nuevos compuestos en el laboratorio, y en este sentido, las simulaciones computacionales facilitan considerablemente este proceso, proponiendo materiales con propiedades de interés. En los últimos años, la creación de métodos computacionales eficientes, junto con el desarrollo de la tecnología, permite calcular con gran precisión las propiedades de los nuevos materiales. En este contexto, es imprescindible desarrollar y testear estas herramientas.

Esta tesis tiene como objetivo el estudio de las propiedades magnéticas y ópticas de diversos materiales semiconductores. Siguiendo esta temática, el análisis se ha dividido en dos partes: (i) estudio de las propiedades magnéticas de los óxidos semiconductores compuestos por capas, y (ii) cálculo de las energías de unión de los excitones en sólidos semiconductores y aislantes. A continuación, se resume la estructura de la tesis.

En la primera parte, analizaremos las propiedades magnéticas de los óxidos compuestos por capas. Nuestro objetivo es hacer una descripción detallada del magnetismo de estos materiales para reforzar las mediciones experimentales actuales y dar una base teórica sólida a los experimentos futuros. Los resultados que presentamos están disponibles en las referencias bibliográficas [1, 2].

- En el capítulo 1, haremos una introducción general al magnetismo, destacando su origen electrónico y su importancia en la nanotecnología. En esta parte de la tesis se presentan también los materiales que serán objeto de estudio, revisando para ello algunos estudios experimentales realizados hasta la fecha.

- En el capítulo 2, presentamos el método numérico que utilizaremos para calcular las propiedades magnéticas: la teoría del funcional de la densidad (Density Functional Theory, DFT, en inglés). La base de este método es calcular el estado electrónico fundamental de un sistema de muchos cuerpos, utilizando para ello un sistema equivalente formado por partículas que no interactúan, y que tiene la misma densidad que el sistema original. Presentaremos también el método DFT+U, que es una adición a la DFT que tiene como objetivo corregir la excesiva delocalización electrónica que esta produce al aplicarse en los sistemas con una correlación electrónica alta. Para conseguir esto, la interacción Coulomb entre orbitales electrónicos de tipo d se corrige mediante la adición de un parámetro de U de tipo Hubbard. A continuación, explicamos el procedimiento para calcular las propiedades magnéticas de los materiales y cómo calcular la interacción de intercambio (exchange coupling, en inglés). Por último, presentamos la interacción espín-órbita y el concepto de anisotropía magnética.

- En el capítulo 3, estudiamos el mineral de ilmenita $CoTiO_3$ [1]. El titanato de cobalto es un material que recientemente ha generado mucho interés, ya que presenta numerosas propiedades físicas de interés. En especial, las propiedades topológicas de este material son las que más han llamado la atención, ya que en el titanato de cobalto presenta magnones de tipo Dirac. Esto convierte este material en un compuesto de gran interés en el campo de la espintrónica, pues podría emplearse para inyectar magnones en otros compuestos. En este capítulo, dentro del formalismo GGA+U, hemos calculado el estado magnético fundamental del material, obteniendo la estructura G-AFM que se ha observado experimentalmente. También hemos compuesto un diagrama de sus transiciones de fase en función de la temperatura, demostrando que el titanato de cobato tiene dos temperaturas críticas. A continuación, hemos realizado cálculos que tienen en cuenta la interacción spin-órbita, concluyendo que la anisotropía magnética cristalina del $CoTiO_3$ es perpendicular al plano hexagonal. En un principio, este hallazgo parece contradecir los datos experimentales, pero tras calcular otras contribuciones que influyen en la anisotropía, hemos descubierto que el dopaje del titanato de cobalto puede provocar que la anisotropía pase a estar en el plano, como se observa en los experimentos.

- En el capítulo 4, analizamos las propiedades estructurales, electrónicas y magnéticas [2] de los materiales magnéticos bidimensionales tipo ilmeneno basados en metales de transición $3d$. El ilmeneno de hierro es un material magnético bidimensional que se exfolió recientemente del mineral de la ilmenita basada en el hierro. Siguiendo la línea iniciada en el capítulo anterior, y teniendo en cuenta que las estructuras de la ilmenita de hierro y el titanato de cobalto son muy similares, en este capítulo analizaremos toda la familia de ilmenenos $TMTiO_3$ (siendo TM = V, Cr, Mn, Fe, Co, Ni,

Cu, Zn los metales de transición $3d$). Con el formalismo GGA+U, hemos calculado la estructura cristalina relajada de cada material, desarrollado un modelo de llenado de niveles electrónicos para los electrones $3d$, y calculado el estado magnético fundamental y la anisotropía magnética. Hemos llegado a la conclusión de que la mayoría de los ilmenenos son antiferromagnéticos por capas, y que la anisotropía magnética está fuera del plano (en el plano) cuando la capa $3d$ está por debajo (encima) de la mitad del llenado.

- En el capítulo 5, estudiamos las propiedades magnéticas del compuesto semiconductor y antiferromagnético $CaMn_2Bi_2$. Siguiendo el procedimiento de los capítulos 3 y 4, calculamos el estado magnético básico y la anisotropía del material. En $CaMn_2Bi_2$, los átomos de manganeso están organizados de forma antiferromagnética y los momentos magnéticos se alinean dentro del plano. En este capítulo también se ha estudiado como la de la deformación de la celda influye en el magnetismo, y encontramos que la tensión puede provocar que la anisotropía magnética cambie de dirección.

En la segunda parte de la tesis nos centraremos en las propiedades ópticas de los semiconductores. En concreto, nos centraremos en el cálculo de las energías de enlace de los excitones, utilizando la teoría del funcional de la densidad dependiente del tiempo (Time-Dependent Density Functional Theory, TDDFT, en inglés). El objetivo de esta investigación ha sido el desarrollo de un código propio que calcula estas energías y que se ha desarrollado a lo largo de toda la tesis. Los resultados que presentamos se pueden encontrar en la referencia [3].

- En el capítulo 6, se introduce el concepto de excitón y las implicaciones de estos en las propiedades ópticas de los semiconductores. También presentamos el estado actual del cálculo de energías excitónicas utilizando métodos *ab inito*.

- En el capítulo 7, revisamos los métodos númericos que se emplean en el cálculo de las energías de ligadura de los excitones en sólidos extensos. En primer lugar, presentaremos la teoría de la densidad del funcional dependiente del tiempo. Mencionamos los teoremas fundamentales y nos centramos en el formalismo de la respuesta lineal (Linear-Response TDDFT), en el que se realizan la mayoría de los cálculos excitónicos. En este formalismo presentamos el kernel de correlación e intercambio (f_{xc}) y las ecuaciones de Dyson y Casida que se utilizan para calcular los espectros ópticos de absorción y las energías de ligadura de los excitones, respectivamente. Por último, también presentaremos el formalismo híbrido que se está utilizando últimamente para el cálculo de energías de excitación más allá de la TDDFT y que combina la ecuación de Casida con la ecuación Bethe-Salpeter (BSE)

de la teoría de perturbación de los muchos cuerpos.

- En el capítulo 8, presentamos nuestros resultados referentes al cálculo de las energías de ligadura de los excitones []. Dividimos nuestro análisis en dos partes. Por una parte, estudiamos las energías de ligadura dentro del formalismo TDDFT, empleando el kernel Long-Range Corrected (LRC) que incluye la interacción Coulombiana de largo alcance. En este formalismo, encontramos que para aplicar el truco del conmutador que se emplea para el cálculo de los términos singulares de la ecuación de Casida, es necesario incluir un término de corrección addicional C_{cv} que aparece al tratar con sólidos infinitos. Calculamos la magnitud de este término para diferentes semiconductores, y descubrimos que a menudo es varios órdenes de magnitud mayor que el própio término singular, dejando claro la necesidad de incluir éste termino para describir los excitones correctamente. Por otra parte, también calculamos las energías de ligadura en el formalismo híbrido. Utilizando un nuevo kernel, que está basado en truncar el kernel Screened Exact Exchange (SXX) en la supercelda Wigner-Seitz del cristal, obtenemos dichas energías para diversos materiales semiconductores y aislantes. El kernel SXX incluye una parte de la energía de intercambio exacta, pero apantallada por la función dieléctrica del compuesto. Comparamos nuestros resultados teóricos con los que hay disponibles en la bibliografía, y analizamos la tendencia de las energías obtenidas respecto a los parametros de convergencia. A pesar de que las energías que se obtienen son mejores que las del formalismo TDDFT, descubrimos una preocupante dependencia de los resultados con respecto al muestreo de la zona de Brillouin. Todo esto dificulta obtener energías de ligadura bien convergidas, limitando las capacidades predictivas del modelo, y apunta a la necesidad de desarrollar kernels más avanzados que describan la interacción electron-hueco en el excitón de una forma más completa.

Part I

Magnetic properties of layered oxides

CHAPTER 1

INTRODUCTION

Magnetism is a property of materials long known to mankind. From the use of magnetic compasses for navigation to the data storage devices and medical imaging of today, the study of magnetism has been present in the progress of mankind. The first references to magnetism date back to ancient Greece, where the attraction effect of magnetite (Fe_3O_4) on iron was already observed and studied. However, it was not until the 19th century that the relationship between magnetism and electricity was made: the experiments of Ørsted, Ampère, Gauss and Faraday established the link between magnetism and electricity, which was later synthesized in Maxwell's equations. In this framework, the magnetic and electric fields could be described, but the origin of magnetism in materials was still unknown. In the 20th century, with the advent of Quantum Mechanics, the structure of atoms was better understood, which lead to de discovery of the spin, and revolutionized the knowledge about magnetic materials. In the Stern-Gerlach experiment in 1922, it was observed that a neutral beam of Ag atoms in an inhomogeneous magnetic field split into two [4]. This finding was the first experimental evidence of the existence of an intrinsic and quantized angular momentum of atoms[1]. By the end of 1924, while studying the anomalous Zeeman effect and ferromagnetism, Pauli proposed that it was necessary to consider an additional quantum number to describe the electronic structure and spectral lines of certain elements [5]. Uhlenbeck and Goudsmit suggested the physical interpretation of this quantum number as the angular moment of a particle spinning around itself[2] [6]. In 1925, Pauli formulated

[1] In the case of silver atoms, it was also found that this angular momentum had to be non-integer, since if the momentum had the minimum integer value of 1, the beam would split into three, as would correspond to atoms with L_z=1,0,-1.

[2] Even if this can work as an intuitive way to visualize the spin, in reality, spin is a quantum property with no analogous classical counterpart. We consider electrons to be point-like particles that are not spinning.

his famous Pauli exclusion principle [5], which states that two electrons cannot be in the same quantum state; that is, they cannot have the same quantum numbers. For two electrons in the same orbital (with the same n, l and m_l numbers), their m_s number must be different, and therefore their spin projections must be opposite (+1/2 and -1/2). All of this lead to the concept of electron spin, as an intrinsic angular momentum of the electron associated with the quantum number m_s. The mathematical description of the spin was established with the relativistic wave equation Dirac derived in 1928, which naturally included the spin [7]. Analogously to the orbital momentum $\mathbf{L}$, the spin can be associated with a vector $\mathbf{S}$ which is described by the Pauli matrices. Therefore, the magnetic moment of an electron has two contributions: one arising from its orbital angular momentum (μ_L), similar to a charged particle that is rotating, and the other due to its spin (μ_S).

In atoms, the total magnetic moment is a consequence of the unpaired electron spins yielding a non-zero net magnetic moment. As a consequence, isolated atoms with unpaired electrons show some kind of magnetism. However, in bulk materials composed of single elements, we find magnetism in few of them, mostly containing transition metal or rare-earth atoms [8, 9]. This happens because in a bulk material the electrons from different atoms can interact with each other, and this interaction can lead to a delocalized behavior, thus weakening the local magnetic moment of the different atoms. On top of that, the thermal disorder can also disrupt the alignment of the spins, which decreases the magnetism of the material. How is it possible to have magnetism in bulk materials then? The answer lies in the magnetic exchange interaction ($J\ \mathbf{S}_1 \cdot \mathbf{S}_2$), which is a consequence of the Pauli exclusion principle and Coulomb interaction, and energetically favors the alignment of the different spins. If the exchange coupling is large enough, it can overcome the thermal disorder, and the material will present magnetism. Magnetic materials can show different spin alignments: ferromagnetic (spins parallel) [10], antiferromagnetic (spins antiparallel) [11], ferrimagnetic (spins antiparallel, but the total magnetization is not cancelled) or more complex structures involving non-collinearity and spin-spirals [12]. Both for ferromagnetic and antiferromagnetic compounds, there is a critical temperature that marks the ending of the magnetic ordering and the beginning of paramagnetism. This order parameter is the Curie (Néel) temperature of the ferromagnetic (antiferromagnetic) materials. Above these temperatures, the long-range magnetic order is broken, and all the localized moments point in random directions, resulting in a total magnetic moment of zero[3]. Apart from the magnetic exchange, the magnetocrystalline anisotropy energy (MAE), originating from the spin-orbit coupling, couples the spin magnetic moment to a certain crystallographic direction, making the magnetic properties of the system more resistant to an external field.

A good theoretical description of the magnetic exchange is crucial for

[3] Even above this temperature, the magnetic atoms of the compound can present a well-defined local magnetic moment. The long-range, macroscopic magnetism is what is lost above the critical temperature.

understanding the behavior of magnetic materials and for predicting and designing new compounds with desired properties. In this thesis, we chose Density Functional Theory [13, 14] as our framework to study the magnetism of transition metal oxides; such as ilmenites and ilmenenes. DFT is a method that has revolutionized the field of solid-state physics by providing numerical approaches that yield accurate results at a moderate computational cost. DFT lightens the burden of solving the many-body Schrödinger equation by solving an auxilary system of non-interacting electrons that has the same ground state density (and energy) as the real system. In its spin-polarized form, DFT allows us to compute the total energy of different magnetic configurations of the material under analysis. These energies can then be used to compute the exchange coupling constants between the spin orderings, and determine the magnetic ground state of the system [15]. If the spin-orbit coupling is included, the magnetocrystalline anisotropy energy of the material can also be obtained using DFT, by comparing the total energy of configurations with the magnetization oriented in different crystalline directions. Therefore, DFT is a powerful tool that can provide a wide amount of information of the magnetic properties of systems, at a computationally moderate cost. Nevertheless, albeit being a formally exact theory, the precision of DFT is limited by the way in which the exchange and correlation are approximated when performing calculations. For example, in materials with a strong electron correlation, such as in magnetic compounds containing $3d$ transition metals, DFT often fails to even give a good qualitative description of the system, i.e. predicting a metallic character instead of insulating [16–18]. There are several methods to improve the description of the electronic exchange and correlation in DFT. In this thesis, we focus on the DFT+U method [19], which includes a Hubbard-like correction term that acts in the localized electrons of the material; correcting the electron delocalization and giving a better description of the magnetic compounds of our interest.

In this block of the thesis, our goal is the study of the magnetic properties of layered oxide semiconductors. We focus our analysis in two parts: (i) the study of the magnetism of the bulk oxide $CoTiO_3$ ilmenite, and (ii) the characterization of two-dimensional $TMTiO_3$ ilmenenes, where TM are $3d$ transition metals (TM=V, Cr, Mn, Fe, Co, Ni, Cu, Zn). Due to the effort required to synthesize these materials experimentally, the theoretical study of such materials is essential to find ideal candidates that exhibit the desired properties. For both cases, we systematically analyze the different magnetic configurations of each compound using Density Functional Theory in the DFT+U framework, and study the exchange coupling and the magnetic anisotropy. The aim of this work is to establish a solid theoretical basis for future and more advanced calculations on these compounds.

On the one hand, bulk ilmenite cobalt titanate $CoTiO_3$ is a layered oxide that has attracted a lot of interest lately, because of the presence of intriguing solid-state phenomena in this material, such as ferroelectricity, piezoelectricity or the magnetodielectric effect [20–23]. In particular, it is the applications of cobalt titanate in the field of spintronics what has attracted attention to this material.

Inelastic neutron scattering (INS) experiments confirm the presence of Dirac Magnons [24, 25] in cobalt titanate (see Fig. (1.1)). Magnons are quasiparticles that describe the collective excitation of the spin structure of a compound, and can be seen as a quantized spin-wave. Magnons are of great interest in spintronics, because they could be used to transport information in such devices, potentially leading to faster and more efficient computing. Even though there is considerable experimental work on ilmenite cobalt titanate, to the best of our knowledge, there is no theoretical study on the magnetism of this compound. We study the fundamental magnetic properties of cobalt titanate, aiming to set a solid theoretical basis for future calculations, such as spin-spiral and magnon dispersions.

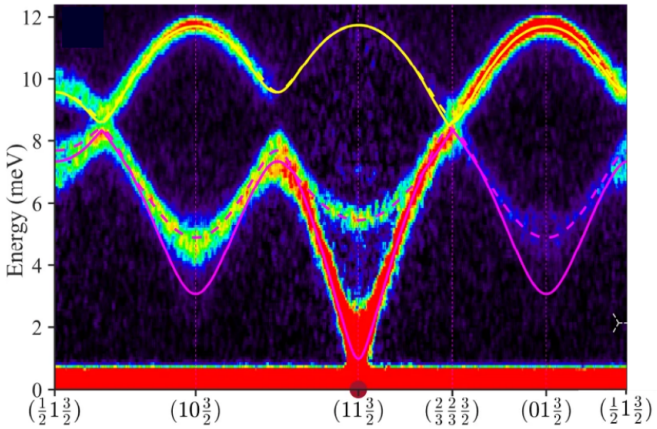

Figure 1.1: INS data at 8K observing the magnon dispersions along high-symmetry directions in the hexagonal plane. Lines are the dispersions $\tilde{\omega}(\mathrm{k})$ of the XXZΔ model, the brown dot on the elastic line indicates the location of the magnetic Bragg peak. The incident neutron energy was E_i=18meV. The color bars indicate scattering intensity in arbitrary units on a linear scale. Figure adapted with permission from reference [24].

On the other hand, ilmenene is a promising new two-dimensional non-van de Waals magnetic material that has been exfoliated from bulk ilmenite [26](see Fig. (1.2)). In conjunction with titania nanotube arrays, it has been observed that ilmenene is a promising candidate to be used in photoelectrochemical water splitting. Based on the similar structure of iron ilmenite and other transition metal compounds (such as cobalt titanate), it is not difficult to think that new two-dimensional magnetic ilmenene-like compounds could also be synthesized in the near future. We expand the analysis to most of the ilmenene–like $3d$ transition metal titanates, and describe the structural, electronic and magnetic properties of these compounds, providing a general background for future experimental and theoretical work involving these materials.

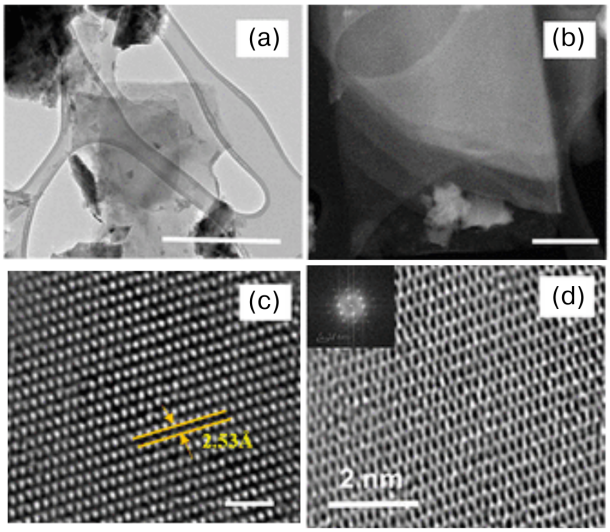

Figure 1.2: Experimental images of iron ilmenene. (a) Bright-field tunneling electron microscope (TEM) images of monolayer and bilayer ilmenene sheets (scale bar of 0.5 μm). (b) Dark-field TEM images of a multilayer stack of ilmenene sheets (scale bar of 0.2 μm). (c) HRTEM image showcasing the interplanar spacing of 2.53 Å (scale bar of 1 nm). This distance corresponds to the $(11\bar{2}0)$ and $(2\bar{1}10)$ lattice spacing of the ilmenite structure signifying the (001) plane. (d) HRTEM image of the (001) ilmenene plane (scale bar of 2 nm). The hexagonal lattice of ilmenene is clearly observed in this figure.
Figure adapted with permission from reference [26]. Copyright 2018 American Chemical Society.

CHAPTER 2

NUMERICAL METHODS

Ferromagnetism has its origin in the exchange interaction between the spin momentum of electrons in materials. Therefore, because we are interested in a quantum effect that happens on the atomic scale, quantum mechanics will be our working framework.

2.1 The Quantum Many-Body Problem

In general, if we want to study a quantum system with N_e electrons and N_I nuclei, this implies solving the following time-dependent Schrödinger equation

$$\hat{H}\Phi(\mathbf{r}_e, \mathbf{R}_I, t) = i\frac{\partial\Phi(\mathbf{r}_e, \mathbf{R}_I, t)}{\partial t}, \tag{2.1}$$

where t is time, $\Phi(\mathbf{r}_e, \mathbf{R}_I, t)$ is the many-body wavefunction that describes the system, being $\mathbf{r}_e = (\mathbf{r}_1, ..., \mathbf{r}_{N_e})$ and $\mathbf{R}_I = (\mathbf{R}_1, ..., \mathbf{R}_{N_I})$ the electronic and ionic spatial coordinates, respectively. In many cases, solving the time-independent stationary problem is all we need to do. Then, the spatial coordinates and time can be separated, and the stationary Schrödinger equation is obtained:

$$(T_e + T_I + V_{ee} + V_{Ie} + V_{II})\Psi(\mathbf{r}_e, \mathbf{R}_I) = E\Psi(\mathbf{r}_e, \mathbf{R}_I). \tag{2.2}$$

Here, $\Psi(\mathbf{r}_e, \mathbf{R}_I)$ is the time-independent wavefunction, and E is the total energy of the system. T_e and T_I are the electronic and ionic kinetic energy operators, and V_{ee}, V_{II} and V_{Ie} are the electron-electron, ion-ion and ion-electron Coulomb

interactions, which are mathematically described as[1][2]

$$\hat{H} = \sum_{i}^{N_e} -\frac{1}{2}\nabla_i^2 + \sum_{j}^{N_I} -\frac{1}{2\tilde{M}_I}\nabla_j^2 + \frac{1}{2}\sum_{i\neq i'}^{N_e}\frac{1}{|\mathbf{r}_i - \mathbf{r}_{i'}|} \tag{2.3}$$

$$-\sum_{i}^{N_e}\sum_{j}^{N_I}\frac{Z_j}{|\mathbf{R}_j - \mathbf{r}_i|} + \frac{1}{2}\sum_{j\neq j'}\frac{Z_j Z_{j'}}{|\mathbf{R}_j - \mathbf{R}_{j'}|}. \tag{2.4}$$

Even though all the information about the system is encoded in the wavefunction Ψ, and solving the many-body Schrödinger equation (2.2) is all we have to do; in practice, getting an exact solution is unfeasible. The large size of the system, which has $3(N_e + N_I)$ variables, in conjunction with the computational cost of calculating the Coulomb interaction terms, requires approximations.

2.1.1 The Born-Oppenheimer Approximation

The Born-Oppenheimer approximation [27] consists mainly in decoupling the electronic and ionic parts of Eq. (2.2), by assuming that the wave function of the system can be written in the following manner:

$$\Psi(\mathbf{r}_e, \mathbf{R}_I) = \sum_n \psi_n(\mathbf{R}_I)\phi_n(\mathbf{r}_e, \mathbf{R}_I). \tag{2.5}$$

Here, $\psi_n(\mathbf{R}_I)$ and $\phi_n(\mathbf{r}_e, \mathbf{R}_I)$ are the ionic and electronic wave functions, and n runs over all ions. The large difference between nuclear and electron masses [3], allows us to neglect the kinetic energy of the ions, i.e. $T_I = 0$, therefore treating the system as an electronic problem on top of a frozen ion configuration.

Plugging the wavefunction in Eq. (2.5) into Eq. (2.2) yields the following equation for the electronic degrees of freedom:

$$(T_e + V_{ee} + V_{Ie} + V_{II})\phi_{\mathbf{R}_I}(\mathbf{r}_e, \mathbf{R}_I) = E_{\mathbf{R}_I}\phi_{\mathbf{R}_I}(\mathbf{r}_e, \mathbf{R}_I). \tag{2.6}$$

Note that in the ionic degrees of freedom enter as parameters in the previous equation, and that the potential energy term V_{II} is a constant for a given ionic configuration. The Born-Oppenheimer approximation reduces the size of the system from $3(N_I + N_e)$ degrees of freedom to $3N_e$ variables.

[1] Throughout all this thesis, and unless stated otherwise, atomic units will be used, so $m_e = e = \hbar = 1$

[2] $\tilde{M}_I$ is the nuclear mass of ion I.

[3] Even in the lightest case, the hydrogen atom, the ratio between proton and electron masses is of the order of $M_p/m_e \simeq 1836$, which makes the kinetic energy of the nuclei negligible with respect to the kinetic energy of the electrons.

2.1.2 Hartree-Fock method

Even if the Born-Oppenheimer approximation is adopted, the many-body character of the wavefunction and the electron-electron interaction needs to be addressed to perform calculations efficiently. The Hartree-Fock method [28] approximates the total wavefunction of the system using a Slater determinant [29] of the single-particle electron wavefunctions:

$$\psi(\mathbf{r}_1, \mathbf{r}_2, ..., \mathbf{r}_{N_e}) = \frac{1}{\sqrt{N_e!}} \begin{vmatrix} \phi_1(\mathbf{r}_1) & \phi_2(\mathbf{r}_1) & ... & \phi_{N_e}(\mathbf{r}_1) \\ \phi_1(\mathbf{r}_2) & \phi_2(\mathbf{r}_2) & ... & \phi_{N_e}(\mathbf{r}_2) \\ \vdots & \vdots & \ddots & \vdots \\ \phi_1(\mathbf{r}_{N_e}) & \phi_2(\mathbf{r}_{N_e}) & ... & \phi_{N_e}(\mathbf{r}_{N_e}) \end{vmatrix}, \tag{2.7}$$

where $\mathbf{r}_i$ are the spatial and spin coordinates of each electron. One of the main features of this approximate wavefunction is that it satisfies the Pauli exclusion principle, i.e. it is antisymmetric with respect to particle interchange.

Using the wavefunction in Eq. (2.7), the expectation value of the many-body Hamiltonian of Eq. (2.2) is

$$\begin{aligned} \langle \hat{H} \rangle = & \sum_{i}^{N_e} \int d\mathbf{r} \phi_i^*(\mathbf{r}) \left[-\frac{1}{2}\nabla^2 + V_{ext} \right] \phi_i(\mathbf{r}) \\ & + \frac{1}{2} \sum_{ij}^{N_e} \int d\mathbf{r} d\mathbf{r}' \frac{|\phi_i(\mathbf{r})|^2 |\phi_j(\mathbf{r})|^2}{|\mathbf{r} - \mathbf{r}'|} \\ & - \frac{1}{2} \sum_{ij}^{N_e} \int d\mathbf{r} d\mathbf{r}' \phi_i^*(\mathbf{r}) \phi_j^*(\mathbf{r}') \frac{1}{|\mathbf{r} - \mathbf{r}'|} \phi_j(\mathbf{r}) \phi_i(\mathbf{r}'). \end{aligned} \tag{2.8}$$

The first row in Eq. (2.8) contains the kinetic energy of each electron and the external potential acting on the them. The terms in the second and third rows are the so-called Hartree and exchange terms, respectively. The Hartree term represents the Coulombic repulsion energy of two charge densities $|\phi_i|^2$ and $|\phi_j|^2$ integrated over the locations of the two electrons i and j. The exchange term arises from the Pauli exclusion principle. Note that for $i = j$ the Hartree term includes an unphysical self-interaction of the electrons, which is exactly canceled by the exchange term.

To get the ground state energy, the variational principle is used in the Hartree-Fock method. The energy of the system is minimized using the Lagrange multipliers ϵ_i, while imposing that the one-electron wavefunctions are orthogonal:

$$\frac{\partial}{\partial \phi} \left[\langle \hat{H} \rangle - \sum_i \epsilon_i \int d\mathbf{r} |\phi_i(\mathbf{r})|^2 \right] = 0. \tag{2.9}$$

The HF approach is a practical scheme to solve the many-body electron problem starting from one-electron wavefunctions. However, the HF method neglects the correlation between electrons (by assuming a single determinant form of the wavefunction), which can lead to the incorrect description of the systems under analysis, often overestimating HOMO-LUMO band gaps in insulators [30].

2.2 Density Functional Theory

Density Functional Theory (DFT) is a numerical method that replaces the many-body wavefunction $\Psi(\mathbf{r}, \mathbf{r}_2, ..., \mathbf{r}_{N_e})$ with the electron density $n(\mathbf{r})$ as its main variable. The electron density is obtained by integrating the wavefunction over all but one spatial variable

$$n(\mathbf{r}) = N \int d\mathbf{r}_2 ... \int d\mathbf{r}_{N_e} \Psi^*(\mathbf{r}, \mathbf{r}_2, ..., \mathbf{r}_{N_e}) \Psi(\mathbf{r}, \mathbf{r}_2, ..., \mathbf{r}_{N_e}), \tag{2.10}$$

and has the advantage of only depending on 3 spatial coordinates, compared to the $3N_e$ variables of the wavefunction.

2.2.1 Hohenberg-Kohn Theorems

The basis of DFT were established by Hohenberg and Kohn [13], which demonstrated that:

1) For an electronic system in an external potential $v_{ext}(\mathbf{r})$, there is a one to one correspondence between the potential and the ground state density $n_0(\mathbf{r})$, except for a constant.

2) For any external potential $v_{ext}(\mathbf{r})$, a universal functional of the total energy $E[n]$ exists, and the exact ground state of the system is determined by the global mininum of this functional:

$$E_0[n] = \min_{\phi \in \Psi} \langle \phi | H | \phi \rangle = \min_{n \in N} E_{v_{ext}}[n], \tag{2.11}$$

where Ψ and N represent the ensemble of ground state wave functions and electron densities, respectively. The energy functional $E[n]$ can be written as

$$E[n(\mathbf{r})] = F[n(\mathbf{r})] + \int v_{ext}(\mathbf{r}) n(\mathbf{r}) d\mathbf{r}, \tag{2.12}$$

where $F[n] = T[n] + V_{ee}[n]$ is the universal functional that accounts for the kinetic

energy of the electrons and their interaction, and the right term describes the interaction of the density with the external potential.

The Hohenberg-Kohn theorems establish a theoretical framework to calculate the ground state energy of the system using the density $n(\mathbf{r})$ as the main variable, but without knowing the expression for the functional $F[n]$, its practical application is not straightforward.

2.2.2 Kohn-Sham ansatz

Kohn and Sham developed a practical application of the HK theorem by studying one of the simplest systems: the problem of N non-interacting electrons under an external potential [14]. The energy functional of that system is

$$E_s[n] = T_s[n] + \int v_s(\mathbf{r}) n(\mathbf{r}) d\mathbf{r}, \tag{2.13}$$

where $T_s = \sum_i^{N_e} \left\langle \phi_i^{KS} \right| -\frac{1}{2}\nabla_i^2 \left| \phi_i^{KS} \right\rangle$ is the kinetic energy functional of the non-interacting electrons, and v_s is the external effective potential that acts on the particles. In the non-interacting system, the ground state wavefunction of the system is the Slater determinant of the single-particle orbitals ϕ^s, which are calculated from the N decoupled Schrödinger equations

$$\left[-\frac{\nabla_i^2}{2} + v_s(\mathbf{r}) \right] \phi_i^s(\mathbf{r}) = \epsilon_i \phi_i^s(\mathbf{r}). \tag{2.14}$$

As long as the effective potential v_s is known, this system can be exactly solved, as the density is computed from the ϕ^s orbitals:

$$n_s(\mathbf{r}) = \sum_i^{N_e} |\phi_i^s(\mathbf{r})|^2. \tag{2.15}$$

The basis of the Kohn-Sham approach is the following: since the energy is a functional of the ground state density, an auxiliary system of non-interacting particles with the same density as the real system ($n_s(\mathbf{r}) = n(\mathbf{r})$) can be used to calculate the energy of the real system.

In the interacting system, the electron-electron interaction can be split into two terms $V_{ee} = E_H + U_{xc}$, where E_H is the energy due to the classical Coulomb interaction between two charge densities (also called the Hartree term), and U_{xc} is a smaller term that accounts for the exchange and correlation effects of the interaction. Similarly, the kinetic energy of the electron can be split as $T = T_s + T_c$, where T_c is the difference between kinetic energy of the interacting and non-interacting electrons. All of this allows us to rewrite the energy functional of the interacting

system as follows

$$E[n] = T_s[n] + E_H[n] + E_{xc}[n] + \int v_{ext}(\mathbf{r})n(\mathbf{r})d\mathbf{r}, \tag{2.16}$$

where all the terms are known, except for the exchange-correlation energy $E_{xc} = (V_{ee} - E_H) + T_c$. One of the keys of the Kohn-Sham approach is that this term is indeed much smaller than the rest of the known contributions, meaning that a big fraction of the total energy can be calculated exactly.

By minimizing equations (2.13) and (2.16) with respect to the density, the effective potential acting on the non-interacting electrons is

$$v_s = v_{KS} = v_{ext} + \int d\mathbf{r}' \frac{n(\mathbf{r}')}{|\mathbf{r} - \mathbf{r}'|} + v_{xc}(\mathbf{r}). \tag{2.17}$$

Here, $v_{xc} = \frac{\delta E_{xc}}{\delta n(\mathbf{r})}$ is the exchange-correlation potential, which is the unknown term. In practice, there is no analytical expression for this magnitude, and it has to be numerically approximated (as we will discuss in section 1.3).

Using all of the above, Kohn and Sham established a **self-consistent method** to perform calculations in the framework of the Density Functional Theory, which we graphically depict in Fig. 2.1: for an initial guess density $n(\mathbf{r})$, the v_{KS} potential is calculated from Eq. (2.17), which yields a set of single particle wavefunctions by solving Eq. (2.14). These wavefunctions are used to calculate a new density $n'(\mathbf{r})$ from Eq. (2.15), which is compared to the initial density. The previous procedure is repeated until the calculated density is within a certain convergence threshold. The converged density can then be used to compute the ground-state magnitudes of interest of which we know the functional, such as the total energy of the system from Eq.(2.16).

2.2.3 Exchange and correlation functionals: LDA and GGA

Density Functional Theory is formally an exact theory, which would yield the exact ground state properties of the system, once it is provided that the exchange-correlation energy functional E_{xc} is known. However, in practice, there is no known analytic expression for this term, and approximations are needed in order to perform DFT calculations. The Local Density Approximation (LDA) and the Generalized Gradient Approximation (GGA) are two of the most used.

In the **Local Density Approximation** [14], the exchange-correlation functional E_{xc} is approximated by a local functional of the density in the limit of the homogeneus electron gas (HEG)

$$E_{xc}^{LDA}[n] = \int n(\mathbf{r})\epsilon_{xc}^{HEG}(n(\mathbf{r}))d\mathbf{r}, \tag{2.18}$$

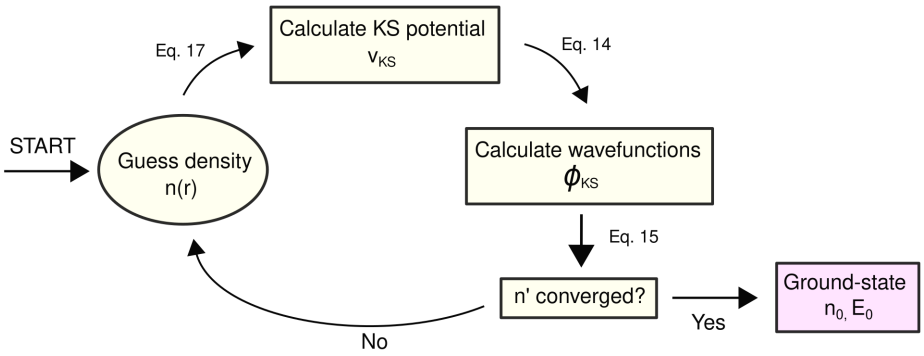

Figure 2.1: Schematic representation of the Kohn-Sham self-consistent procedure.

where $\epsilon_{xc}^{HEG}(n(\mathbf{r}))$ is the exchange-correlation energy per electron in a homogeneous electron gas. For a homogeneus electron gas, the exchange part of this term is known, while the correlation energy needs to be approximated with numerical methods, such as Monte Carlo methods. The applicability of LDA goes beyond the homogeneous electron gas, and is currently used in a wide array of materials. One of the main shortcomings of LDA is the overbinding of the electrons, which often leads to an underestimation of bond lengths [31] and band gaps [32].

The **Generalized Gradient Approximation** is a generalization of the LDA that includes a gradient of the density to take the spatial variations of the density into account:

$$E_{xc}^{GGA}[n] = \int n(\mathbf{r})\epsilon_{xc}^{HEG}(n(\mathbf{r}))F_{xc}(n(\mathbf{r}), |\nabla n(\mathbf{r})|)d\mathbf{r}. \tag{2.19}$$

Here, ϵ_{xc}^{HEG} is the exchange correlation energy functional of the homogeneous electron gas, and F_{xc} is the enhancement function that includes the non-locality of the density through its gradients. GGA functionals improve the description of the exchange and correlation, and can yield chemically accurate bond lengths[4]. Unless stated otherwise, all the GGA calculations in this thesis were performed in the parametrization of F_{xc} given by Perdew, Burke and Ernzerhof (PBE) [33].

[4] Band gaps are still underestimated within the GGA.

2.2.4 Spin in DFT

The generalization of DFT to include spin was done by Barth and Hedin [34]. Using spinor wavefunctions $\phi(\mathbf{r}) = \begin{pmatrix} \phi^{\uparrow} \\ \phi_{\downarrow} \end{pmatrix}$, the density matrix $\hat{n}(\mathbf{r})$ can be defined as

$$\hat{n}(\mathbf{r}) = \frac{1}{2}(n(\mathbf{r})\mathbf{I} + \boldsymbol{\sigma} \cdot \mathbf{s}(\mathbf{r})) = \frac{1}{2}\begin{pmatrix} n(\mathbf{r}) + s_z(\mathbf{r}) & s_x(\mathbf{r}) - is_y(\mathbf{r}) \\ s_x(\mathbf{r}) + is_y(\mathbf{r}) & n(\mathbf{r}) - s_z(\mathbf{r}) \end{pmatrix}, \tag{2.20}$$

where $n(\mathbf{r})$ is the scalar electron density, $\mathbf{s}(\mathbf{r})$ is the vectorial spin-density, $\mathbf{I}$ is the 2x2 identity matrix, and $\boldsymbol{\sigma} = (\sigma_x, \sigma_y, \sigma_z)$ are the Pauli matrices.

In this framework, the Kohn-Sham equations are the following:

$$\left[\left(-\frac{1}{2}\nabla^2 + \int \frac{\hat{n}(\mathbf{r}')}{|\mathbf{r} - \mathbf{r}'|}d\mathbf{r}'\right)\mathbf{I} + \hat{v}_{ext}(\mathbf{r}) + \hat{v}_{xc}(\mathbf{r})\right]\begin{pmatrix} \phi_i^{\uparrow} \\ \phi_i^{\downarrow} \end{pmatrix} = \epsilon_i \begin{pmatrix} \phi_i^{\uparrow} \\ \phi_i^{\downarrow} \end{pmatrix} \tag{2.21}$$

where $\hat{v}_{ext}$ and $\hat{v}_{xc}$ are now functionals of the density matrix. In the special case with no external magnetic field and with spins aligned in the z-axis [15], which describes all the collinear magnetic configurations, Eq. (2.21) splits in two decoupled equations for the spin-up ($\phi\uparrow$) and spin-down ($\phi\downarrow$) channels:

$$\left[-\frac{1}{2}\nabla^2 + \int \frac{n(\mathbf{r}') + s_z(\mathbf{r}')}{|\mathbf{r} - \mathbf{r}'|}d\mathbf{r}' + v_{ext}(\mathbf{r}) + v_{xc}^{\uparrow\uparrow}(\mathbf{r})\right]\phi_i^{\uparrow} = \epsilon_i \phi_i^{\uparrow} \tag{2.22}$$

$$\left[-\frac{1}{2}\nabla^2 + \int \frac{n(\mathbf{r}') - s_z(\mathbf{r}')}{|\mathbf{r} - \mathbf{r}'|}d\mathbf{r}' + v_{ext}(\mathbf{r}) + v_{xc}^{\downarrow\downarrow}(\mathbf{r})\right]\phi_i^{\downarrow} = \epsilon_i \phi_i^{\downarrow} \tag{2.23}$$

where $v_{xc}^{\uparrow\uparrow,\downarrow\downarrow} = \frac{\delta E_{xc}[n^{\uparrow\uparrow,\downarrow\downarrow}]}{\delta n^{\uparrow\uparrow,\downarrow\downarrow}}$. In the case where the charge density is not spin-polarized, i.e. $n\uparrow\uparrow = n\downarrow\downarrow$, both equations are identical.

2.2.5 Strongly correlated systems: DFT+U method

While DFT is a successful method for calculating a wide variety of physical phenomena, it still presents shortcomings when studying highly correlated systems [19, 35]. In compounds that contain rare-earth or transition metals, the energy gap involves bands of the orbitals with d and f character [36]. LDA and GGA exchange-correlation functionals tend to over-delocalize these electrons, and this often results in an itinerant electron behavior, which can lead to an incorrect description of physical properties such as the total energy, local magnetic moments and magnetic exchange couplings [17, 18]. This behavior is especially notable in the so-called Mott insulators, where DFT often predicts these insulating materials to have a metallic character [16].

This delocalization is linked to the inability of the approximated exchange-correlation functionals to fully cancel out the self-interaction in the Hartree term [19]. This residual part of the self-interaction can induce a delocalization of the

otherwise localized electrons. In order to correctly describe the electronic structure of systems with localized electrons, the Coulomb interaction between localized states has to be properly corrected. The DFT+U approach adds the Coulomb U parameter of the Hubbard Hamiltonian to the DFT framework [19].

In DFT+U, the total energy functional of the system is separated in two parts: a ground state DFT total energy term, and an orbital-dependent Hubbard-like term, which describes the Coulomb interaction between the electrons in the localized orbitals. The DFT+U functional [37] is given by

$$E^{DFT+U}[\rho^\sigma, n_l^\sigma] = E^{DFT}[\rho^\sigma] + E^{ee}[n_{mm'}^{I\sigma}] - E^{DC}[n^{I\sigma}], \tag{2.24}$$

where E^{DFT} is the DFT total energy functional, obtained within the LDA or GGA, E^{ee} is the Hubbard-like electron-electron interaction energy responsible of correcting the electron delocalization, and E^{DC} is the double counting term that subtracts the electron-electron interaction of localized states that is already included in E^{DFT}. Here, $\rho^\sigma(\mathbf{r})$ is the spin-dependent electron density (with $\sigma = \uparrow, \downarrow$) on which the DFT energy depends. The Hubbard and double counting terms have an explicit orbital dependence, which is included with the orbital occupation numbers $n_m^{I\sigma}$, where I is the atomic site index, and m are the orbitals of the shell l ($m = -l, ..., l$).

The occupation matrix $n_{mm'}^{I\sigma}$ is given by a projection of the Ψ_{kv}^σ Kohn-Sham orbitals onto a localized basis set:

$$n_{m,m'}^{I\sigma} = \sum_{k,v} f_{kv}^\sigma \left\langle \Psi_{kv}^\sigma \middle| \phi_{m'}^I \right\rangle \left\langle \phi_m^I \middle| \Psi_{kv}^\sigma \right\rangle . \tag{2.25}$$

In Eq. (2.25), f_{kv}^σ are the occupations of the KS states, where the indices k and v represent the k-point and band, respectively. Using the definitions $n_m^{I\sigma} = n_{mm}^{I\sigma}$ and $n^I = \sum_{m,\sigma} n_m^{I\sigma}$, the DFT+U energy functional can be rewritten as

$$\begin{aligned} E^{DFT+U}[\rho(\mathbf{r})] &= E^{DFT}[\rho(\mathbf{r})] \\ &+ \sum_I \left[\frac{U^I}{2} \sum_{m,\sigma \neq m',\sigma'} n_m^{I\sigma} n_{m'}^{I\sigma'} - \frac{U^I}{2} n^I (n^I - 1) \right] . \end{aligned} \tag{2.26}$$

To get a qualitative view of the physical effect of the added terms, the Hubbard contribution to the DFT+U potential can be derived from Eq. (2.26) using the atomic orbital occupations given in Eq. (2.25):

$$V_{DFT+U} = V_{DFT}^\sigma + \sum_{I,m} U^I \left(\frac{1}{2} - n_m^{I\sigma} \right) \left| \phi_m^I \right\rangle \left\langle \phi_m^I \right| . \tag{2.27}$$

The Hubbard potential in Eq. (2.27) is repulsive when the orbitals are less than

half-filled ($n_m^{I\sigma} < 1/2$), and attractive otherwise. Therefore, it can be seen that the DFT+U approach adds an energy penalty to the fractional occupation of the localized atomic orbitals (which is often a sign of hybridization with neighboring atoms), and favors the localization of electrons in particular atomic states when $n_m^{I\sigma} \to 1$. The difference between the Hubbard potential acting on occupied and unoccupied orbitals is in the order of the chosen U parameter, which creates an energy gap in the Kohn-Sham band spectrum.

It should be noted that the quantity in Eq. (2.25) is not invariant under the rotation of the basis set of atomic orbitals employed, which makes the calculations depend on the chosen localized basis. Nevertheless, in practice, rotationally invariant formulations of DFT+U are used, the most widely adopted of which are the ones by Liechtenstein et al. [37] and the simplified approach by Dudarev et al. [38]. In this thesis, we will focus on the Dudarev approach, where the DFT+U energy functional is given by

$$E^{DFT+U}[\rho(\mathbf{r})] = E^{DFT}[\rho(\mathbf{r})] + \frac{\tilde{U}}{2} \sum_{\sigma} \left(\sum_{m} n_{mm}^{\sigma} - \sum_{mm'} n_{mm'}^{\sigma} n_{m'm}^{\sigma} \right). \quad (2.28)$$

Here, $\tilde{U} = U - J$ is the Hubbard electron interaction term, which includes the Coulomb interaction (U) and exchange terms (J) in an effective way [38]. Even though they can in principle be determined *ab initio*; in practice, the U parameters are often used as a semiempirical or input parameter. It should be noted that in DFT+U calculations the total energy will depend on the used U (and J) parameter, which means that only the total energies of calculations performed with the same Hubbard terms can be compared.

As an example, Figure 2.2 shows the band structure of bulk $CoTiO_3$, calculated using the GGA and GGA+U approaches (with $U_{Ti} = 3.9$ eV and $U_{Co} = 4.5$ eV) [1]. We observe that in the GGA band structure (panel (a)), the band gap of the system is determined by cobalt bands that are around the Fermi energy, with a small hybridization with oxygen and titanium atoms. When the DFT+U approach is used (panel (b)), cobalt orbitals become localized in space, which leads to a splitting of the cobalt bands, considerably increasing the band gap of the system from around 0.2 eV to almost 3.0 eV, and yielding a completely different electronic character. In the GGA+U approach, the valence band consists of hybridized Co-O bands and a conduction band is formed of Co-Ti bands. The electronic bands of the system change considerably from GGA to GGA+U, which goes from being an almost metallic compound to a semiconductor with an interesting layered structure, where electrons localize around the Co-O layers and holes concentrate in the Co-Ti layers.

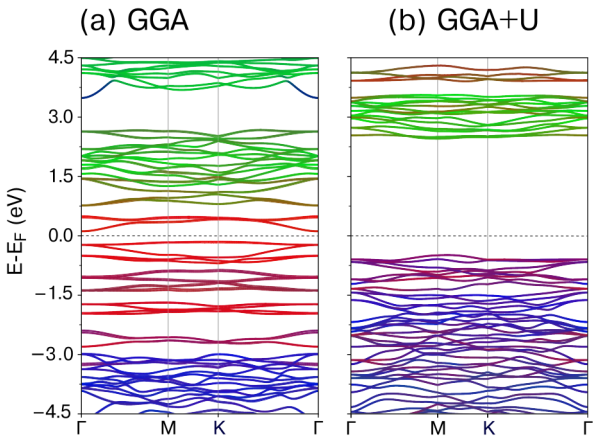

Figure 2.2: Electronic band structure of bulk $CoTiO_3$, computed using (a) GGA and (b) GGA+U DFT calculations. The color scheme represents the projection of the Kohn-Sham orbitals into atomic orbitals of the different elements in the compound. Cobalt is depicted in red, oxygen in blue, and titanium in green.

2.3 Magnetic Properties From First-Principles

2.3.1 Magnetic Ordering and Ground State

An interesting fact about the spin-polarized Kohn-Sham equations (2.22) and (2.23) is that for a given spin density $\mathbf{s}(\mathbf{r})$, they can lead to metastable solutions that are not the magnetic ground state of the system [15]; i.e. for a given initial magnetic state, the system can stay near the input magnetic configuration, even if another lower energy magnetic configuration exists. This makes it difficult to calculate the fundamental state of a particular system using DFT, since the final magnetic configuration is not guaranteed to be the fundamental state of the system. Several magnetic configurations have to be calculated in order to find the ground state.

The magnetic interactions of the system can also be described using a model Hamiltonian. The simplest example is the Heisenberg model

$$H = -\sum_{\langle ij \rangle} J_{ij} \mathbf{S}_i \cdot \mathbf{S}_j, \tag{2.29}$$

where $\mathbf{S}_i$ denotes the spin of the magnetic atom at site i, and J_{ij} is the exchange coupling between the atoms i and j. In this approach, it is assumed that at the positions of the magnetic atoms, the exchange interaction between atoms is large, and that each lattice point can be assigned a well-defined magnetic moment within a sphere centered on the nucleus.

This description of the system allows us to compute the exchange constants of the system by comparing the total energies of different magnetic configurations of the compound (ferromagnetic, antiferromagnetic, ...), since the energy differences between the magnetic states arise due to the exchange interactions described in the model.

2.3.2 Spin-orbit coupling and MAE

We now consider the spin-orbit coupling (SOC) of electrons in solids. The spin-orbit coupling is a relativistic effect that emerges from the interaction between the spin angular momentum $\mathbf{S}$ of an electron and its orbital angular momentum $\mathbf{L}$. In the non-relativistic limit of the Dirac equation, the spin-orbit coupling H_{SOC} is a correction term of the Schrödinger equation with the Hamiltonian

$$H = H_{NR} + H_{SR} + H_{SOC}. \tag{2.30}$$

Here, H_{NR} is the non-relativistic Hamiltonian, and H_{SR} is the scalar-relativistic term including relativistic effects that do not include spin. The spin-orbit coupling term is given by

$$H_{SOC} = \boldsymbol{\sigma} \cdot (-\nabla V(\mathbf{r}) \times \mathbf{p}) = -\frac{1}{r}\frac{dV(r)}{dr}\boldsymbol{\sigma} \cdot (\mathbf{r} \times \mathbf{p}) = \xi(r)\boldsymbol{\sigma} \cdot \mathbf{L}. \tag{2.31}$$

In the previous expression, $\boldsymbol{\sigma}$ are the Pauli matrices, $V(r)$ is the potential, $\mathbf{L}$ is the orbital moment, and $\xi(r) = -\frac{1}{r}\frac{dV(r)}{dr}$ is the variation of the potential around each atomic site. Integrating ξ over radial coordinates, and including the spin $\mathbf{S} = \boldsymbol{\sigma}/2$ in equation 2.31, the spin-orbit coupling is rewritten as

$$H_{SOC} = \lambda \mathbf{S} \cdot \mathbf{L}. \tag{2.32}$$

Here, $\lambda = \langle \xi \rangle / 2$ is the so-called spin-orbit constant [39]. The SOC can induce the splitting of degenerated energy bands in the crystalline field of solids.

The spin-orbit coupling is the origin of an array of effects in magnetic systems, which include the magnetocrystalline anisotropy energy (MAE, from now on), the antisymmetric magnetic exchange (also known as the Dzyaloshinskii–Moriya interaction) [40, 41] and the anomalous Hall effect [42–44]. In this thesis, we will focus on the MAE.

The spin-orbit interaction couples the spin magnetic moment to the symmetry of the crystal, thus resulting in energetically favored directions for the magnetization. The magnetocrystalline anisotropy energy is the energy difference between two magnetic configurations with different magnetization directions. In the DFT framework, the MAE can be computed by subtracting the total energy of two

self-consistent calculations with different spin orientations:

$$\mathrm{MAE} = E_a - E_b. \tag{2.33}$$

In solids, the MAE is usually small (in the order of 10^{-5}-10^{-6} eV/atom)[5], which means that the total energy calculations have to be carefully performed. We are going to compare two large values to get a small energy difference, so the dependence of the calculated results has to be analyzed with respect to the convergence parameters, such as the energy cutoff and the Brillouin Zone sampling.

[5] For cubic systems, this value tends to be in the order of 10^{-6} eV/atom, while for other systems with lower symmetry, the value can increase up to the order of 10^{-5}eV [45].

CHAPTER 3

MAGNETIC PROPERTIES OF BULK ILMENITE $CoTiO_3$

Titanate materials $ATiO_3$ with A being a rare earth or transition metal element have a wide variety of crystal structures, which result in numerous intriguing physical phenomena, such as ferroelectricity, magnetism, multiferroicity and piezoelectricity [20]. In particular, cobalt titanate, $CoTiO_3$, has a broad variety of electronic based industrial applications including catalysis [23], as a high-κ dielectric[1] [22], and as a gas sensor [46]. In addition, $CoTiO_3$ has been recently reported to exhibit Dirac magnons [25] and a magnetodielectric effect [21]. Despite the growing interest in the electronic and magnetic properties of cobalt titanate, to the best of our knowledge, first-principles theoretical studies of its magnetic properties are absent in the literature.

Magnetic properties of $CoTiO_3$ ilmenites are ascribed to cobalt atoms in the form of Co^{2+} ions distributed in layers, structurally in a C_{3v} symmetry given by the neighboring oxygen atoms. Magnetic susceptibility studies indicate that cobalt magnetic moments are antiferromagnetically coupled between layers while they are ferromagnetically coupled within layers [47, 48]. Neutron diffraction experiments assign in-plane magnetic moments to cobalt atoms, a fact that lowers the symmetry around cobalt atoms [25, 47]. However, these studies find that magnetic excitations recover the C_{3v} symmetry around Co^{2+} ions. To reconcile the two pictures, these experimental works have assumed models that include in-plane structural domains given by staggered trigonal distortions and oxygen twin planes. Neutron scattering averages over the domains and allows one to recover the C_{3v} symmetry found in magnetic excitations. Using first-principles calculations, the

[1] κ is the dielectric constant.

phonon vibrational properties were studied to explain Raman observations [21]. Therefore, to complement these lattice dynamics results, and clarify the validity of the assumptions made to explain neutron scattering data, there is a need to study the magnetic properties of $CoTiO_3$ ilmenites in a single perfect crystal in detail.

In this chapter, we perform a theoretical analysis of bulk ilmenite $CoTiO_3$, with the focus on its magnetic properties. In the framework of the Hubbard-corrected GGA (GGA+U) [19], we calculate the lattice parameters and band structure of $CoTiO_3$, and find that the G-type antiferromagnetic structure reported in the experiments [25, 47, 48] is the ground-state of the system. Two critical temperatures are observed, resulting in a temperature region above the Néel temperature where the system would still present ferromagnetism within the individual layers. We also calculate the magnetic anisotropy of the system, which favors out-of-plane magnetization, a finding that seems to be at odds with previous experimental findings. However, we analyze the variation of the magnetocrystalline anisotropy energy (MAE) with respect to the number of electrons in the unit cell, and propose that the experimental in-plane magnetization could be a result of doping. We compute the low-doping level that would switch the out-of-plane magnetization to be in-plane.

3.1 Theoretical Details

3.1.1 Chemical and magnetic structures of $CoTiO_3$

We first discuss the difference between the chemical and magnetic structures of bulk cobalt titanate. The compound $CoTiO_3$ is reported to have an ilmenite crystal structure with trigonal space group $R3^-$, which consists of alternating layers of corner sharing CoO_6 and TiO_6 octahedra, stacked along the c-axis in the hexagonal setting, as shown in Fig. 3.1(a) [25, 47]. The lattice can be seen as hexagonal with $a = b = 5.06$ Å and $c = 13.91$ Å, or $a = 5.48$ Å and $\theta = 55$ in the rhombohedral setting. The Co, Ti and O atoms are located at the Wyckoff positions (0,0, 0.355), (0, 0, 0.146) and (0.316, 0.021, 0.246), respectively [21].

The $CoTiO_3$ magnetic configuration is reported as “G-type" antiferromagnetic ordering below the Néel temperature of 38 K [21, 25, 47, 48, 50]. This configuration consists of ferromagnetically coupled hexagonal ab-planes, antiferromagnetically coupled along the c-axis, as shown in Fig. (3.1)(b). It should be noted that in order to reproduce the periodicity of this magnetic cell in the spin-polarized formalism implemented in the *ab initio* codes, building a cell larger than the chemical rhombohedral or hexagonal cells is needed.

Although the c-axis doubled hexagonal cell, which consists of 60 atoms, is a straightforward candidate, there is a primitive magnetic cell of just 20 atoms that

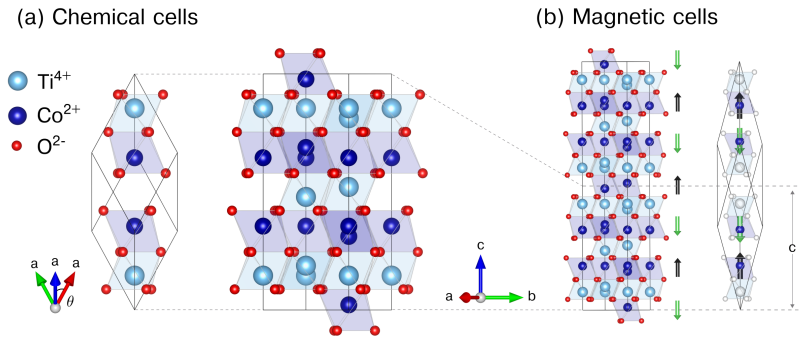

Figure 3.1: Chemical and magnetic unit cells of bulk $CoTiO_3$. (a) The rhombohedral and hexagonal cells that reproduce the crystalline chemical periodicity. (b) Conventional and primitive magnetic cells exemplified using the experimentally found "G-AFM" magnetic configuration. Ferromagnetic hexagonal *ab* planes of cobalt are antiferromagnetically coupled in the (doubled) hexagonal *c*-axis. This figure was prepared using the VESTA software [49].

still satisfies this periodicity [24]. It can be defined by means of the transformation

$$\begin{bmatrix} \mathbf{M}_1 \\ \mathbf{M}_2 \\ \mathbf{M}_3 \end{bmatrix} = \frac{1}{3} \begin{bmatrix} 1 & 2 & 2 \\ -2 & -1 & 2 \\ 1 & -1 & 2 \end{bmatrix} \begin{bmatrix} \mathbf{a} \\ \mathbf{b} \\ \mathbf{c} \end{bmatrix}, \tag{3.1}$$

where **a**, **b** and **c** are the hexagonal lattice vectors. We refer to this cell as the primitive magnetic cell, and unless stated otherwise, all the calculations in this chapter are performed using this lattice.

3.1.2 Computational methodology

Electronic delocalization within DFT may lead to an incorrect description of the magnetic properties. In particular, for systems with localized electrons such as *d*-electrons of transition metals acting as dopants in semiconductors or constituting a component of transition metal oxides, Coulomb interaction effects may lead to qualitatively different results [51, 51–53]. The DFT+U method is one approach that aims to correct the tendency of DFT towards itineracy by explicitly correcting the Coulomb interaction with a Hubbard-like interaction for a subset of states in the system [54]. By including the on-site Coulomb interaction U and exchange interaction J terms, the non-integer or double occupation of these states is penalized, thus localizing them in the atomic sites.

Our DFT calculations were performed using the Vienna Ab-initio Software Package (VASP) [55, 56] using the projector augmented wave method (PAW). We employed the GGA for exchange using Perdew–Burke–Ernzerhof (PBE) approach. Extra electron-electron Coulomb interactions are taken into account with the

GGA+U approach in the code. We employed the simplified rotationally invariant approach implemented by Dudarev *et al.* [38], which includes the U and J terms as an effective $U_{\text{eff}} = U - J$ parameter. For brevity, and unless stated otherwise, we refer to the U_{eff} parameter as U. The electrons Co($3p$, $3d$, $4s$), Ti($3p$, $3d$, $4s$) and O($2s$, $2p$) were treated as valence states. Tests using all-electron calculations were conducted to check that the number of valence electrons per element was properly considered, as described in Appendix A.

For most of the calculations presented in this chapter, the total energy of the system was converged with respect to the plane-wave cutoff energy and reciprocal space samplings. The convergence criterion was less than 1 meV/atom, and we found that a plane-wave cutoff of 800 eV, and a Γ-centered 8x8x8 Monkhorst-Pack k-point mesh yield results within the stated precision. In the spin-orbit calculations, where the energy differences are on the order of 10^{-1} meV, additional convergence tests for the magnetocrystalline anisotropy energies (MAE) with respect to the reciprocal space sampling were performed to ensure numerically precise results (see Appendix B).

3.2 Magnetic ordering

To analyze the magnetic structure of cobalt titanate, we perform total energy calculations for various magnetic configurations shown in Fig. 3.2: the G-AFM structure, and the ferromagnetic (FM) and "full-antiferromagnetic" (F-AFM) structures. We find that for all considered (U_{Ti}, U_{Co}) values, the energy ordering of the three structures is the same: the G-AFM configuration is the ground-state, followed by the ferromagnetic FM state, with the full-antiferromagnetic F-AFM structure presenting a considerable higher energy. We refer to the energetic difference between the G-AFM and FM structures as ΔE_1, and label the difference between the G-AFM and F-AFM states as ΔE_2.

In the G-AFM state, all cobalt atoms have a local magnetic moment of $\pm|\mu_{Co}|$, where $|\mu_{Co}|$ ranges from 2.5 μ_B (GGA) to 2.8 μ_B (U_{Ti}=6, U_{Co}=5). This change in the local magnetic moment is also the cause of the localization effect due to the U parameters, which increases the electronic density around the cobalt atoms as the U parameters increase. The calculated magnetic moments are close to the expected S=3/2 value derived from Hund rules, and the slight difference can be attributed to the fact that the local magnetization is numerically computed by integrating in the spherical region given by the Wigner-Seitz radius, which can lead to an underestimation of the measured magnetization. However, it should not be forgotten that due to the hybridization mentioned in the previous section, cobalt presents a non-negligible covalence that modifies the ionic Co^{2+} picture.

The inter-layer superexchange J_1 and intra-layer direct exchange J_2 couplings can be calculated from the energy differences $\Delta E_1 = E_{\text{FM}} - E_{\text{G-AFM}}$ and

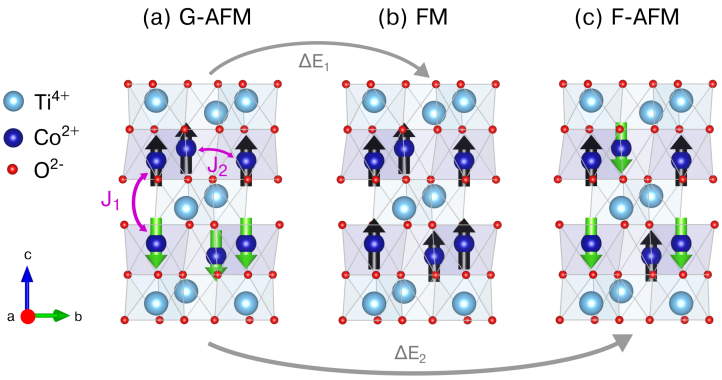

Figure 3.2: (a) "G-type" antiferromagnetic, (b) ferromagnetic and (c) full-antiferromagnetic configurations of ilmenite $CoTiO_3$. J_1 and J_2 are the inter-layer and intra-layer magnetic couplings, respectively, and ΔE_1 and ΔE_2 denote the energetic differences between the configurations. In the (a) and (b) settings, the intra-layer coupling is ferromagnetic, with (a) antiferromagnetic, or (b) ferromagnetic, inter-layer coupling. In the configuration (c), both couplings are antiferromagnetic.

$\Delta \mathrm{E}_2 = \mathrm{E}_{\text{F-AFM}} - \mathrm{E}_{\text{G-AFM}}$. Applying the Heisenberg Hamiltonian

$$\mathrm{H} = -\sum_{ij} J_{ij} \mathbf{S}_i \cdot \mathbf{S}_j \tag{3.2}$$

to the magnetic configurations under analysis yields the following energies per unit cell:

$$\mathrm{E}_{\text{G-AFM}} = E_0 + (+2J_1 - 6J_2)\tilde{S}^2, \tag{3.3}$$
$$\mathrm{E}_{\text{FM}} = E_0 + (-2J_1 - 6J_2)\tilde{S}^2, \tag{3.4}$$
$$\mathrm{E}_{\text{F-AFM}} = E_0 + (+2J_1 + 6J_2)\tilde{S}^2. \tag{3.5}$$

Here, $\tilde{S}$ is the pseudospin 3/2, and J_1 and J_2 are the inter-layer and intra-layer magnetic couplings (given in meV). From the energy differences ΔE_1 and ΔE_2, we get the following expressions for the couplings:

$$J_1 = -\frac{\Delta \mathrm{E}_1}{4\tilde{S}^2}, \tag{3.6}$$
$$J_2 = \frac{\Delta \mathrm{E}_2}{12\tilde{S}^2}. \tag{3.7}$$

This procedure yields approximate values of J_1 = -1.33 meV and J_2 = 1.25 meV in the U_{Co}=U_{Ti}=4.0 eV case. These values have not to be confused with the ones in Refs. [21, 25], which are calculated for different model Hamiltonians and other DFT approaches.

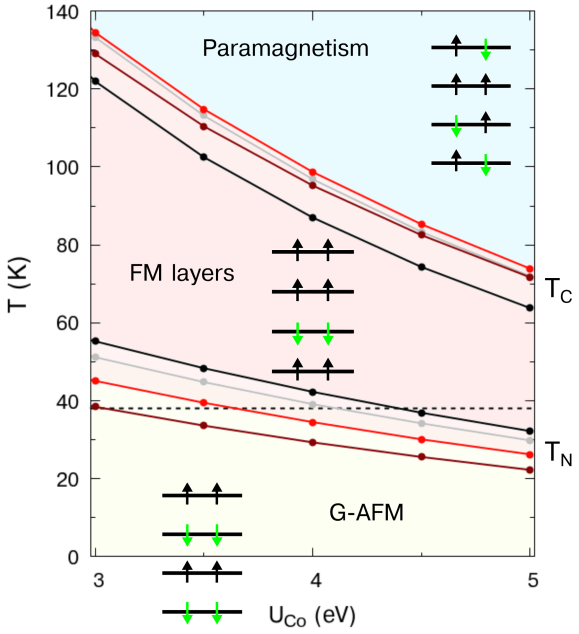

Figure 3.3: Magnetic phases of cobalt titanate with temperature. Energy differences ΔE_1 and ΔE_2 were converted to temperature units. T_N is the Néel temperature, which is related to the breaking of the inter-layer antiferromagnetic ordering, and is shown along the experimental value of T_N=38K indicated by a dashed line. T_C is related to the breaking of the intra-layer ferromagnetic ordering, and represents the starting point of paramagnetic behavior which exists for higher temperatures.

The previously defined energy differences ΔE_1 and ΔE_2 can also be linked to the thermal energies needed to invert the spin ordering of their respective coupling, which causes phase transitions. A critical temperature can be associated with each of these transitions, e.g. in the form of $k_B T_i = \Delta E_i / N_{Co}$. These computed critical temperatures are shown in Fig. 3.3, where a phase diagram of the system behavior is presented. For temperatures lower than the Néel temperature (T_N), the system will exhibit the G-AFM state, which consists of ferromagnetic hexagonal *ab* planes antiferromagnetically coupled along the *c*-axis. When the temperature ranges between T_N and T_C, the antiferromagnetic inter-layer ordering will be broken, but the intra-layer ferromagnetic ordering will still be present. Lastly, T_C indicates the beginning of the fully paramagnetic behavior, where the thermal energy overcomes the in-layer coupling, breaking the ferromagnetic ordering of the layers. Note that the Co ions in the paramagnetic state still present disordered local magnetizations, not being fully spin compensated. These findings suggest that individual layers can be ferromagnetic in the $T_N < T < T_C$ range above the Néel temperature, an interesting result regarding applications that might merit further experimental

work. It is noteworthy that single layers of iron ilmenene, a material with a similar structure to cobalt titanate, have already been exfoliated [26].

3.3 Magnetic anisotropy

We next consider the magnetic anisotropy due to the ferromagnetic cobalt layers in $CoTiO_3$ bulk. In order to determine whether cobalt titanate presents an in-plane or out-of-plane magnetic anisotropy, we first perform total energy calculations including the spin-orbit term as implemented in VASP for a number of spin orientations with respect to the ferromagnetic cobalt layers. The magnetocrystalline anisotropy energy (MAE) is defined as the energetic difference between the lowest energy magnetic configuration and the configuration under analysis, and is given by $\mathrm{MAE}(\theta) = E(\theta)$ - E_z. Here, θ is the polar angle in the hexagonal ac (cartesian xz) plane. We focus our analysis onto this plane because we found that the effect of the in-plane orientation was negligible, varying the MAE in the order of μeV for different values of the azimuthal angle within the hexagonal ab plane.

In the G-AFM setting of the primitive magnetic cell, we calculated the MAE in the GGA and GGA+U approaches. The MAE values using GGA are larger than those for the GGA+U cases because the GGA structure is slightly compressed. In fact, the role of the structural parameters seems key as the MAE for the experimental lattice is even larger. Some comments on the effect of U in the anisotropy are included in Appendix C. We then focus on the MAE per atom in the GGA+U case, as shown in Fig. 3.4(a). We observe that the magnetocrystalline anisotropy is minimum in the out-of-plane hexagonal c-axis, and increases as spins align with the hexagonal ab plane. This tendency is observed in both the GGA and GGA+U approaches, suggesting the easy-axis character of the hexagonal c-axis. The MAE was also calculated for the ferromagnetic configuration and found to be out-of-plane. We also performed all-electron Elk calculations that confirm the out-of-plane MAE (see Appendix B). This finding confirms that the ab layers have a strong out-of-plane character.

In order to understand the angular dependence of the MAE, we fit our results to the expresion

$$\mathrm{MAE}(\theta) = K_1 \sin^2(\theta) + K_2 \sin^4(\theta), \tag{3.8}$$

where K_1 and K_2 are the magnetocrystalline anisotropy constants [57]. Using the total energies per unit cell, our fitting yields values of $K_1 = 0.29$ (0.52) meV and $K_2 = 0.068$ (0.025) meV for GGA+U (GGA) cases. The K_1 value is much larger than the K_2 one, but not negligible for GGA+U. This indicates the strong uniaxial character of the anisotropy.

The element dependence of the anisotropy can also be analyzed by fitting the

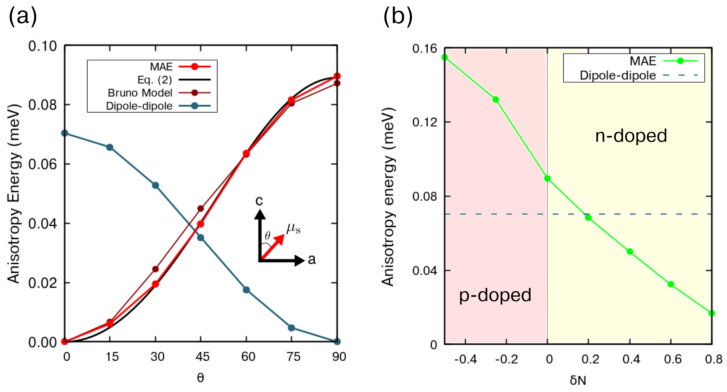

Figure 3.4: Magnetic anisotropy of bulk cobalt titanate. (a) Angular dependence of the anisotropy, where θ changes from the out-of-plane c-axis to the hexagonal ab plane. In red, the MAE is shown as calculated using DFT. In dark red, the Bruno model fitting obtained with the calculated μ_L orbital moments is shown; in black, the fitting to Eq.(3.8); in blue, the magnetic anisotropy due to the dipole-dipole interaction is shown. (b) Magnetic anisotropy at the ab plane ($\theta = 90°$) with respect to the variation of the electron number in the unit cell (δN). The dipole-dipole term is shown in dashed lines. For an electron excess of around 0.2, the MAE term becomes smaller than the dipole-dipole term, so that the total anisotropy becomes in-plane.

MAE to the Bruno model [58] given by

$$\mathrm{MAE}(\theta) = -\frac{\xi}{4\mu_B}(\mu_L^{GS} - \mu_L(\theta)) > 0, \tag{3.9}$$

where $\xi \simeq 50$ meV is the spin-orbit constant, and μ_L^{GS} and $\mu_L(\theta)$ are the orbital magnetic moments of cobalt atoms in the ground-state configuration and in the axis under analysis, respectively. Our fitting to Eq.(3.9) yielded a spin-orbit constant of $\xi \simeq 48$ meV ($\xi \simeq 60$ meV) in the GGA+U (GGA) approach, close to the aforementioned value. These MAE values calculated from the orbital magnetic momenta μ_L using the Bruno model are in great agreement with the directly calculated DFT+U values. This agreement suggests that the MAE could be directly correlated to the angular dependence of the density around cobalt ions in $CoTiO_3$. In the GGA+U approach, we get values of μ_L between 0.16 and 0.19 μ_B, in good agreement with the GGA values in Ref. [59]. By being non-negligible, these μ_L values are pointing to the relevance of spin-orbit coupling in these cobaltates. The μ_L values are noncollinear with μ_S ones when the field is not exactly aligned with the easy axis or the hard plane (see Appendix D.

Previous reports point to an in-plane anisotropy for cobalt titanate [24, 25, 47, 48], which is in contrast to our calculations. In order to understand this discrepancy, we also calculated the anisotropy due to the magnetic dipole-dipole interaction[60].

This interaction is given by the term

$$H_{d-d} = -\sum_{i \neq j} \frac{\mu_0}{4\pi |\mathbf{r}_{ij}|^3} \left(3(\mathbf{m}_i \cdot \hat{\mathbf{r}}_{ij})(\mathbf{m}_j \cdot \hat{\mathbf{r}}_{ij}) - \mathbf{m}_i \cdot \mathbf{m}_j \right), \tag{3.10}$$

where $\mathbf{m}_i$ and $\mathbf{m}_j$ are the local magnetic moments around the interacting cobalt ions pairs, and $\mathbf{r}_{ij}$ is the vector joining the two cobalt atoms. We computed this term from the atomic positions and local magnetic moments derived from the DFT calculations in which the spin-orbit interaction was included. Our results for the GGA+U structure are shown along the MAE in Fig. 3.4(a). In contrast to the spin-orbit term, the dipole term favors in-plane spin orientation, and competes with the MAE term in magnitude. Nevertheless, the total magnetic anisotropy still favors an out-of-plane orientation in our calculations. This effect presumably increases with growing temperature, as the dipole-dipole term (approximately $\propto M^2(T)$) decays faster than the MAE term ($\propto M(T)$) with the spontaneous magnetization [61]. This could lead to potential out-of-plane ferromagnetic layers in the $T_N < T < T_C$ temperature range.

To reconcile our results with experiments, we analyze the effect of doping in the system, see Fig. 3.4(b). This is performed by the addition and the substraction of electrons in the unit cell. Including defects in this compound explicitly implies a different set of calculations beyond the scope of this actual work. We find that removing electrons (p-doping) leads to an increase of the MAE, while adding electrons (n-doping) lowers the MAE even past the dipole-dipole term. This later mechanism could be a consequence of the presence of Ti atoms at some cobalt sites in the sample, as suggested in the experimental literature [47, 62]. Our results indicate that adding 0.2 electrons, which roughly corresponds to 2.5% of cobalt sites being occupated by titanium, could be enough to turn the out-of-plane anisotropy to an in-plane anisotropy, consistent with experiments.

In summary, we find that crystalline bulk $CoTiO_3$ presents a strong out-of-plane magnetocrystalline anisotropy, due to the spin-orbit coupling of cobalt atoms. The value is larger in magnitude to that of pure hcp cobalt [63, 64], a fact that is interesting because cobalt can be seen in this compound as a Co^{2+} ion instead of being metallic. Furthermore, the dipole-dipole interaction is also estimated to be significant in this material due to cobalt ferromagnetic coupling in layers. Summing the two contributions, we observed that the presence of cobalt-titanium anti-site disorder could be responsible of the experimentally observed in-plane anisotropy of the bulk $CoTiO_3$. We further remark that the effect of mesoscopic domains, suggested in the literature [24, 25], may result in domains with in-plane anisotropy. However, it should be noted that domains with an out-of-plane component could also lead to the compensation of the MAE, yielding an in-plane anisotropy, as already shown in magnetic alloys [65, 66].

3.3.1 Conclusions

In this chapter, we analyzed the magnetism of bulk ilmenite cobalt titanate in the DFT+U framework. We found that the G-AFM structure is the ground state of the system with ferromagnetic cobalt layers antiferromagnetically coupled in the *c*-axis. Thus, there are two critical temperatures that correspond to the transition between the G-AFM and ferromagnetic-layered structure, and to the beginning of the paramagnetic phase. The existence of ferromagnetic planes at temperatures above T_N, could potentially lead to interesting magnetic applications when being synthesized as layers.

Our calculations including spin-orbit coupling indicate that the anisotropy would be out-of-plane, a finding in contrast with experiments. However, we found that the presence of 0.2 electrons in the unit cell, which roughly corresponds to 2.5% of cobalt sites being occupated by titanium, could be enough to turn the out-of-plane anisotropy to an in-plane anisotropy, consistent with experiments. We believe that further experimental studies, such as deformation or strain experiments, could further deepen our understanding of the magnetic anisotropy in this material. On the theoretical front, slab and single-layer calculations seem of great interest for future investigations of intriguing thin-film systems.

CHAPTER 4

CHARACTERIZATION OF THE 3*d* TRANSITION METAL ILMENENES

The technology for synthesizing two-dimensional materials has greatly improved in recent years. Since the synthesis of graphene [67, 68], a large number of extensive systems only a few atoms thick have been obtained. The study of these 2D materials has brought new physical phenomena with countless applications into play, like their magnetic properties [69, 70]. Obtaining magnetism in 2D isotropic crystals is forbidden in the Heisenberg model as explained by the Mermin-Wagner theorem [71]: the magnon dispersion is reduced with respect to their 3D counterparts, and it has an abrupt onset, which translates into low thermal agitation and a collapse of the spin order. However, 2D systems with uniaxial magnetic anisotropy are able to withstand thermal agitation, allowing magnetic states in mono- and multi-layer nanostructures.

In the past decades, the study of 2D magnetic properties has been performed on epitaxially grown thin films, in which phenomena such as oscillating exchange coupling [72, 73], giant magnetoresistance [74, 75] and Hall effect [76, 77] have been observed. Nevertheless, the study of the intrinsic magnetic properties of these 2D systems is novel, and most of the materials that have been synthesized today are magnetic van der Waals crystals [69, 70]. In the last five years, non-van der Waals two-dimensional materials have also been synthesized, mainly by exfoliating naturally occurring ores. By liquid exfoliation of natural iron ore hematite (α-Fe_2O_3), Balan et al. [78] synthesized a new 2D material which is called hematene. Contrary to its antiferromagnetic bulk, hematene presents ferromagnetic order. Similarly, other promising material for 2D magnets is ilmenene [26], which has been synthesized using liquid phase exfoliation from titanate ore ilmenite ($FeTiO_3$), as shown in Fig. (1.2).

In this chapter, motivated by the synthesis of iron ilmenene, we characterize the whole family of ilmenene-like 3*d* transition metal titanates ($TMTiO_3$, TM = V to Zn), setting a first theoretical basis for this group of compounds that could be exfoliated in the near future. Within the framework of the density functional theory, we systematically analyze the crystalline structure of these compounds, finding that most of the ilmenenes exhibit triangular symmetry for TMs on both sides of a Ti-Ti hexagonal graphene-like sublattice. In the chromium and copper ilmenenes, we find structural distortions of Jahn-Teller-like origin. Our electronic structure calculations reveal that most of these compounds are magnetic semiconductors which have TM layers antiferromagnetically coupled. The calculations including spin-orbit interactions show a strong magnetic anisotropy, with the magnetization being oriented out-of-plane (in-plane) below (above) the half-filling of the TM electronic 3d shell. The presence of out-of-plane anisotropy in some of these compounds suggests potential applications for spintronics in thin layers and 2D materials.

4.1 Theoretical details

To study the structural, electronic and magnetic properties of ilmenene-type materials, we use the projector augmented wave method (PAW) implemented in the Vienna Ab-initio Software Package (VASP) [55, 56]. For the exchange and correlation potential we use the Perdew-Burke-Ernzerhof form of the generalized gradient approximation (GGA), with the formulation of Dudarev [38] for GGA+U calculations. The Hubbard U parameters for each element are chosen based on the available literature on transition metal oxides [53], and are shown in Table 4.1 with the considered valence states. A test calculation of the partial density of states (PDOS) of cobalt titanate using the HSE06 hybrid functional shows that including a U parameter in the oxygen p-orbitals is needed to correctly describe the electronic structure. This finding is in agreement with previous investigations concerning titanium oxide and hematite [79–84]. All calculations are performed with a well-converged plane-wave cutoff energy of 800 eV, a gamma-centered 4x4x1 Monkhorst-Pack k-point mesh, and a Fermi smearing of 20 meV. Atomic coordinates are relaxed until forces in all directions were smaller than 0.5 meV/Å. An energy convergence criterion of 10^{-7} eV for the energy is used. Further tests using even a larger plane wave cutoff up to 1000 eV and 6x6x1 k-point mesh do not modify the presented results. Differences in local charges and local magnetic moments are univocally analyzed using the Bader method [85, 86]. By including the spin-orbit coupling, additional tests are performed to converge the magnetocrystalline anisotropy energy with respect to the Brillouin Zone sampling.

The d-metal ilmenene sheets are obtained by cutting their respective bulk titanates ($TMTiO_3$, TM = V to Zn) in the hexagonal [001] direction. For the iron ilmenene $FeTiO_3$, transmission electron microscopy measurements confirm that the

4.1: Valence electron states and U parameters employed on each element of the TM titanates.

Element	Valence states	U
O	2s, 2p	6.6
Ti	3p, 3d, 4s	3.9
V	3p, 3d, 4s	3.5
Cr	3p, 3d, 4s	3.5
Mn	3p, 3d, 4s	4.0
Fe	3d, 4s	4.0
Co	3d, 4s	4.5
Ni	3d, 4s	4.5
Cu	3d, 4s	5.0
Zn	3d, 4s	5.0

2D structure are planes in this direction [26]. The layer structure is shown in Fig. 4.1. For all the compounds under analysis, two different layer-ilmenenes are tested: titanium and transition metal terminated ilmenene layers. This work focuses on the TM ended layers because they are found to be more stable for all the materials under analysis.

4.2 Crystalline structure and distortions

The structure of the TM ilmenenes is graphically depicted from two viewpoints in Fig. 4.1. After structural relaxations, we find that most of the compounds keep the input symmetry, except for chromium and copper ilmenenes, which show structural deformations of the perfect lattice due to the Jahn-Teller effect (see Fig. 4.1(b)). The orange area in panel (a) denotes the chemical cell that reproduces the crystalline structure of the ilmenenes when periodically repeated. We calculate magnetic configurations using a larger 2x2x1 magnetic cell. For chromium and copper titanates, due to structural distortions, the unit cell and the magnetic cell coincide. In the distorted compounds, the two in-plane lattice vectors become slightly different: for the chromium case $a = 10.57$ Å and $b = 10.00$ Å, and for the copper case $a = 10.44$ Å and $b = 10.21$ Å. Note that these ilmenenes become anisotropic. Overimposed on the global lattice distortions, the inner atomic distortions become more noticeable. For instance, the pairs of largest-smallest distances are 6.0 Å - 3.9 Å and 5.4 Å - 4.8 Å for Cr and Cu ilmenenes, respectively. The large 1D anisotropy of these two Jahn-Teller–like distorted ilmenenes is shown by the stripes of the green and violet areas in Fig. 4.1 (b).

A summary of the interatomic distances of the TM titanates is shown as a function of the elements across the period in the periodic table in Fig. 4.1. We find that the horizontal distance between transition metals in the same layer l_{TM-TM} increases from V to Mn, then decreases until Ni, and finally increases for the brass

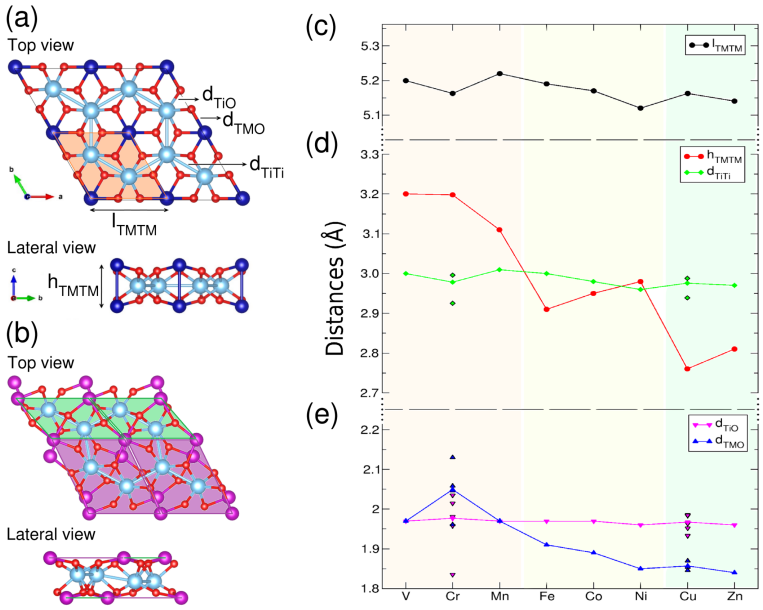

Figure 4.1: Magnetic unit cell for transition metal ended ilmenene-like systems: (a) symmetric for most ilmenenes, and (b) distorted for chromium titanate $CrTiO_3$. The color code of the atoms is as follows: TM (Cr) atoms in blue (purple), titanium in cyan, and oxygen in red. The orange area in panel (a) represents the smaller chemical cell. For chromium and copper titanates, the chemical and magnetic cells coincide. Calculated interatomic distances: (c) horizontal TM-TM distance l_{TM-TM}, (d) layer height h_{TM-TM} and Ti-Ti distances, and (e) Ti-O and TM-O distances. For the chromium and copper ilmenenes we present an average of the distances in their distorted structures.

metals Cu and Zn. The height distance between metals in different layers h_{TM-TM} generally decreases. The distances involving Ti in the Ti-Ti and Ti-O bonds remain nearly constant, while the TM-O distances decrease. In essence, TM-ilmenenes can be thought of as a solid network formed by Ti and O atoms on which the TM atoms attach on both sides. For the Cr and Cu ilmenenes showing structural distortions, the TM-TM distances have two values because the triangular symmetry is broken, and the Ti-O distances are split into several values as shown by the extra marks in the lower panel of Fig. 4.1.

We find that in comparison with their bulk counterparts, TM ilmenenes are compacted along the c direction, so that a two-dimensional hexagonal layer of titanium ions is formed similar to graphene. The Ti-Ti sublattice in ilmenenes remains almost constant with the distances varying within 3%. [1] This compression for the iron ilmenene has a minimum height about 2.91 Å, in agreement with another work [26]. The theoretical value of 2.59 Å for the interplanar space corresponding to the $(11\bar{2}0)$ and $(\bar{2}110)$ lattice spacing compares well with the experimental one ($\sim$ 2.53 Å) [26], which is also supporting our calculations since the interatomic distances depend on the chosen U values. For cobalt titanates, a layer thickness of 4.03 Å has been reported [1] in bulk, which decreases to 2.95 Å in the ilmenene layer, while the horizontal distance between cobalt atoms in the same layer expands slightly from 5.06 Å in bulk to 5.17 Å in the layer. The significant changes in the height distances are due to the layer being decorated with half of the TM atoms than in the corresponding bulk, in order to keep the stoichiometry. It seems that the ilmenene layers depart largely from those found in ilmenites and not only their structural properties but their magnetic ones are thus deserving a thoroughly study.

4.3 Electronic properties: magnetic semiconductors

We now focus on the electronic structure of ilmenenes and find that they show a gap opening that is linked to their stability. The calculated electronic band gaps range between 1.8 and 4 eV, as displayed in Fig. (4.2) (a), with values that are typical for semiconductors. The gaps are increasing when going from V to Mn, and they are oscillating for Fe, Co and Ni. In general, the values are smaller than the gap for TiO_2 in the rutile bulk phase ($\sim$ 3.2 eV). Note that the Mn and the Co ilmenenes remain within the same order of the TiO_2 gap values. These trends follow the filling of 3d TM electronic levels as discussed below.

The TM atoms in the ilmenene compounds show local magnetic moments, which are calculated using the Bader method, and are shown in panel (b) of Fig. 4.2.

[1] However, the chromium titanate layer does not show the fully compacting behavior to a flat titanium sheet due to distortions(see Fig. 4.1(b)).

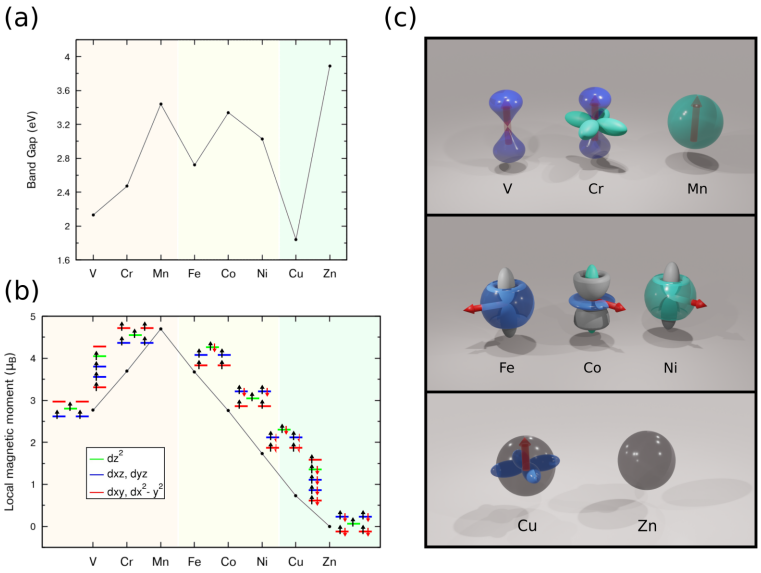

Figure 4.2: (a) Electronic band gaps for TM ilmenenes. Vertical lines separate different regions with TM below half-filling, TM above half-filling, and brass metals. (b) Calculated local magnetic moment around transition metal atoms. For each compound, the electronic filling model of the ground state is also shown. Red levels represent the in-plane $d_{x^2-y^2}$ and d_{xy} orbitals; green, the out-of-plane d_{z^2} orbital; and blue, the d_{xz} and d_{yz} orbitals with in- and out-plane components. (c) Orbital models of the local magnetization in 3d TMs and brass metals within ilmenenes. Blue and green regions denote spin polarized regions; grey, spin compensated ones.

The calculated values are close to the ones expected by applying the Hund rules to isolated ions. Furthermore, the local magnetic moment as a function of atomic number follows a Slater-Pauling–like rule, increasing from vanadium to manganese, then decreasing until it vanishes for zinc. Thus, the 3d ilmenenes behave similarly as being magnetic semiconductors.

The band structures and the PDOS projected onto the transition metal atoms are collected in Appendix E. From their analysis, an electronic filling model for each TM ilmenene is presented in Fig. 4.2(b). We find that the orbitals can be classified into three groups: (i) out-of-plane d_{z^2}, (ii) in-plane $d_{x^2-y^2}$ and d_{xy}, and (iii) mixing in- and out- of plane contributions for d_{xz} and d_{yz}. The $d_{x^2-y^2}$ and d_{xy} orbitals are highly hybridized, as the d_{xz} and d_{yz} orbitals are. Because the in-plane degenerated energy levels of chromium and copper titanates are being partially occupied, they are held responsible for the Jahn-Teller–like distortions in these structures, where a splitting of these otherwise degenerated orbitals is observed under distortions.

All these electronic trends can be better understood following the orbital model in real space for each case, as shown in Fig. 4.2 (c). Below half-filling, we show how the magnetic moment increases in correlation with the gap values. For next elements, above half-filling, the Fe case becomes similar to the Ni one which has a weaker spin distribution. In between, we find the Co ilmenene with a large in-plane spin distribution has also an out-of-plane component that cannot be neglected, an extra component that is related to the complexity added to this case when trying to write down a single spin hamiltonian. For brass metals, the local magnetization is nearly screened having a spin compensated cloud around the brass metal centers. This model is going to be interesting in the discussion of magnetic anisotropies below. For instance, we note that the spin distribution is not anisotropic for the case of Cr (Cu) having one-electron less below a half-filled (filled) $3d$ shell.

4.4 Magnetism

4.4.1 Magnetic Order

We next consider the magnetic behavior of the ilmenene-type materials, and calculate the total energies of the magnetic configurations shown schematically in Fig. 4.3. We find that, with the exception of ferromagnetic copper and spin-compensated zinc titanates, the ilmenenes show antiferromagnetism between the 2D TM layers in the so-called AFM-1 configuration.

The magnetic configurations in Fig. 4.3 are used to fit the Heisenberg Hamiltonian

$$H = -\sum_{ij} J_{ij} \tilde{\mathbf{S}}_\mathbf{i} \cdot \tilde{\mathbf{S}}_\mathbf{j} \tag{4.1}$$

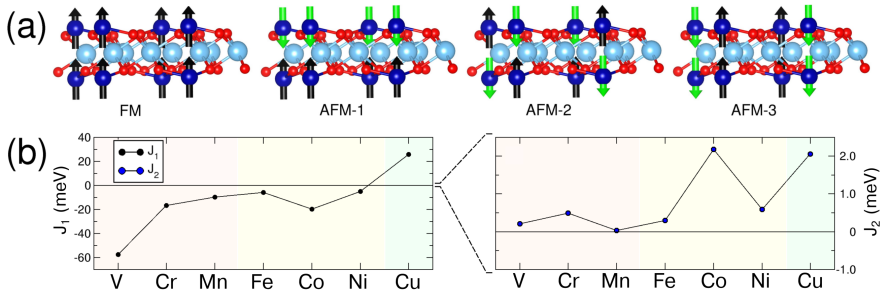

Figure 4.3: (a) Magnetic ordering configurations of TM ilmenenes: "FM" Ferromagnetic, "AFM-1" antiferromagnetic by layers, "AFM-2" and "AFM-3" antiferromagnetic. (b) Couplings between both layer sides (J_1), and within the same side layer of TM ions (J_2).

where the $\tilde{S}_i$ is the pseudospin of each isolated atomic species (e.g: $\tilde{S} = 3/2$ for Co), and the J_i with $i = 1, 2$ are the inter-layer ($i = 1$) and intra-layer ($i = 2$) magnetic couplings schematically depicted in 4.3. The magnetic couplings are computed from the energy differences $\Delta E_1 = E_{FM} - E_{AFM_1}$, $\Delta E_2 = E_{AFM_2} - E_{AFM_1}$.

The fitted J_i values are shown in Fig. 4.3 (b). The inter-layer coupling is the leading interaction because J_1 is an order of magnitude larger than J_2. The inter-layer coupling J_1 is negative for most of the ilmenenes, that indicates a preference for antiferromagnetism. The intra-layer coupling J_2 is positive in all cases, and the compounds favor intralayer ferromagnetism. Since the coordination of the TM atoms on each layer side changes from being hexagonal in bulk to triangular in the layer, the structural differences between bulk and two dimensional titanates mentioned above play an important role in the magnetic ordering. It is noteworthy that the manganese ilmenene even favors ferromagnetism within layers in contrast with its antiferromagnetic bulk counterpart.

4.4.2 Magnetic Anisotropy

We last study the magnetic anisotropy of d-metal ilmenenes. The spin-orbit interaction couples the spin magnetic moment to the crystal lattice, which means that some spin orientations are more stable than others. The magnetocrystalline anisotropy energy (MAE) is defined as the energetic difference between two magnetic configurations with different spin orientations. We calculate the total energy of the ilmenenes for a number of spin orientations, and find that, anisotropy-wise, ilmenenes can be classified in two groups: out-of-plane ilmenenes, in which the spin magnetic moment is aligned in the *c*-axis, and in-plane ilmenenes, with the spin aligned in any of the directions along TM-Ti bonds projected in the plane, as shown in Fig. 4.4. Due to symmetry around TM atoms, there are six such equivalent directions in the *ab* plane. The vanadium, chromium and manganese titanates in addition to copper ones have an out-of-plane anisotropy, and the magnetization

in iron, cobalt and nickel titanates is oriented in-plane. These MAE trends agree with the electronic filling model, in which below half-filling TMs the electrons near the Fermi level are those that include an out-of-plane component, and for iron, cobalt and nickel titanates they are mainly in-plane.

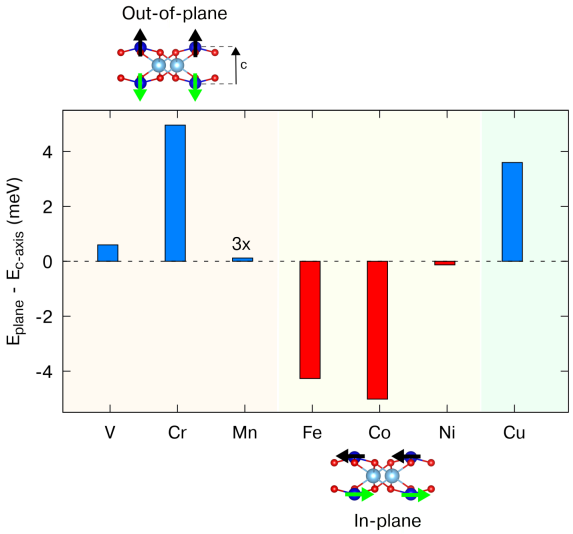

Figure 4.4: Magnetocrystalline anisotropy energy of the transition metal ilmenenes. In blue, compounds with out-of-plane anisotropy; in red, with in-plane magnetic moments. For the case of manganese titanate, the magnitude was enhanced by a factor of 3 to make it visible in the shown range.

The obtained MAE values range between several orders of magnitude from 10^{-2} meV up to tenths of meVs because the spin-orbit interaction varies greatly for the different ilmenenes. The chromium, iron and cobalt titanates have a strong MAE of around 5 meV, and in the case of the vanadium and nickel layers, this value is still large about 0.6 and 0.13 meV, respectively. The manganese titanate has the smallest anisotropy ($\sim$ 0.04 meV) because the orbital magnetic moment is nearly fully quenched. This finding summed to having the energetic difference between the magnetic AFM-1 and AFM-2 configurations of the manganese titanate being very small (around 0.25 meV) points to non-collinear magnetic configurations, a topic that might merit future experimental investigation on this specific layer, but being beyond the actual scope of the paper. Furthermore, the iron ilmenene is also a particular 2D layer because it shows a strong in-plane anisotropy, contrary to the ilmenite bulk with a non-negligible out-of-plane component.

We observe a noticeable trend for the magnetic anisotropy. Below half-filling, the V and Cr ilmenenes exhibit out-of-plane anisotropy, while the half-filled manganese ilmenene has a very small MAE. Above half-filling, most the compounds have an in-

plane anisotropy. In fact, these trends in anisotropy follow the levels depicted in Fig. 4.4 (c). For V and Cr ilmenenes, it shows that the spin density is perpendicular to the plane. The spin density in manganese ilmenene is isotropic, and this correlates with its low MAE. Above half-filling, the spin density of Fe, Co and Ni ilmenenes lies in-plane, in agreement with their in-plane MAE. The case of Cu ilmenene shows out-of-plane anisotropy even if the spin density lies in-plane, a finding that can be explained by the out-of-plane changes in the orbitals when the spin-orbit coupling term is included with the distortions.

We next bring the magnetic results on magnetic ilmenenes into contact with experimental facts. Note that Fe ilmenenes can be obtained by exfoliation and deposited on substrates for some experimental setups [26, 78]. Then, further measurements on the magnetic properties of the Fe ilmenenes can be today performed in line with our theoretical results. Furthermore, we have studied Co ilmenenes that could be interesting as they can behave in a similar way to study magnon physics in two dimensions as their bulk counterpart is already being used [1, 24, 25]. In fact, Cr ilmenenes seem to become key as they are candidates to show out-of-plane anisotropy when in the form of ultrathin layers. These findings are suggesting the future use of TM ilmenenes in spintronics devices for injecting magnons and study magnetism in exfoliated 2D magnetic layers.

4.5 Conclusions

In this chapter, we have analyzed the structural, electronic and magnetic properties of TM ilmenene-like systems. Our calculations reveal that most of the layer materials under analysis present a triangular crystalline structure for TMs, with an ironed compression of the internal titanium ion layer with respect to its bulk. The chromium and copper ilmenenes exhibit notable structural distortions, which seem to have a Jahn-Teller–like origin. All the compounds studied have been found to be magnetic semiconductors with band gaps in the range between 1.7 and 4 eV. The magnetic ground state is mainly antiferromagnetic between layers, and ferromagnetic and spin-compensated for $CuTiO_3$ and $ZnTiO_3$, respectively. Furthermore, spin-orbit calculations revealed that TM ilmenenes can be divided into two groups: out-of-plane ilmenenes, for less than half-filling of the 3d bands, and in-plane ilmenenes, above half-filling of these levels, with the spin aligned in the TM-titanium directions projected in the hexagonal plane. We believe that this family of materials paves the way to other types of promising magnetic 2D candidates with potential applications in the field of spintronics.

CHAPTER 5

STRAIN-INDUCED MAGNETIC ANISOTROPY TRANSITIONS IN LAYERED $CaMn_2Bi_2$

$CaMn_2Bi_2$ is a layered semiconductor that has been reported to exhibit large magnetoresistance and has been proposed to be a candidate for a hybridization gap semiconductor [87]. $CaMn_2Bi_2$ has a hexagonal structure, composed of layers of manganese and bismuth tetrahedra, separated by calcium layers (see Fig. (5.1)). The manganese atoms are structured in a so-called *puckered* honeycomb, and they are antiferromagnetically aligned in the magnetic ground state configuration. Regarding the electronic structure, $CaMn_2Bi_2$ has a band gap of a few meV [87, 88], and could exhibit topological properties [89].

We have recently started a collaboration with an experimental group that has been studying second harmonic generation using lasers. After thermal cycling the sample, they observed one of two possible signals after each cycling, which could be a sign of a competition between two magnetic states with close energies. Aiming to explain the observed phenomena, we theoretically studied the fundamental magnetic properties of this compound. We determined the magnetic ground state of the compound, which we confirmed to be the antiferromagnetic structure. We then studied the MAE, and found that $CaMn_2Bi_2$ has an in-plane anisotropy, with the zigzag-x axis being the easy-axis. When applying strain to the compound, which in experiments is done by exciting certain vibration modes with incident light, we found that the easy-axis changes from the zigzag-x to the armchair-y direction.

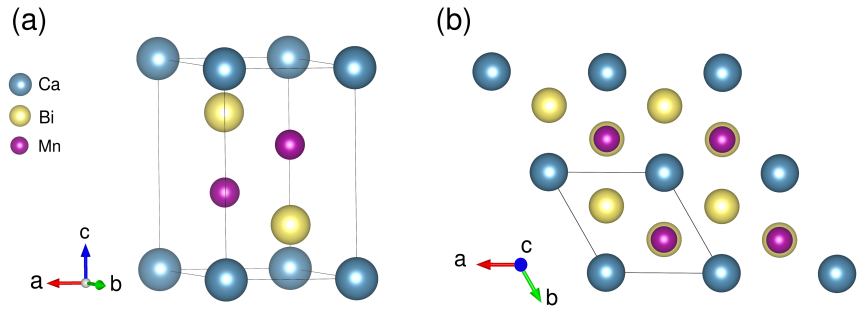

Figure 5.1: (a) Lateral view and (b) top view of the crystal structure of $CaMn_2Bi_2$. Manganese atoms are displayed in purple, and calcium and bismuth atoms are represented in cyan and yellow, respectively. The manganese and bismuth atoms form hexagonal sublattices that are rippled in the c-axis, as is clearly seen in panel (b).

5.1 Numerical details

The total energy calculations in this chapter have been performed in the DFT+U approach. We have used the projector augmented wave method (PAW) implemented in the Vienna Ab-initio Software Package (VASP) [55, 56]. For the exchange and correlation potential, we use the Perdew-Burke-Ernzerhof form of the generalized gradient approximation (GGA), which is further corrected with the Coulomb U parameter following the GGA+U formulation of Dudarev [38]. We performed a test calculation of the partial density of states (PDOS) using the HSE06 hybrid functional and compared it to the GGA and GGA+U calculations. We found that it is necessary to include the correction terms $U_{Mn} = 4$ eV and $U_{Bi} = 3$ eV for a correct qualitative description of the electronic structure of $CaMn_2Bi_2$.

All calculations were performed with a well-converged plane-wave cutoff energy of 700 eV, a gamma-centered 15x15x8 Monkhorst-Pack k-point mesh, and a Fermi smearing of 20 meV. Atomic coordinates were relaxed until forces in all directions were smaller than 0.5 meV/Å. An energy convergence criterion of 10^{-7} eV was used. The atomic valence configuration for Ca, Mn and Bi are $3s^2 3p^6 4s^2 4p^{0.01}$, $4s^2 3d^5$ and $6s^2 6p^3$, respectively.

5.2 Magnetic order

We first study the Heisenberg spin exchange term that is responsible for the magnetic order of the compound. In $CaMn_2Bi_2$, due to the crystalline symmetry, the strength of the exchange coupling J_e is the same for all the Mn-Mn interactions

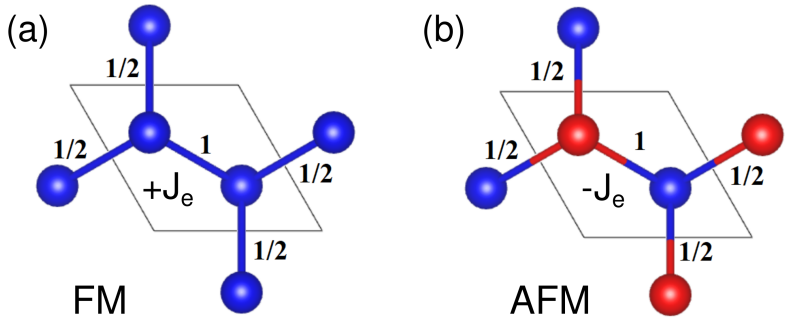

Figure 5.2: Ferromagnetic and antiferromagnetic configurations of the 1x1 $CaMn_2Bi_2$ cell. The blue and red spheres represent the spin-up and spin-down magnanese atoms, respectively. To compute the exchange coupling terms, the interaction with the first neighbors in the adjacent cells is taken into account.

(see Fig. (5.2)). Therefore, we can use the following Heisenberg Hamiltonian

$$H_{Ex} = -\sum_{i,j} J_e \mathbf{S}_i \cdot \mathbf{S}_j. \tag{5.1}$$

In this approach, the total energies of the ferromagnetic (FM) and antiferromagnetic (AFM) configurations in Fig. (5.2) are given by

$$E_{FM} = E_0 - 4(\frac{1}{2} J_e S^2) - J_e S^2 = E_0 - 3J_e S^2, \tag{5.2}$$

$$E_{AFM} = E_0 + 4(\frac{1}{2} J_e S^2) + J_e S^2 = E_0 + 3J_e S^2, \tag{5.3}$$

where E_0 is the total energy of the non-magnetic configuration, and $S = 5/2\ \mu_B$ is the spin around each manganese atom. To obtain these expressions, the interaction in adjacent cells has to be taken into account, because those atoms are also first neighbors to the Mn atoms in the reference cell.

We find that the ground state of $CaMn_2Bi_2$ is the antiferromagnetic configuration. In the 1x1x1 cell, the energy difference between the ferromagnetic and the antiferromagnetic configurations is 208 meV. Subtracting equations (2) and (3) yields the following expression for the exchange coupling J_e:

$$J_e = \frac{E_{FM} - E_{AFM}}{6S^2} = -16.68\text{meV}, \tag{5.4}$$

which is negative, indicating the preference of the system to show antiferromagnetic coupling between manganese atoms.

5.3 Strain-induced magnetic anisotropy change

By including the spin-orbit coupling, we then study the magnetocrystalline anisotropy energy of layered $CaMn_2Bi_2$. After computing the total energy of the compound with the spin aligned in different crystallographic axes, we have determined that the easy axis is the zig-zag x-axis. The energy needed to align the spin out-of-plane is 2.4 meV, a value that is about a hundred times larger than the MAE difference with the armchair y-axis, which is on the order of 0.02 meV.

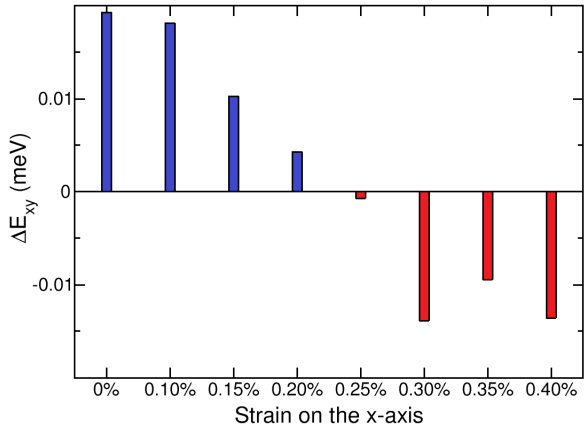

Figure 5.3: Energy difference between x and y-directions with respect to the easy axis. Blue bars indicate the zigzag-x direction for the AFM order parameter is preferred, and red bars indicate the armchair-y direction for the AFM order parameter is preferred. Note that by having strain as in experiments, the difference energy value changes sign around 0.25 %, indicating a change in the in-plane magnetic moment direction.

We also studied the effect of strain in the magnetic anisotropy of $CaMn_2Bi_2$. In Fig. (5.3) we show the MAE difference between the x and y directions while applying strain in the zigzag-x direction. We find that with a strain of around 0.25 %, the easy spin orientation of the crystal changes from the x-axis to lie along the armchair-y direction. When increasing the strain in the x-axis above 0.4 %, the MAE difference increases and favors the y-axis as the easy axis. This strain-dependent behavior of the anisotropy could be used as a way to control the spin orientation of $CaMn_2Bi_2$ at will, which could lead to potential applications. The switching of magnetization in-plane is also interesting for their control by lasers, as some of the light-excited phonons evolve in some of these directions.

5.4 Conclusions

In this chapter, we carried out a theoretical study on the magnetism of $CaMn_2Bi_2$. We computed the magnetic ground state of the compound, with the manganese atoms antiferromagnetically coupled in the puckered honeycomb sublattice. In addition, we studied the spin-orbit coupling, and found that $CaMn_2Bi_2$ has an in-plane magnetic anisotropy, and that the x-axis is the easy-axis. Lastly, we applied strain to the material, and observed that above a small of strain, the easy-axis of the system changes from being in the zig-zag x-axis to the armchair y-axis. This strain-dependent spin behavior deserves further investigation, since it could have interesting applications.

Part II

Excitons in TDDFT

CHAPTER 6

INTRODUCTION

Excitons are bound electron-hole pairs that are created when a semiconducting or insulating material is energetically excited. When an electron in a solid becomes excited (for example, by absorbing a photon), it goes from the valence to the conduction band, leaving a positively charged hole behind. This hole is a particle with positive charge, and therefore, an attractive Coulomb interaction between the conduction electron and the hole can lead to a bound-state similar to the hydrogen atom [90]. Excitons are neutral quasiparticles that can move through the crystal, and carry a momentum $\mathbf{k}$, but no net electric charge (see Fig. 7.1(a)). One of the main features of excitons is observed in the optical absorption spectra of materials with a band gap: even though it could be expected those materials not to present optical absorption until the photon energy is above E_{Gap}, sharp discrete absorption peaks appear below the energy gap. Using the analytic Wannier model [91], which can be derived from perturbation theory [1], the exciton energy levels arise as a Rydberg series inside of the band gap (see Fig. 7.1(b)).The exciton binding energy (E_B) is the energetic difference between the lowest excitonic level and the band gap, and gives a measure of how bound the electron and hole are. Based on the binding energy, two main types of excitons exist: Wannier excitons, with a low binding energy and high spatial delocalization, and Frenkel excitons, which are tightly bound and localized around one atomic site [90, 93]. Even though the single electron-hole picture can give a qualitative image of excitons, it should be noted that in reality excitons are collective effects that imply the superposition of the excitation of different particles in the crystal, which makes it challenging to study.

Excitons have important implications in a wide range of solid-state phenomena,

[1] If one assumes the band structure to only consist on one conduction and one valence band, both parabollic [92].

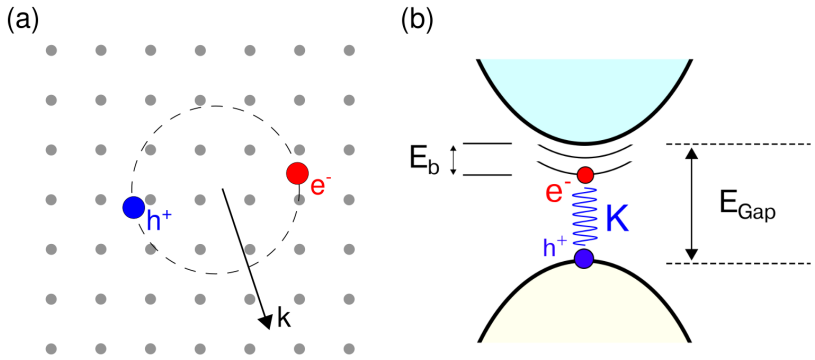

Figure 6.1: (a) Spatial representation of an exciton in a crystal lattice. (b) Band structure sketch of an exciton: excitons can be understood as discrete energy levels that appear below the optical gap, due to the electron-hole interaction. Here, K represents the Coulomb interaction, and E_B is the exciton binding energy, given by the subtraction between the gap energy E_{Gap} and the lowest excited state inside the gap.

and heavily determine the optical properties of semiconducting and insulating materials. An exciton can decay when the electron and hole recombine, emitting a light in the process, which is known as photoluminescence [94, 95]. Therefore, excitons play an important role in the optical properties of materials and are crucial for the design of novel materials such as semiconductors for optoelectronics applications like solar cells and LEDs [96]. For example, low exciton binding energies in perovskite solar cells promote the electron-hole separation and enhance power conversion efficiencies in these devices [97].

The correct description of excitation phenomena in matter is a challenging task of material science. The design of novel man-made materials with desired properties relies upon the capability to accurately predict their electronic structure, but calculations for interacting electrons are much more challenging than those of independent electrons. Over the last two decades, Time Dependent Density Functional Theory has proven to be very successful for the calculation of neutral excitations both for finite and extended systems and it is often considered as the computational cheaper but rigorous alternative to the state-of-the-art MBPT [98–101]. Excitonic effects in semiconductors and insulating materials have been successfully described by the Linear response formalism of TDDFT, solving a Dyson type equation to obtain the density response function which yields good looking optical spectra of several materials [100, 102]. On the other hand, a completely equivalent approach based on the same formalism reformulates the equations into an eigenvalue problem allowing a direct determination of exciton binding energies [103–105]. Originally for finite system, these equations were known as the Casida equations [106] and were later extended to periodic solids [107]. In the two methods, excitonic features are correctly captured using the family of exchange-correlation

kernels known as long-range corrected (LRC) kernels; however, these kernels are not capable to produce simultaneously good looking spectra and accurate exciton binding energies [105]. In other words, when a material dependent α parameter in the LRC-type kernel is fitted to provide a good optical spectra using ab-initio calculations, the same parameter will fall by more than an order of magnitude short in the estimation of binding energies. One of the biggest problems of these kernels is that the main contribution towards exciton binding has a singular term ($\mathbf{q}$=0), which is an ill-defined [108, 109].

Lately, hybrid approaches between TDDFT and the Bethe-Salpeter Equation (BSE) equation have been proposed [92, 110] with success having an affordable computational cost. Furthermore, a hybrid exchange-correlation term can be considered by mixing an adiabatic TDDFT kernel with screened exact exchange (SXX), so that good exciton binding energies were obtained in conjunction with optical spectra [111, 112]. In fact, the head-only SXX kernel including the divergent term $\mathbf{q}$=0 yielded identical binding energies to the full kernel [111]. These findings indicate that the singular term is still crucial in these approaches, and that it should be studied in detail when dealing with exciton calculations.

In this block of the thesis, we carefully study the effect of the singular long-range Coulomb term on the calculation of exciton binding energies. On the one hand, in the pure TDDFT framework, we report the absence of a correction term $\mathbf{C}_{c\mathbf{k},v\mathbf{k}}$ that has to be included when applying the commutator relation that is often used to deal with singularities [109]. We compute the magnitude of this term for set of semiconductors, and find that it is often larger than the regularized singular term itself, which could help explain the discrepancy between the absorption spectra and exciton binding energy calculations. On the other hand, in the hybrid framework, we propose a Wigner-Seitz Truncated SXX kernel (WS-SXX) with a well-defined analytical term in the optical limit ($\mathbf{q}$=0). We furthermore analyze the performance of the kernel with respect to the different convergence parameters, and compare it with the state-of-the-art methods in the field.

CHAPTER 7

NUMERICAL METHODS

7.1 Time Dependent Density Functional Theory

While DFT succesfully performs calculations for many electronic systems, it can only be used to describe ground-state properties of these systems (such as total ground-state energies, electronic density distributions, bond lengths and bond angles, lattice constants ...) [113, 114]. Time-dependent density functional theory is a generalization of ground-state DFT that allows us to describe the behavior of quantum systems that are not in the ground state or in an equilibrium state. Analogously to DFT, TDDFT replaces the time-dependent electronic wavefunction by the time-dependent electron density $n(\mathbf{r}, t)$ as its working magnitude. TDDFT is based in two fundamental theorems, which are related to the Hohenberg-Kohn theorem and to the Kohn-Sham equations, respectively:

Runge-Gross theorem [115]. *Two densities $n(\boldsymbol{r}, t)$ and $n'(\boldsymbol{r}, t)$, evolving from a common initial many-body state Ψ_0 under the influence of two different potentials $v(\boldsymbol{r}, t)$ and $v'(\boldsymbol{r}, t) \neq v(\boldsymbol{r}, t) + c(t)$ (both assumed to be Taylor-expandable around t_0), will start to become different infinitesimally later than t_0. Therefore, there is a one-to-one correspondence between densities and potentials, for any fixed initial many-body state.*

Van Leeuwen theorem [116]. *For a time-dependent density $n(\boldsymbol{r}, t)$ associated with a many-body system with a given particle-particle interaction $w(|\boldsymbol{r} - \boldsymbol{r}'|)$, external potential $v(\boldsymbol{r}, t)$, and initial state Ψ_0, there exists a different many-body system featuring an interaction $w'(|\boldsymbol{r} - \boldsymbol{r}'|)$ and a unique external potential $v'(\boldsymbol{r}, t)$ (up to a purely time-dependent $c(t)$) which reproduces the same time-dependent density. The initial state Ψ_0' in this system must be chosen such that it correctly*

yields the given density and its time derivative at the initial time.

These theorems establish the basis of TDDFT, leading to the derivation of the time-dependent Kohn-Sham equations, thus deriving a formal framework in which to compute time-dependent dynamics of a real system by solving an equivalent system of non-interacting electrons.

Sometimes, calculating the full response of the system to an external potential is not required or even desirable: when the system does not deviate much from the ground state, computing the full time-dependent wave function or density and extracting small deviations of the ground state from it is unefficient, and it is preferable to calculate these small differences directly. In this thesis, our scope will be the calculation of excitonic properties in the Linear Response TDDFT framework, which we will derive in the following section.

7.2 Linear Response TDDFT

For a periodic solid, the linear density response[1] to a perturbing potential v_1 can be written as

$$n_{1\mathbf{G}}(\mathbf{k},\omega) = \sum_{\mathbf{G}'} \chi_{\mathbf{G}\mathbf{G}'}(\mathbf{k},\omega) v_{1\mathbf{G}'}(\mathbf{k},\omega), \tag{7.1}$$

where the density response $n_{1\mathbf{G}}(\mathbf{k},\omega)$ is given in reciprocal space, and $\chi_{\mathbf{G}\mathbf{G}'}$ is the density-density response function of the system, which includes electron-electron interactions. In TDDFT, the response function is given by

$$\chi_{\mathbf{G}\mathbf{G}'}(\mathbf{k},\omega) = \chi^{KS}_{\mathbf{G}\mathbf{G}'}(\mathbf{k},\omega) + \sum_{\mathbf{G}_1,\mathbf{G}_2} \chi^{KS}_{\mathbf{G}\mathbf{G}_1}(\mathbf{k},\omega) f^{Hxc}_{\mathbf{G}_1\mathbf{G}_2}(\mathbf{k},\omega) \chi_{\mathbf{G}_2\mathbf{G}'}(\mathbf{k},\omega). \tag{7.2}$$

Here, we have introduced two key elements: the Kohn-Sham response function $\chi^{KS}_{\mathbf{G}\mathbf{G}'}$ and the Hartree-exchange-correlation (Hxc) kernel.

The Kohn-Sham response function can be built from the Kohn-Sham band structure:

$$\chi^{KS}_{\mathbf{G}\mathbf{G}'}(\mathbf{k},\omega) = \frac{2}{V} \sum_{\mathbf{k}'\in BZ} \sum_{j,l} \frac{f_{j\mathbf{k}'} - f_{l\mathbf{k}+\mathbf{k}'}}{\omega + \epsilon_{j\mathbf{k}'} - \epsilon_{l\mathbf{k}+\mathbf{k}'} + i\eta}$$
$$\times \int_{cell} d\mathbf{r} \phi^*_{j\mathbf{k}'}(\mathbf{r}) e^{-i(\mathbf{k}+\mathbf{G})\cdot\mathbf{r}} \phi^*_{l\mathbf{k}+\mathbf{k}'}(\mathbf{r}) \int_{cell} d\mathbf{r} \phi^*_{l\mathbf{k}+\mathbf{k}'}(\mathbf{r}') e^{i(\mathbf{k}+\mathbf{G}')\cdot\mathbf{r}'} \phi^*_{j\mathbf{k}'}(\mathbf{r}'), \tag{7.3}$$

where $\phi_{j\mathbf{k}}(\mathbf{r})$ are the Kohn-Sham single-particle Bloch wavefunctions, with j band index and $\epsilon_{j\mathbf{k}}$ energy. $f_{j\mathbf{k}}$ are the occupation numbers, equal to 1 (0) if the state $\phi_{j\mathbf{k}}$ is occupied (unoccupied). Eq. (7.3) can be simplified by using the bra-ket

[1] The time-dependent density is assumed to be expandable as $n(\mathbf{r},t) = n_0(\mathbf{r},t) + n_1(\mathbf{r},t) + ...$

notation:

$$\chi^{KS}_{\mathbf{G}\mathbf{G}'}(\mathbf{k},\omega) = \frac{2}{V}\sum_{\mathbf{k}'\in BZ}\sum_{j,l}\frac{f_{j\mathbf{k}'} - f_{l\mathbf{k}+\mathbf{k}'}}{\omega + \epsilon_{j\mathbf{k}'} - \epsilon_{l\mathbf{k}+\mathbf{k}'} + i\eta} \times \langle j\mathbf{k}'|\, e^{-i(\mathbf{k}+\mathbf{G})\cdot\mathbf{r}}\, |l\mathbf{k}+\mathbf{k}'\rangle \langle l\mathbf{k}+\mathbf{k}'|\, e^{i(\mathbf{k}+\mathbf{G}')\cdot\mathbf{r}'}\, |j\mathbf{k}'\rangle\,, \tag{7.4}$$

where the terms in the second row are meant to be integrated over the $\mathbf{r}$ and $\mathbf{r}'$ variables, respectively.

The Hartree-exchange-correlation kernel is given as

$$f^{Hxc}_{\mathbf{G}\mathbf{G}'}(\mathbf{k},\omega) = \frac{4\pi\delta_{\mathbf{G}\mathbf{G}'}}{|\mathbf{k}+\mathbf{G}|^2} + f^{xc}_{\mathbf{G}\mathbf{G}'}(\mathbf{k},\omega), \tag{7.5}$$

where the first term on the right-side is the Hartree kernel and the second term is the xc kernel. Similarly to DFT, in TDDFT, the exchange-correlation kernel does not have a known expression and has to be approximated. A more detailed discussion on the xc kernel and its effect on TDDFT calculations can be found in Section 2.2.3.

From equations (7.1) and (7.2), a self-consistent expression for the density response $n_{1\mathbf{G}}(\mathbf{k},\omega)$ is obtained.

$$n_{1\mathbf{G}}(\mathbf{k},\omega) = \sum_{\mathbf{G}'}\chi^{KS}_{\mathbf{G}\mathbf{G}'}(\mathbf{k},\omega)\left[v_{1\mathbf{G}'}(\mathbf{k},\omega) + \sum_{\mathbf{G}''} f^{Hxc}_{\mathbf{G}'\mathbf{G}''}(\mathbf{k},\omega) n_{1\mathbf{G}''}(\mathbf{k},\omega)\right]. \tag{7.6}$$

7.2.1 Dyson equation: optical absorption

The optical absorption spectrum of a material is obtained from the imaginary part of its macroscopic dielectric function $\epsilon_M(\omega)$, which is obtained from an averaging of the inverse microscopic dielectric function $\epsilon_{\mathbf{G}\mathbf{G}'}(\mathbf{k},\omega)$[2] as [118, 119]

$$\epsilon_M(\omega) = \lim_{k\to 0}\left[\epsilon^{-1}_{\mathbf{G}\mathbf{G}'}(\mathbf{k},\omega)|_{\mathbf{G}=\mathbf{G}'=0}\right]^{-1}. \tag{7.7}$$

In TDDFT, the microscopic dielectric function is given by

$$\epsilon_{\mathbf{G}\mathbf{G}'}(\mathbf{k},\omega) = \delta_{\mathbf{G}\mathbf{G}'} - v_{\mathbf{G}}(\mathbf{k})\tilde{\chi}_{\mathbf{G}\mathbf{G}'}(\mathbf{k},\omega), \tag{7.8}$$

where $v_{\mathbf{G}}(\mathbf{k}) = 4\pi/|\mathbf{k}+\mathbf{G}|^2$ is the Coulomb kernel, and $\tilde{\chi}$ is the proper response function, which is calculated from the Dyson equation (7.2) using $f^{xc}_{\mathbf{G}_1\mathbf{G}_2}$ instead of $f^{Hxc}_{\mathbf{G}_1\mathbf{G}_2}$. Plugging Eq. (7.8) into Eq. (7.7), one obtains the following expression for

[2] This is only true for crystals with cubic symmetry. In the general case, the expression is not that straightforward [117].

the macroscopic dielectric function:

$$\epsilon_M(\omega) = 1 - \lim_{k\to 0} v(\mathbf{k})\tilde{\chi}_{00}(\mathbf{k},\omega). \tag{7.9}$$

The response function, and therefore ϵ_M, can be calculated by directly solving the Dyson equation (7.2), which is a matrix equation of dimension $\mathbf{G}$, and links the microscopic ($\tilde{\chi}_{00}$) and macroscopic (ϵ_M) properties of the material under analysis. To do so, the Kohn-Sham response function $\chi^{KS}_{\mathbf{GG'}}$ has to be previously computed from Eq. (7.4), which implies summing over occupied and empty bands, and over the number of k-points in the Brillouin Zone.

This approach, which is sometimes called the *Dyson approach*, is the method of choice for calculating optical spectra, as it has a moderate computational cost. However, the method does not allow the precise determination of exciton binding energies, especially if the excitons are weakly bound. The reason is that, in practice, calculations are done with an artificial broadening of several tens of meV, in order to produce spectra that can be compared to experiment. This broadening will completely wash out any excitonic peaks that are on the order of a few tens of meV, which is the case for semiconductors [105].

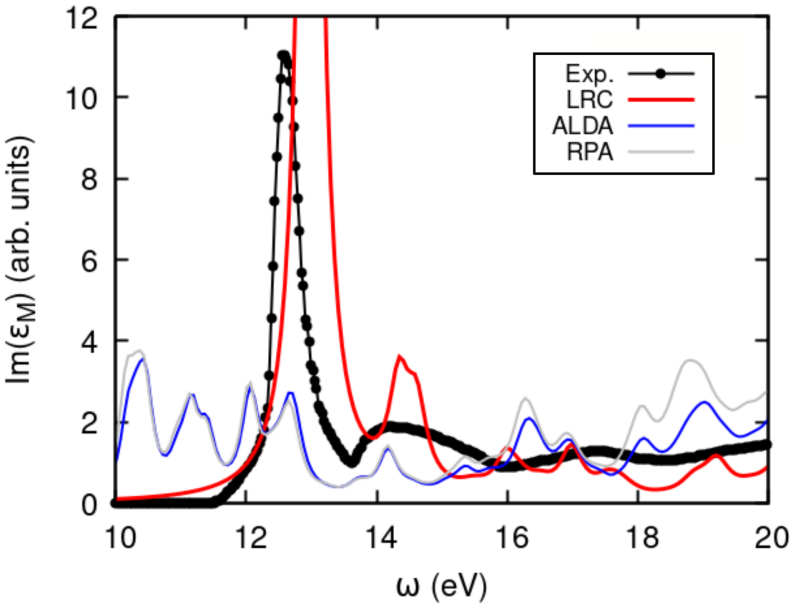

Figure 7.1: Absorption spectrum of lithium fluoride, calculated in different TDDFT approaches. In red, the absorption spectrum corresponding to the LRC is shown. In blue and grey, the adiabatic local density approximation (ALDA) and the random phase approximation (RPA) results, respectively. The black dots represent the experimental data. The optical spectra were computed using the *Yambo* package [120].

7.2.2 Casida equation: excitation energies

The calculation of excitation energies in the linear response TDDFT formalism is done via the Casida equation. If the external perturbation acting on the system is set to zero, only self-sustained solutions to the density reponse are considered. These eigenmodes oscillate with the excitation energies of the system [113]. Setting the external potential to zero, and after several lines of algebra, Eq. (7.6) can be rewritten in the following way [92, 113]:

$$\sum_{v'c'\mathbf{k}'} \{[(\epsilon_{c\mathbf{k}} - \epsilon_{v\mathbf{k}})\delta_{v'v}\delta_{c'c}\delta_{\mathbf{k}\mathbf{k}'} + K_{vc\mathbf{k},v'c'\mathbf{k}'}]X_{v'c'\mathbf{k}'} + K_{vc\mathbf{k},c'v'\mathbf{k}'}Y_{v'c'\mathbf{k}'}\} = -\omega X_{vc\mathbf{k}} \tag{7.10}$$

$$\sum_{v'c'\mathbf{k}'} \{K_{cv\mathbf{k}',v'c'\mathbf{k}'}X_{v'c'\mathbf{k}'} + [(\epsilon_{c\mathbf{k}} - \epsilon_{v\mathbf{k}})\delta_{v'v}\delta_{c'c}\delta_{\mathbf{k}\mathbf{k}'} + K_{cv\mathbf{k},c'v'\mathbf{k}'}]Y_{v'c'\mathbf{k}'}\} = -\omega Y_{vc\mathbf{k}}, \tag{7.11}$$

which has the form of an eigenvalue problem. The indices v, v' and c, c' represent the occupied (valence) and unoccupied (conduction) states, respectively. The energetic terms $\epsilon_{c\mathbf{k}} - \epsilon_{v\mathbf{k}}$ correspond to single-particle Kohn-Sham excitations, and $\mathbf{q} \to 0$ indicates that the terms are calculated in the optical limit; i.e. with no momentum transfer and only considering vertical transitions in momentum space ($\mathbf{k} = \mathbf{k}'$). The coupling between the single-particle orbitals is mediated by the matrices

$$\begin{aligned} K_{vc\mathbf{k},v'c'\mathbf{k}'}(\omega) = \lim_{\mathbf{q}\to 0} \frac{2}{V} \sum_{\mathbf{G}\mathbf{G}'} & \langle v\mathbf{k}| \, e^{i(\mathbf{q}+\mathbf{G})\cdot\mathbf{r}} \, |c\mathbf{k}\rangle \, \langle c'\mathbf{k}'| \, e^{-i(\mathbf{q}+\mathbf{G}')\cdot\mathbf{r}} \, |v'\mathbf{k}'\rangle \\ & \times \left(\frac{4\pi\delta_{\mathbf{G}\mathbf{G}'}}{|\mathbf{q}+\mathbf{G}|^2}(1 - \delta_{\mathbf{G},0}) + f^{xc}_{\mathbf{G}\mathbf{G}'}(\mathbf{q},\omega) \right). \end{aligned} \tag{7.12}$$

It should be noted that the $\mathbf{G} = 0$ term of the Hartree kernel (first term of the second row of Eq. (7.12)) is omitted. This is done so that the eigenvalues of the Casida equation correspond to the poles of the dielectric function. In principle, the xc kernel depends on the frecuency ω, but in practice, this dependence is often ignored by adopting the adiabatic approximation ($f^{xc}_{\mathbf{G}\mathbf{G}'}(\mathbf{q},\omega) \to f^{xc}_{\mathbf{G}\mathbf{G}'}(\mathbf{q})$).

The Casida equation (7.11) can be recast into its more compact matrix form

$$\begin{pmatrix} \mathbf{A} & \mathbf{B} \\ \mathbf{B}^* & \mathbf{A}^* \end{pmatrix} \begin{pmatrix} \mathbf{X}_n \\ \mathbf{Y}_n \end{pmatrix} = \omega \begin{pmatrix} -\mathbf{1} & \mathbf{0} \\ \mathbf{0} & \mathbf{1} \end{pmatrix} \begin{pmatrix} \mathbf{X}_n \\ \mathbf{Y}_n \end{pmatrix}, \tag{7.13}$$

where the excitation and de-excitation matrices $\mathbf{A}$ and $\mathbf{B}$ are defined as

$$A_{vc\mathbf{k},v'c'\mathbf{k}'}(\omega) = (\epsilon_{c\mathbf{k}} - \epsilon_{v\mathbf{k}})\delta_{v'v}\delta_{c'c}\delta_{\mathbf{k}\mathbf{k}'} + K_{vc\mathbf{k},v'c'\mathbf{k}'}(\omega) \tag{7.14}$$

$$B_{vc\mathbf{k},v'c'\mathbf{k}'}(\omega) = K_{vc\mathbf{k},v'c'\mathbf{k}'}(\omega). \tag{7.15}$$

Solving the Casida equation yields a spectrum of excitation energies ω that are the real excitation energies of the system. Even though the single-particle Kohn-Sham spectrum is used as an input, the energy levels that arise from the Casida equation differ from the KS excitation energies $(\epsilon_c - \epsilon_v)$ because of the coupling mediated by the K matrices. In this picture, excitons are manifested in the discrete energy levels that appear inside the Kohn-Sham gap. The exciton binding energy E_B is given by subtracting the energy of the lowest excited state and the Kohn-Sham band gap E_g(see Fig. (7.1)):

$$E_B = E_g - \omega_1. \tag{7.16}$$

Therefore, the Casida equation is a powerful tool that gives us a framework to directly compute the excitation energies of the system starting from the DFT single-particle wavefunctions of the ground state, provided that the f^{xc} kernel correctly includes the electron-hole interaction effects.

7.2.3 f_{xc} kernel and excitons

Although TDDFT is a formally exact theory, the mathematical form of exchange-correlation potential is unknown, which means that in practice approximations have to be done. In fact, both of the approaches that we have previously presented (Dyson and Casida) require an exchange-correlation kernel f_{xc}. Within the linear-response formalism, the frequency-dependent xc kernel of TDDFT is formally defined as [92, 121]

$$f_{xc}(\mathbf{r}, \mathbf{r}', \omega) = \int d(t - t') e^{i\omega(t-t')} \frac{\delta v_{xc}[n](\mathbf{r}, t)}{\delta n(\mathbf{r}', t')}\bigg|_{n_0(\mathbf{r})}, \tag{7.17}$$

where $v_{xc}[n](\boldsymbol{r}, t)$ is the xc potential of TDDFT and $n_0(\boldsymbol{r})$ is the ground-state density of the unperturbed system. In periodic systems, the f_{xc} kernel is transformed into the reciprocal space: $f_{\mathbf{G},\mathbf{G}'}(\mathbf{q}, \omega)$ (here, $\mathbf{G}$ and $\mathbf{G}$' are reciprocal lattice vectors and $\mathbf{q}$ is a wave vector within the Brillouin Zone).

Even though several formulations for f_{xc} kernels exist, one of the main issues one has to face when trying to calculate excitons using TDDFT is the long-range behaviour of the (xc) kernel. Local and semilocal xc kernels that work well in finite systems (such as the Adiabatic Local-Density Approximation, ALDA) do not yield bound excitons in solids, since they lack a long-range part [92, 104]. In this block of the thesis, we will focus on the so-called (static) long-range-corrected kernel, which is a simple (xc) kernel with a long-range part, which has been succesfully used to calculate excitonic properties in solids [92, 98, 99, 104, 105]:

$$f_{xc}^{\mathrm{LRC}} = \frac{-\alpha\, \delta_{\mathbf{G}\mathbf{G}'}}{|\mathbf{q} + \mathbf{G}|^2}. \tag{7.18}$$

The α parameter in the previous equation can be experimentally fitted, or calculated

from first-principles, using the dielectric function as an input [104, 105]. Further and more detailed discussion on the role of the LRC kernel when calculating excitons in the TDDFT framework can be found in Chapter 3 of this block.

7.3 Excitation energies beyond TDDFT

Similarly to TDDFT, the Bethe-Salpeter Equation (BSE) of many-body perturbation theory can be written as an eigenvalue problem that follows Eq. (7.13). In fact, if the Tamm-Dancoff approximation (TDA) is adopted (i.e. $\mathbf{B}$=0 so that excitations and de-excitations are decoupled) [105, 111, 113], the following eigenvalue problem has to be solved in both approaches:

$$[(\epsilon_{c\mathbf{k}} - \epsilon_{v\mathbf{k}'})\delta_{vv'}\delta_{cc'}\delta_{\mathbf{k}\mathbf{k}'} + K^{\mathrm{Hxc}}_{cv\mathbf{k},c'v'\mathbf{k}'}]\mathbf{Y}_n = \omega_n \mathbf{Y}_n. \tag{7.19}$$

Essentially, the matrix in Eq. (7.19) consists of a diagonal of KS excitation energies, which are coupled by K^{Hxc}.

The main difference between the TDDFT and BSE approaches lies in the mathematical description of the coupling matrix $K^{Hxc} = K^H + K^{xc}$. The Hartree kernel K^H is the same in both approaches:

$$K^{\mathrm{H}}_{cv\mathbf{k},c'v'\mathbf{k}'} = \frac{2}{V}\sum_{\mathbf{G}\neq 0}\frac{4\pi}{|\mathbf{G}|^2}\langle c\mathbf{k}|\, e^{i\mathbf{G}\cdot\mathbf{r}}\,|v\mathbf{k}\rangle\left\langle v'\mathbf{k}'\right|\, e^{-i\mathbf{G}\cdot\mathbf{r}}\left|c'\mathbf{k}'\right\rangle, \tag{7.20}$$

where V is the crystal volume and the long-range of the Coulomb term $4\pi/|\mathbf{G}|^2$ is omitted.

The exchange-correlation K^{xc} term of the coupling matrix differs for the TDDFT and BSE approaches. In TDDFT, within the optical limit where the momentum transfer in negligible ($\mathbf{q}\to 0$) the matrix elements are given by

$$\begin{aligned} K^{xc}_{cv\mathbf{k},c'v'\mathbf{k}'} = \frac{2}{V}\sum_{\mathbf{G},\mathbf{G}'} & f_{xc,\mathbf{G}\mathbf{G}'}(\mathbf{q}\to 0) \\ & \times \langle c\mathbf{k}|\, e^{i(\mathbf{q}+\mathbf{G})\cdot\mathbf{r}}\,|v\mathbf{k}\rangle\left\langle v'\mathbf{k}'\right|\, e^{-i(\mathbf{q}+\mathbf{G}')\cdot\mathbf{r}}\left|c'\mathbf{k}'\right\rangle, \end{aligned} \tag{7.21}$$

where f_{xc} is the exchange-correlation kernel. In the BSE formalism, it has the form

$$\begin{aligned} K^{\mathrm{xc}}_{cv\mathbf{k},c'v'\mathbf{k}'} = -\frac{1}{V}\sum_{\mathbf{G},\mathbf{G}'} & W_{\mathbf{G},\mathbf{G}'}(\mathbf{q},\omega)\delta_{\mathbf{q},\mathbf{k}-\mathbf{k}'} \\ & \times \langle c\mathbf{k}|\, e^{i(\mathbf{q}+\mathbf{G})\cdot\mathbf{r}}\left|c'\mathbf{k}'\right\rangle\left\langle v'\mathbf{k}'\right|\, e^{-i(\mathbf{q}+\mathbf{G}')\cdot\mathbf{r}}\,|v\mathbf{k}\rangle. \end{aligned} \tag{7.22}$$

$W_{\mathbf{G},\mathbf{G}'}$ is the screened Coulomb interaction.

There are some fundamental differences between the BSE and the Casida equation approach. On the one hand, in TDDFT the xc matrix elements involve braket operations between valence and conduction bands, while in MBPT, these elements are given by c-c' and v-v' integrals[3]. On the other hand, the Coulomb interaction is described by the exchange-correlation kernel f_{xc} in DFT, and by the screened Coulomb interaction W in the BSE. The numerical advantage of TDDFT appears in this term. One of the main numerical bottlenecks of the MBPT approach is the construction of the screened Coulomb interaction [110, 111], which depends on the dielectric screening $\epsilon^{-1}_{\mathbf{G}\mathbf{G}'}$ as

$$W_{\mathbf{G},\mathbf{G}'}(\mathbf{q},\omega) = -\frac{4\pi\epsilon^{-1}_{\mathbf{G}\mathbf{G}'}(\mathbf{q},\omega)}{|\mathbf{q}+\mathbf{G}|\left|\mathbf{q}+\mathbf{G}'\right|}. \tag{7.23}$$

Even in the static approach with $\omega = 0$, the calculation of the dielectric function requires a sum over all $\mathbf{q} = \mathbf{k} - \mathbf{k}'$ values in the BZ, as well as a double sum over the reciprocal lattice vectors $\mathbf{G}$ and $\mathbf{G}'$. In TDDFT, the f_{xc} kernel is usually approximated by simpler kernels (such as the LRC kernel), which reduces the computational cost considerably.

[3] This will have implications when we analyze the role of the Coulomb singularity in the following section.

CHAPTER 8

DIRECT CALCULATION OF EXCITON BINDING ENERGIES FROM FIRST-PRINCIPLES

Over the last years, Time Dependent Density Functional Theory has established itself as a computationally cheaper, yet effective alternative to the Many Body Perturbation Theory to calculate the optical properties of solids. Within the Linear Response formalism, it is possible to obtain the optical absorption spectra in good agreement with experiments, as well as the direct determination of the exciton binding energies. However, the family of exchange-correlation kernels known as long-range corrected (LRC) kernels that correctly capture excitonic features are not capable of simultaneously produce good looking spectra and accurate exciton binding energies. More recently, this discrepancy has been partially overcomed by means of an hybrid-TDDFT approach. In this chapter, we show that the key resides in the numerical treatment of the long-range Coulomb singular term. We carefuly study the effect of this term, both in the pure-TDDFT and hybrid approach using a Wigner-Seitz truncated kernel. We find that computing this term presents technical difficulties that are hard to overcome in both approaches, and that points to the need for a better description of the electron-hole interaction.

8.1 TDDFT approach: LRC kernel

Since TDDFT is a formally rigorous theory, the solution of eq. (7.21) should provide us with the exact values of the excitonic energies, as long as we are able to satisfactorily approximate the unknown exchange-correlation function. The family of exchange-correlation kernels known as long-range corrected (LRC) kernels

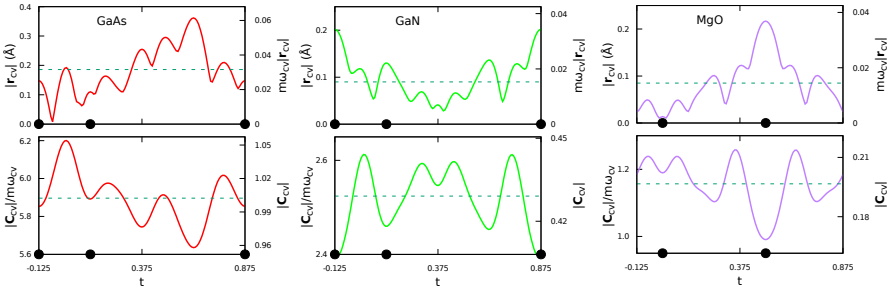

Figure 8.1: Magnitude of the r-matrix (top) and C-matrix (bottom) elements in bulk GaAs, z-GaN and MgO. The magnitudes in the left axes are given in Å, while the ones in the right axes are in units of the momentum matrix element p_{cv}. The horizontal axis represents the cell center on the [111] line of the conventional unit cell, so that the positions of the cell center are given by $t(a, a, a)$. The black dots in this axes indicate the positions of the atoms, and the horizontal dashed lines represent the mean values of the plotted magnitudes.

have proven to correctly capture excitonic features by reproducing experimental absorption spectra in semiconductors [92, 99, 100, 105, 122]. Even when we employ its simplest static form of

$$f_{xc}^{\mathrm{LRC}} = \frac{-\alpha\,\delta_{\mathbf{G}\mathbf{G}'}}{|\mathbf{q}+\mathbf{G}|^2} \tag{8.1}$$

the agreement with experimental absorption spectra is remarkable. However, the empirical parameter α determined from the static dielectric constant of the crystal ($\alpha = 4.615\varepsilon_\infty^{-1} - 0.213$) fails to reproduce bound excitons, unless α is set ad-hoc to a much higher value (see Fig [1] in [105]). In the same reference, the authors propose as a possible solution to the discrepancy, a material dependent non-uniform scaling factor for Bootstrap-type kernels that correctly reproduces both, the peak height and the position. The price to be paid, is the necessity of an extra arbitrary function that contains four parameters that need to be fitted and has no a priory theoretical justification. In the following, we will try to justify that the nature of the discrepancy is of numerical origin. In other other words, we will show that the way in which the $\mathbf{q} \to 0$ and $\mathbf{G} = 0$ limit is handled, completely determines the values of the exciton binding energies, and hence, the value of any empirical parameter α or function needed for the kernels.

In the optical limit and for $\mathbf{G} = 0$, the matrix elements of Eq. (7.21) have a 0/0 indeterminate form for f_{xc}^{LRC} type kernels, as the ground state KS valence and conduction states are orthogonal to each other. The usual way to handle this indetermination is to perform a series expansion of the numerator [104, 105]:

$$\langle c\mathbf{k}|\, e^{i\mathbf{q}\cdot\mathbf{r}}\, |v\mathbf{k}\rangle \simeq \mathbf{q}\,\langle c\mathbf{k}|\,\mathbf{r}\,|v\mathbf{k}\rangle\,. \tag{8.2}$$

which automatically entails a mutual cancellation of the vanishing $\mathbf{q}$ vectors in the

numerator and denominator, yielding a finite term. Nevertheless, a new problem arises as the interband transition value of the position operator has to be calculated, an ill-defined quantity (origin dependent) in infinite crystals with periodic boundary conditions.

In practice, this issue is alleviated throughout the literature [108, 123] by using the commutator relation $\hat{\mathbf{p}} = i[H_{\mathrm{SCF}}, \hat{\mathbf{r}}]$ that transforms the expected value of the position operator into a well defined expectation value of the momentum operator. This is commonly known as the *p-r* relation:

$$\langle c\mathbf{k}|\,\mathbf{r}\,|v\mathbf{k}\rangle = \frac{\langle c\mathbf{k}|\,[H_{\mathrm{SCF}}, \hat{\mathbf{r}}]\,|v\mathbf{k}\rangle}{(\epsilon_{c\mathbf{k}} - \epsilon_{v\mathbf{k}})} = \frac{\langle c\mathbf{k}|\,\mathbf{p} - i[\hat{\mathbf{r}}, V_{\mathrm{nl}}]\,|v\mathbf{k}\rangle}{(\epsilon_{c\mathbf{k}} - \epsilon_{v\mathbf{k}})} \tag{8.3}$$

However, to derive Eq. (8.3), is necessary to employ the above mentioned commutator relation which holds at each point in $\mathbf{r}$ space and to invoke the Hermiticity of the hamiltonian by $\langle c\mathbf{k}|\,H_{\mathrm{SCF}} = \langle c\mathbf{k}|\,\epsilon_{c\mathbf{k}}$. In more algebraic detail, an integration by parts is carried out in the matrix element $\langle c\mathbf{k}|\,H_{\mathrm{SCF}}\mathbf{r}\,|v\mathbf{k}\rangle$ and a surface integral term ($\mathbf{C}_{c\mathbf{k},v\mathbf{k}}$) arises that should only be neglected for finite systems where the wave-function decays to zero far enough at the surface boundary. In contrast, for infinite solids with periodic boundary conditions [109]:

$$\langle c\mathbf{k}|\,\hat{\mathbf{p}}\,|v\mathbf{k}\rangle = i(\epsilon_{c\mathbf{k}} - \epsilon_{v\mathbf{k}})\,\langle c\mathbf{k}|\,\mathbf{r}\,|v\mathbf{k}\rangle + \mathbf{C}_{c\mathbf{k},v\mathbf{k}} \tag{8.4}$$

with the additional surface term

$$\mathbf{C}_{c\mathbf{k}',v\mathbf{k}} = \frac{1}{2}\int_{s(v)} d\mathbf{S}\cdot[\varphi^*_{c\mathbf{k}'}(\mathbf{r})\hat{\mathbf{p}}\varphi_{v\mathbf{k}}(\mathbf{r}) + (\hat{\mathbf{p}}\varphi_{c\mathbf{k}'}(\mathbf{r}))^*\varphi_{v\mathbf{k}}(\mathbf{r})]\mathbf{r} \tag{8.5}$$

Namely, the correct *p-r* relation contains a surface term that compensates for the ambiguity related to the position matrix element that depends on the choice of the unit cell. As the momentum matrix element does not have such an ambiguity, it is clear that there must be an additional term. We will address the importance of this surface term, by extending the same quantification performed in [109] for GaAs, to the GaN semiconductor and MgO insulator (see the reference for calculation parameters). We will later see the effect it produces in the binding energies of the excitons.

To do so, we calculated the $\mathbf{r}$ and $\mathbf{C}$ matrix elements for bulk GaAs, z-GaN and MgO using a simple Cohen-Bergstresser pseudopotential approach[1] [124]. In Fig. (8.1), the interband position matrix element $\langle c\mathbf{k}|\,\mathbf{r}\,|v\mathbf{k}\rangle$ and the correction term $\mathbf{C}_{c\mathbf{k},v\mathbf{k}}$ are shown. Both magnitudes depend on the location of the cell over which the integrals are taken. We also observe that the magnitude of the $\mathbf{r}$ matrix element is much smaller than that of the correction term. In the case of GaAs, the mean value of the correction term is around 31.7 times bigger, while in β-GaN and MgO this value is of 28.04 and 13.6, respectively. These results clearly

[1] Details about this approach and the numerical values employed are shown in Appendix F

show that in periodic systems, the contribution of the correction term is far from trivial. Therefore, neglecting it yields to the overestimation of the $\langle c\mathbf{k}|\,\mathbf{r}\,|v\mathbf{k}\rangle$ matrix elements, which, in turn, leads to the need of smaller α parameters to reproduce experimental binding energies. This unit-cell dependence of the results points to the need of going beyond pure-TDDFT to consistently calculate exciton binding energies in solids.

The next step is to determine the contribution of the $\mathbf{q}$=0, $\mathbf{G}$=0 Coulomb singular term, in the calculation of exciton binding energies. For this, we have built our own code that evaluates the matrix elements of Eq. [7.21] and solves the eigenvalue problem of Eq.[7.13] within the TDA approximation. We use as input for the ground-state, Kohn-Sham wave-functions and energies obtained with the QUANTUM ESPRESSO code [125]. Experimental lattice parameters and norm-conserving LDA pseudopotentials without any scissors or GW corrections were used to compare to reference values [104, 105]. A $20 \times 20 \times 20$ Γ-centered $\mathbf{k}$-point mesh, 3 valence bands and 5 conduction bands were used for GaAs. These parameters for the rest of the materials are: $16 \times 16 \times 16$, 3, 6 for β-GaN and MgO; $16 \times 16 \times 8$, 6, 9 α-GaN and AlN; and $8 \times 8 \times 8$, 3, 24 for LiF, Ar and Ne.

The only difference between the calculation presented in reference [105] and this paper, lies precisely in the numerical treatment of the $\mathbf{q} = \mathbf{G} = 0$ term. Instead of using the p-r relation trick of Eq[8.3], we have directly computed the matrix elements for a finite, but very small $\mathbf{q}$ grid, as implemented in reference [126]. Fig. 8.2 shows the resulting α values that yield the experimental binding energies of an array of semiconductors and insulators in the following three cases: (a) Setting $f_{xc}(\mathbf{G} = \mathbf{0}) = 0$ in Eq.[7.21], i.e., neglecting the indetermination; (b) only considering the $f_{xc}(\mathbf{G} = \mathbf{0})$ term different from zero and neglecting the all the other terms of the summatory (LRC Head-only); and c) full solution (LRC Diagonal). Moreover, for comparison purposes, fig 8.2 includes values for α obtained using the *p-r relation* taken from reference [105].

The first thing to note is that the resulting α values for the (a) case in in which the indeterminate head-term is ignored, yields values that lay between 15 and 30 (green dots in Fig. (8.2)), and no noticeable trend with respect to the material type (semiconductor/insulator) is noticed. These values can be two orders of magnitude larger for small gap semiconductors and of the same order for large gap insulators when compared to those in ref [105]. Thus, it necessarily implies that the $K_{xc}(\mathbf{G} = \mathbf{0})$ contribution is crucial and completely fixes the final values of α. In addition, when the Head terms are added, either isolated (magenta diamonds) or including the complete summation in Eq. 7.21 (blue triangles), the α values needed to reproduce experimental binding energies decrease significantly but still differ from the red squares of the above mentioned reference. Lastly, it is worth mentioning that in our opinion, the parabolic trend shown by red squares as the bandgap of the materials increase is somehow a contrived consequence due to the use of the *p-r relation* in which the surface term is ignored. Note that in Eq (8.3)

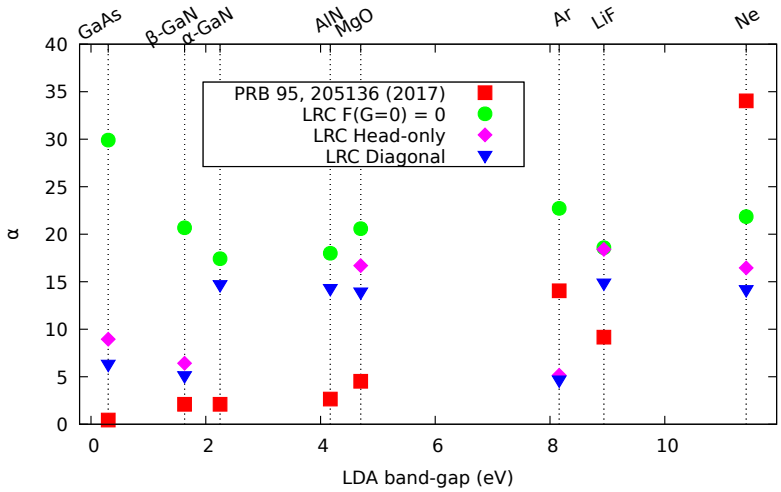

Figure 8.2: Fitted LRC kernel α-parameters that reproduce the experimental exciton binding energy. In red, values from reference [105]. Values obtained omitting the singular term are given in green, while the diagonal and head-only kernel are given in blue and magenta, respectively.

the bandgap energy divides each momentum matrix element, (and assuming that the numerator is bounded), higher values of α are required as we move towards insulating materials.

8.2 Hybrid TDDFT

One of the biggest computational bottlenecks of solving the Bethe-Salpeter Equation is building the screened Coulomb interaction matrix $W_{\mathbf{G},\mathbf{G}'}$ in equation (7.22) [92, 110]. In the Screened Exact Exchange (SXX) approach, this term is given by

$$W_{\mathbf{G},\mathbf{G}'}(\mathbf{q}) = -4\pi\gamma \frac{\delta_{\mathbf{G}\mathbf{G}'}}{|\mathbf{q}+\mathbf{G}|^2}, \tag{8.6}$$

where only the diagonal terms of the exact exchange are considered, and the dielectric screening γ is usually introduced as a parameter. A usual parametrization for this term is given by $\gamma = \epsilon^{-1}$, where ϵ is the experimental or *ab initio* calculated static dielectric function [110, 111]. This approach has been shown to give comparable results to the full BSE [92, 110, 111], while considerably lowering the computation time.

8.2.1 Wigner-Seitz truncation of the kernel

In the SXX approach, a correct treatment for the Coulomb term is crucial. However, in comparison with TDDFT, the $\mathbf{q} = \mathbf{G} = 0$ term for the $c = c'$ and $v = v'$ matrix

elements now diverges as $1/0^2$. Real-space truncation methods to numerically handle the Coulomb interaction have been previously studied to calculate the exact exchange energy in solids [127–129]. They found that the real space truncation of the Coulomb term on a supercell with Wigner-Seitz that naturally includes the crystal symmetry, is the best choice in terms of fast convergence of the k-point sampling. In this approach, the coulomb kernel is given as follows:

$$W_{\mathbf{G}}^{\mathrm{WS}} = \frac{4\pi}{G^2}\left(1 - e^{\frac{-G^2}{4\alpha^2}}\right) + \frac{\Omega}{N_{\mathbf{r}}}\sum_{r\in\mathrm{WS}} e^{-i\mathbf{q}\cdot\mathbf{r}}\frac{erf(\alpha r)}{r}, \tag{8.7}$$

which has a finite, ved value at $\mathbf{G}$=0:

$$W_{\mathbf{G}=0}^{\mathrm{WS}} = \frac{\pi}{\alpha^2} + \frac{\Omega}{N_{\mathbf{r}}}\sum_{r\in\mathrm{WS}} \frac{erf(\alpha r)}{r}. \tag{8.8}$$

Here, where erf is the error function, and α is the range-separation parameter. In Fig. (8.3), we compute the Fourier transform to bring the kernel in Eq. (8.7) to the real space, which allows us to see the great agreement between the Wigner-Seitz truncated and the $1/r$ Coulomb potentials.

We have implemented this particular truncation method for the calculation of the matrix elements in Eq (8.6) and studied its performance for a testing set of semiconductors and insulators. We calculate the exciton binding energy with respect to the following convergence parameters: k-point sampling of the Brillouin Zone and dielectric screening parameter γ. We find that other convergence parameters, such as the number of valence and conduction bands, have a negligible impact on the calculated exciton binding energies. In other words, for all the compounds under analysis, a single valence and conduction band were enough to yield converged results.

The convergence of the exciton binding energy with respect to the Brillouin Zone sampling and dielectric screening parameter γ is shown in panels (a) and (b) of Fig. (8.4), respectively. We find that the exciton binding energy decays as $N_k^{-1/3}$, where N_k is both the number of k-points in the Brillouin Zone and the number of unit cells in the WS supercell of the crystal in the real space. This slow convergence requires large k-point meshes, and the numerical results are highly dependent on N_k. For all the compounds under analysis, the binding energy is linearly proportional to the dielectric screening γ. To keep all the calculation ab-initio, our γ values were computed using the RPA dielectric constant. Using the experimental dielectric constant changed the binding energies less than 10% in the wide gap insulators, and up to 30% for GaAs and CdS. We therefore conclude that, even if the dielectric screening γ is an important parameter to precisely determine the exciton binding energy, N_k is the crucial variable.

In table (8.1), exciton binding energy values obtained in the WS-SXX

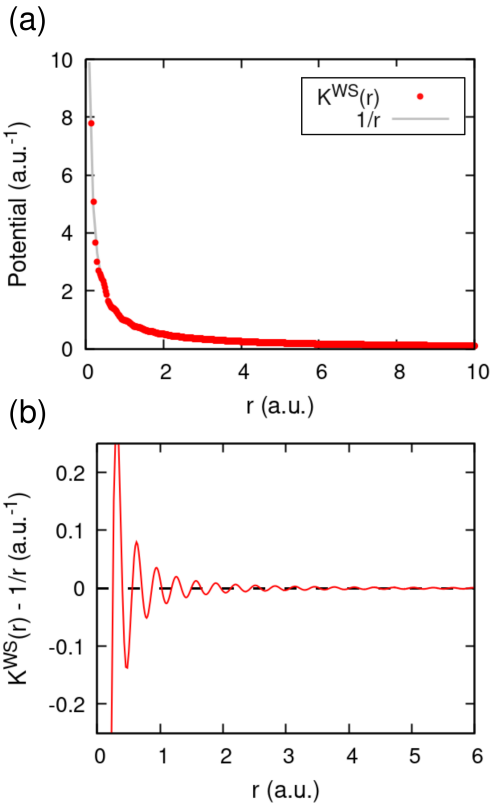

Figure 8.3: (a) Comparison between the coulomb kernel $1/r$ (grey line) and the real space Wigner-Seitz truncated kernel (red dots). (b) Difference between the WS truncated and Coulomb kernel.

Approach	GaAs	CdS	z-GaN	w-GaN	AlN	MgO	LiF	Ar
BSE [111]	24	59	103	110	181	-	2050	1830
SXX [111]	24	58	101	106	177	-	1930	1750
WS-SXX	25	58	92	95	124	180	588	387
Exp.	4	28	26	20	75	80	1600	1900

Table 8.1: Exciton binding energies obtained with the different hybrid approaches. The experimental data was extracted from Refs. [130–140].

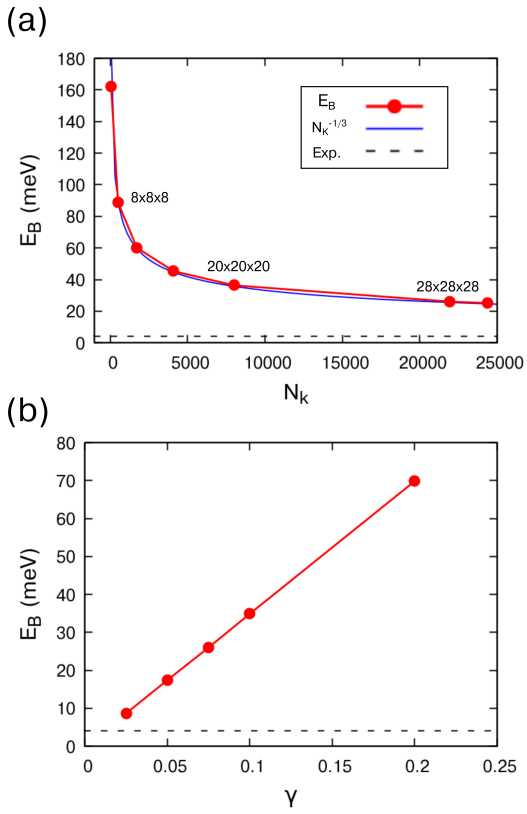

Figure 8.4: Calculated exciton binding energies of GaAs with respect to the Brillouin Zone sampling N_k (panel (a)) and the dielectric screening parameter γ (panel (b)). (a) For the k-point sampling, the exciton binding energy is proportional to $N_k^{-1/3}$, a trend that has already been observed in the literature. (b) For the dielectric screening, the binding energies vary linearly with γ.

approximation are displayed along reference and experimental values. To compare our results with the literature, we set the parameters to match those in the reference [111], with the exception of the number of conduction and valence bands, which in our case were fixed to $n_c = n_v = 1$. We find that for most of the semiconductors, the exciton binding energies are in good agreement with the theoretical results reported in the reference. Specifically, the Wigner-Seitz truncated kernel performs better for Wurtzite type materials, i.e. w-GaN and AlN, because the numerical truncation of the $1/r$ potential takes into account the hexagonal lattice symmetry. However, in the case of the insulators, we observe a clear underestimation of the binding energies with the WS-SXX kernel. We attribute the underestimation to the fact that the WS-SXX kernel mostly takes the long-range interaction into account, without proper consideration of the local effects. In the wide gap insulators with localized excitons, these effects are not negligible, and this discrepancy might merit further investigation with fully hybrid kernels beyond the scope of this paper. Another explanation to the calculated values is that for all the compounds we observe identical trends with respect to the convergence parameters, with no qualitative variations with the electronic character. This results in exciton binding energies that are mostly governed by the chosen k-grid and γ parameters. The sharp dependence on the k-grid is specially worrying, since fully converged results could vary greatly with the numerical values that are obtained from the grids that can be currently handled. All in all, we find that the sharp dependence on the singular term presents an important numerical bottleneck for the calculation of precise exciton binding energies in solids, which limits the real applicability of the simple kernels that are currently used.

8.3 Conclusions

In this chapter of the thesis, we studied the effect of the long-range Coulomb term in the calculation of the exciton binding energies. We focused our analysis in two different frameworks: LRC-TDDFT, and hybrid calculations with the SXX kernel. We find that in the pure TDDFT calculations, the effect of the correction term C_{cv} is crucial, and that neglecting it could lead to errors. In the hybrid TDDFT-BSE framework, we propose a new WS truncated SXX kernel, which yields results close to the BSE for semiconductors, while falling short for the wide-band insulators. We once again find that the effect of the long-range Coulomb interaction is the leading contribution to the calculated exciton binding energies, concluding that a correct and careful description of this term is essential in this kind of calculation. We believe that the findings of this work encourage further and more detailed analysis of the Coulomb singularity that governs the excitonic effects in solids.

CONCLUSIONS AND OUTLOOK

In this thesis, we studied diverse quantum phenomena occurring in semiconducting materials. In the framework of the Density Functional Theory and its time-dependent generalization, we carried out a number of different investigations that study the magnetism and optical excitations in these compounds. The main findings and conclusions obtained in this thesis are summarized below:

- In Chapter 3, we performed a fundamental theoretical analysis of the magnetism of bulk ilmenite cobalt titanate. We obtained the ground state G-AFM configuration, and computed the exchange couplings between the cobalt ions. To get a qualitatively accurate description of the $3d$ electrons, we employed the GGA+U formalism, and checked the effect of the Hubbard correction parameters in the material. We derived a magnetic phase-diagram with respect to the temperature that reveals that $CoTiO_3$ has two critical temperatures, linked to the breaking of the inter-layer AFM coupling (Néel temperature) and the beginning of paramagnetism, respectively. We then studied the effect of the spin-orbit coupling in this compound, and found that, in apparent contradiction with the experiments, crystalline cobalt titanate shows an out-of-plane anisotropy. We analyzed the effect of doping in the material, and found that n-doping, in the form of cobalt-titanium anti-site disorder, can turn the anisotropy in-plane.

- In Chapter 4, we went from the bulk ilmenite cobalt titanate to the two-dimensional ilmenene–like compounds. We characterized the whole family of $TMTiO_3$ ilmenenes, deriving their optimized crystal structures, electronic structures and magnetic ground-state. We found all the compounds to be magnetic semiconductors, with an antiferromagnetic-by-layers spin configuration. By adding the spin-orbit coupling, we then determined the magnetocrystalline anisotropy of each compound, and found the following general trend: ilmenenes have an out-of-plane (in-plane) magnetocrystalline anisotropy below (above) half-filling of the $3d$ shell. In particular, with a large out-of-plane MAE, chromium titanate $CrTiO_3$ appears to be a candidate to find applications in spintronics.

- In Chapter 5, we analyzed the layered semiconductor $CaMn_2Bi_2$. Similar to the previous investigations, we carried out a systematic analysis of the

fundamental magnetic properties of the compound, and we extended the analysis to study the effect of strain on the magnetism. We found that $CaMn_2Bi_2$ is an antiferromagnetic semiconductor with the spin aligned in the zigzag-x direction of the hexagonal plane. Applying a strain of about 0.25% in the x-axis, the easy spin orientation of the crystal changes to the armchair-y direction.

- In Chapter 7, we focus on the calculation of exciton binding energies of semiconductors and insulators. We developed a code that calculates exciton binding energies from input ground-state wavefunctions, and tested different numerical approaches. In the TDDFT framework, we studied the importance of the singular $\mathbf{G}$=0 term of the Casida equation, and found that in periodic solids this term is often computed without including a correction term C_{cv}. We found that the magnitude of this singular term completely determines the obtained excitation energies, and that a more consistent approach is needed to compute excitation energies via TDDFT in a meaningful way. In the hybrid framework, we implemented a new kernel, based on the Wigner-Seitz truncation of the SXX kernel, and obtained exciton binding energies in good agreement with the reference [111]. However, we found a worrying dependence of the results with respect to the convergence parameters, mainly the number of k-points, which limits the predictive capabilities of the implemented approach.

We hope that this thesis has contributed to giving a better understanding of the physical phenomena that have been studied throughout it. On the one hand, we believe that we have set a solid ground for future research on the magnetic properties of layered ilmenite and ilmenene–like compounds, which pans the way to perform more advanced calculations, such as investigating the spin-spirals and magnons. On the other hand, even if we were not successful on implementing a code that precisely calculates exciton binding energies in a computationally efficient way, we sincerely believe that our findings in this respect help to point out some problems in the field. Our research points to the need of correctly addressing and converging the Coulomb interaction in the coupling matrices, and to develop kernels that describe the electron-hole interaction in a more precise way.

Looking forward, the results obtained in this thesis already open new questions that could be addressed. Regarding ilmenite cobalt titanate, apart from spin-spiral calculations, studying the magnetic properties under strain could lead to interesting results that we have not studied in this thesis. In the ilmenene–like oxides, the effect of doping has not been studied, and could have interesting applications by allowing to turn the anisotropy of the in-plane ilmenene layers out-of-plane. The study of exciton binding energies within TDDFT and beyond was not very hope-giving, but there is still work to do in this regard. Testing better kernels, maybe based on qualitative models for excitons could lead to improved and more stable results.

Appendices

Appendix A

$CoTiO_3$: All-electron test for the band structure

In order to check the validity of the chosen number of valence electrons to be included per element, we compare the VASP calculation with a more precise all-electron calculation performed with the Elk code[141]. We find that both band structures are in great qualitative agreement, which confirms the validity of the chosen number of valence electrons per element in our calculations.

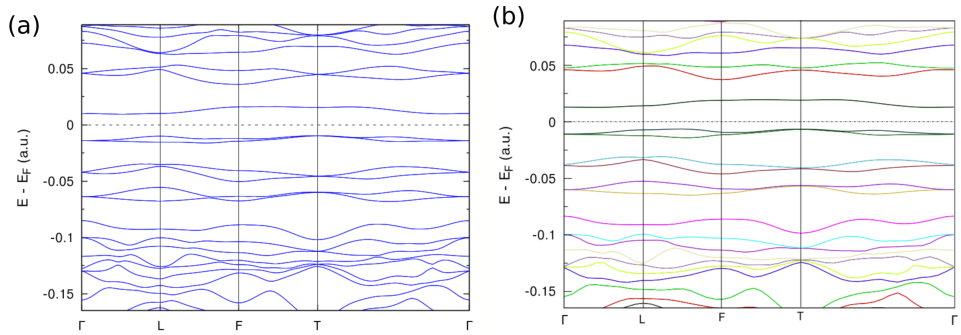

Figure A.1: F-AFM band structure in the chemical primitive cell, in the GGA (panel (a)) and all-electron (panel (b)) approaches.

Appendix B

$CoTiO_3$: Convergence of the MAE

The MAE is a small magnitude, in our case in the order of 10^{-4} eV/unit cell. To ensure that our results are numerically correct, we calculate the MAE amplitude with respect to the Brillouin Zone sampling n_k (Fig. B.1). We show that the MAE has a fast convergence in this system, and that the 8x8x8 Monkhorst-Pack grid used in our calculations gives well-converged anisotropy energies.

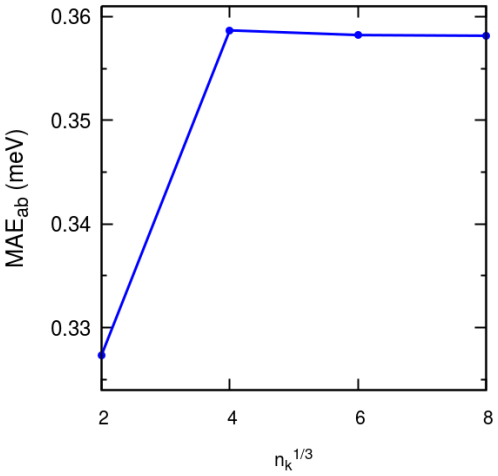

Figure B.1: MAE of the hexagonal *ab* plane against the Brillouin Zone sampling per unit cell. Regular Γ-point centered $n_k \times n_k \times n_k$ Monkhorst-Pack grids were used.

We also calculated the MAE for the hexagonal cell of bulk cobalt titanate. This cell contains three times the atoms of the primitive magnetic cell, and a k-point mesh of 8x8x2 was used. The MAE per cobalt atom was of 0.0895 meV, a value

in great agreement with that of the rhombohedral primitive cell. We find that the change to FM configuration does not affect the MAE in VASP, which yields a 0.0864 meV/Co atom out-of-plane anisotropy.

We checked the MAE in value and sign with respect to all-electron calculations using the Elk code. Calculations of the MAE performed with the Elk code show the same out-of-plane tendency obtained with VASP for the ferromagnetic configuration. To save computational time, we use the VASP relaxed structure for the FM primitive cell. Muffin tin radii for the spheres are 2.01, 2.34, and 1.47 au for Ti, Co and O, respectively. Using well converged energy values with an angular momentum cutoff of 19 for the muffin tin density and potential and the APW functions, and within 10^{-6} and 10^{-5} for the energy and potential, we obtain a MAE of 0.3 meV per cobalt atom in Elk. This calculated value is even larger than that obtained with VASP (0.09 meV/Co atom), and the resulting anisotropy remains being out-of-plane. We consider that at this stage, the Elk results are just reinforcing the trends calculated using VASP, the difference in the values is related to the considered ...

Appendix C

$CoTiO_3$: Effect of U in the MAE

As commented in the main text, we find that the MAE values obtained in the GGA approach are larger than those using GGA+U, as shown in Fig. C.1 in a systematic way with the angle θ. The structural expansion induced by the U parameter plays a leading role in this trend, as the GGA structure is considerably closer to the experimental cell. The GGA+U anisotropy with the experimental lattice parameters is larger ($MAE_{ab}/N_{Co} \simeq 0.145$ meV), a fact that points to the structural expansion as the main responsible for the decreasing MAE.

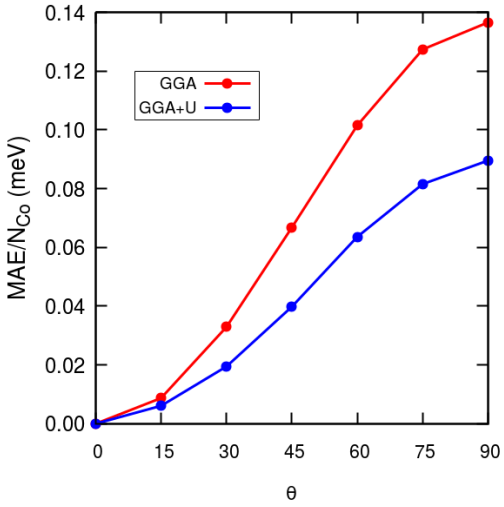

Figure C.1: Comparison between the MAE in the GGA and GGA+U approaches. The MAE values are given per cobalt atom.

Appendix D

$CoTiO_3$: Orbital moment and non-collinearity

We show the calculated orbital magnetic moment values μ_L in the GGA+U approach, as well as the angular difference $\Delta\theta$ between the spin and orbital magnetic moments that arises when the spin-orbit coupling is included. Note the overall non-collinearity between spin and orbital moments unless the θ values are just $\theta = 0, \pi/2$ and π.

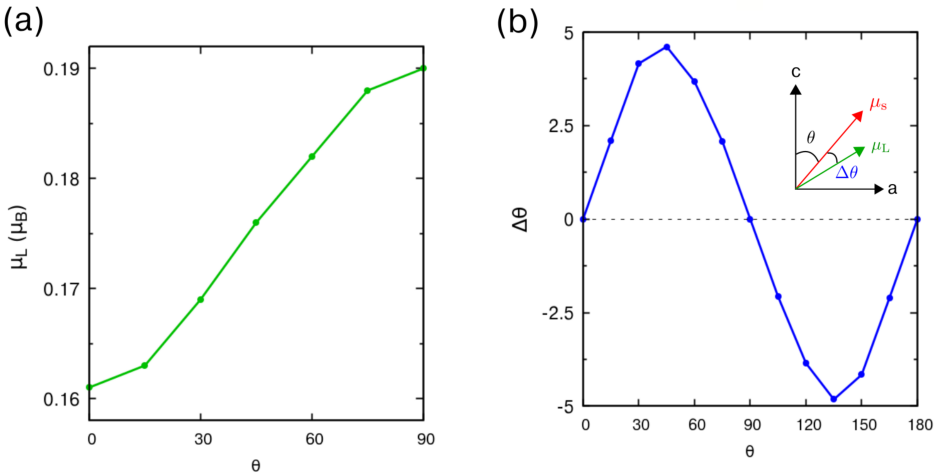

Figure D.1: (a) Orbital moment μ_L of cobalt titanate calculated in the GGA+U approximation. (b) Angular difference $\Delta\theta$ between the spin and orbital magnetic moments.

Appendix E

TM Ilmenenes: PDOS and band structures

We collect the projected densities of states on an atom of each chemical species in Figures E.1-E.3. More interestingly, Figures E.4-E.6 show the band structures projected on the electronic orbitals with the transition metal atom ranging from V to Zn. We divide the analysis of ilmenes into three categories: below half filling (V, Cr and Mn), above half filing (Fe, Co and Ni), and just below full filling (brass metals, Zu and Zn).

(i) In the case of the below half filling ilmenenes (Fig. E.4), the d_{xz}, d_{yz} and d_{z^2} orbitals with an out-of-plane component are the first to be occupied, while the in-plane ones are the least stable. For the chromium ilmenene, the d_{xz} and d_{yz} orbitals are splitted: the d_{xy} and $d_{x^2-y^2}$ orbitals are highly splitted, with the $d_{x^2-y^2}$ orbital being occupied, and the dxy orbital unoccupied. This splitting is the source of Jahn-Teller like distortions for Cr ilmenenes.

(ii) Ilemenenes above half filling (Fig. E.5) have the down-spin part of the orbitals coming into play. For iron ilmenene, the first orbital to fill is d_{z^2}, while in the case of cobalt, due to degenerate orbitals, the system prefers to fill the d_{xz} and d_{yz} orbitals first. For nickel titanate, the d_{z^2} orbital is again filled first, while the others are partially filled. This kind of alternance gives rise to odd-even trends when the levels are being occupied in going from Fe to Ni oxide ilmenenes.

(iii) Finally, in Fig. E.6, copper ilmenene shows a similar behavior to the chromium ilmenene: the d_{xz} and d_{yz} orbitals split, as do the d_{xy} and $d_{x^2-y^2}$ orbitals, with the d_{xy} orbital being the unoccupied one. The zinc titanate ilmenene with a d^{10} electronic configuration has all orbitals occupied, and is spin compensated.

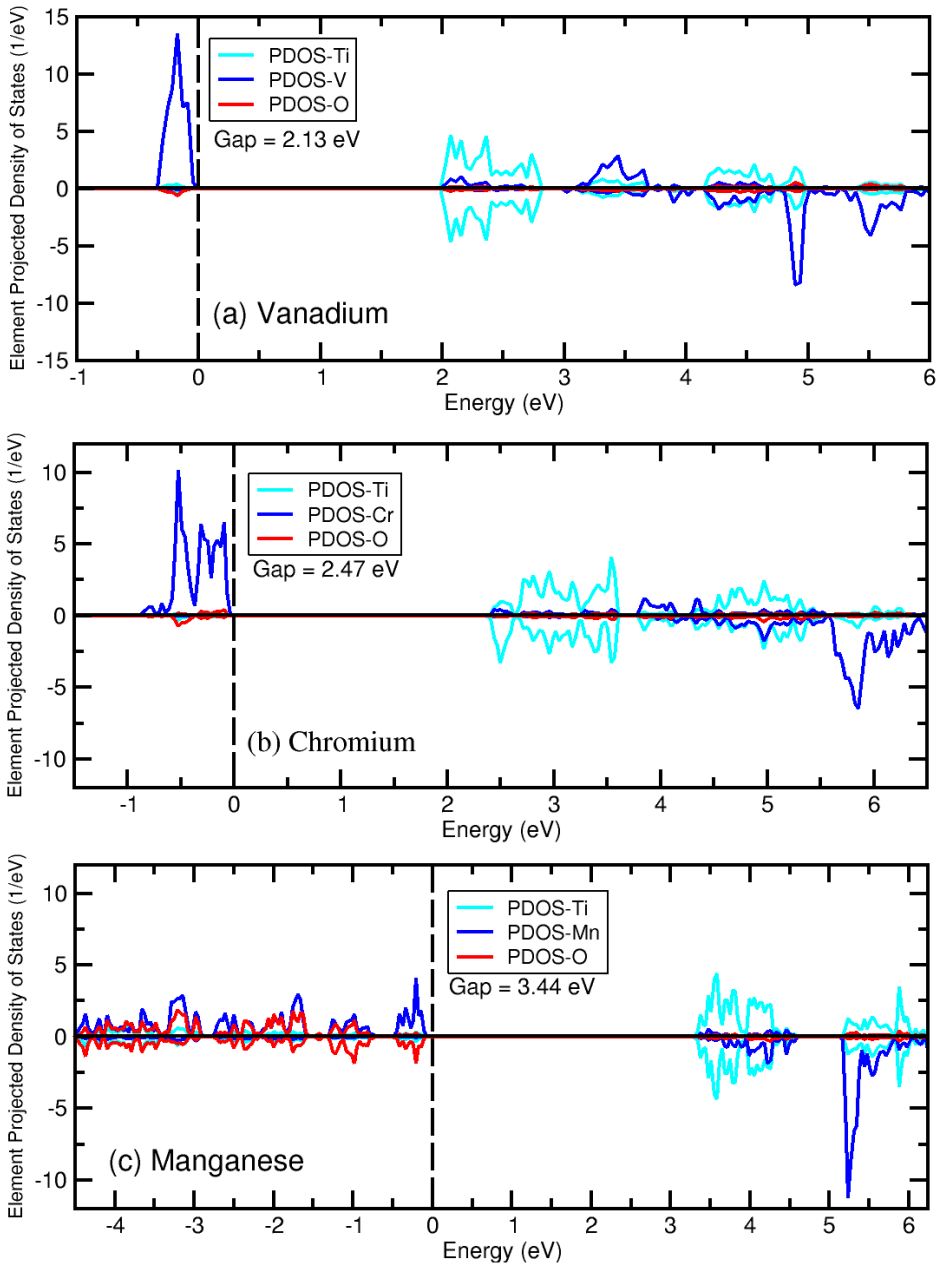

Figure E.1: Element-projected density of states (DOS) on a atom of each atomic species. Transition metal is denoted in blue, titanium in cyan, and oxygen in red.

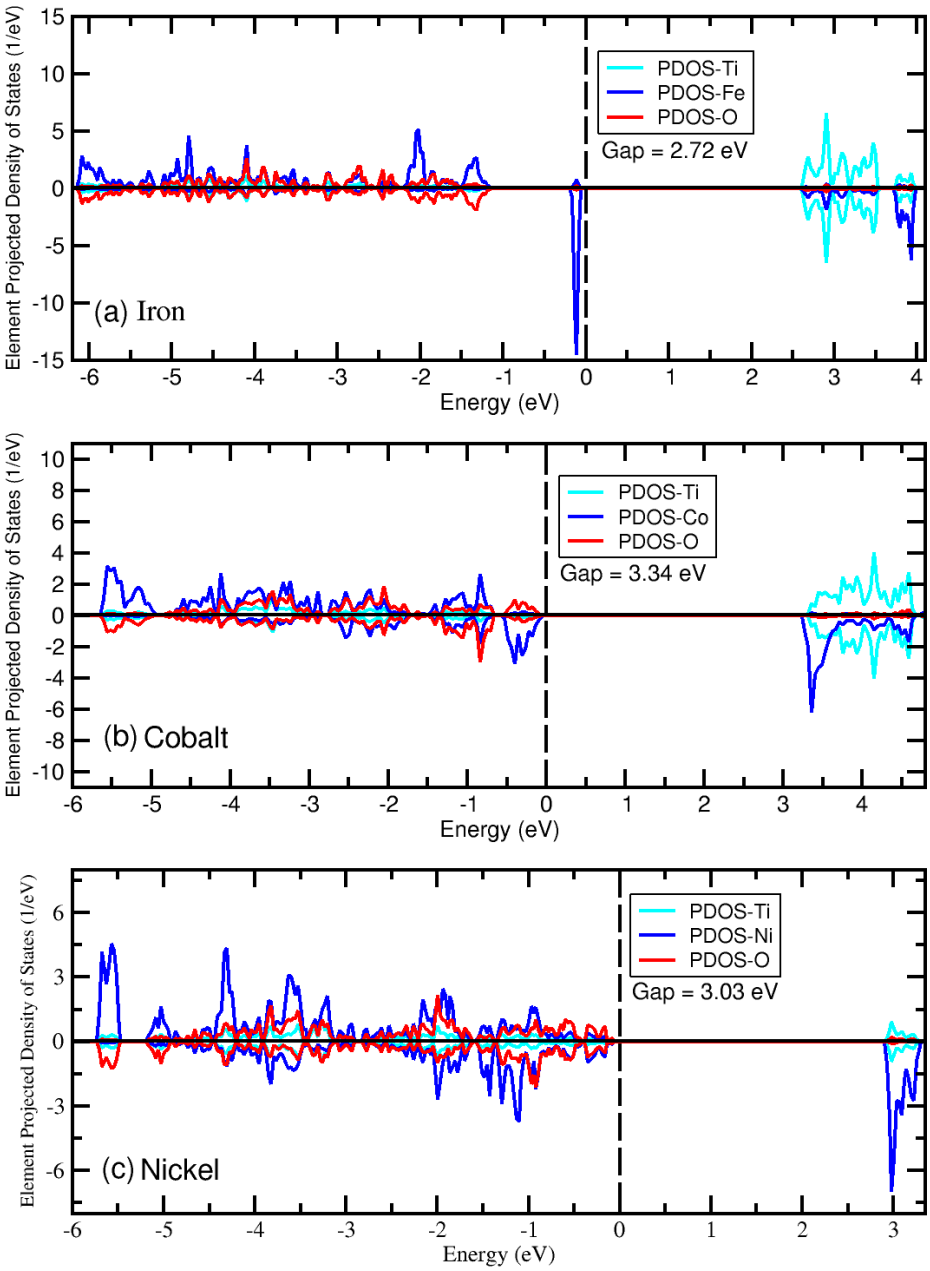

Figure E.2: Element-projected density of states (DOS) on a atom of each atomic species. Colors follow the caption of previous figure.

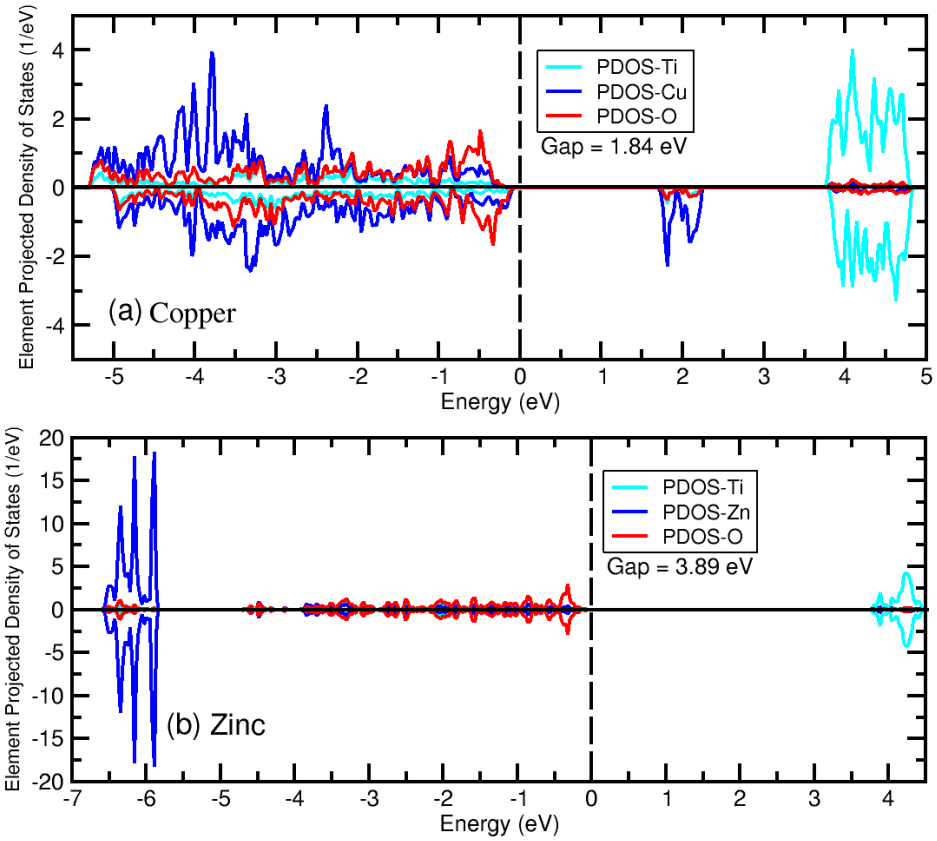

Figure E.3: Element-projected density of states (DOS) on a atom of each atomic species. Colors follow the caption of figures above.

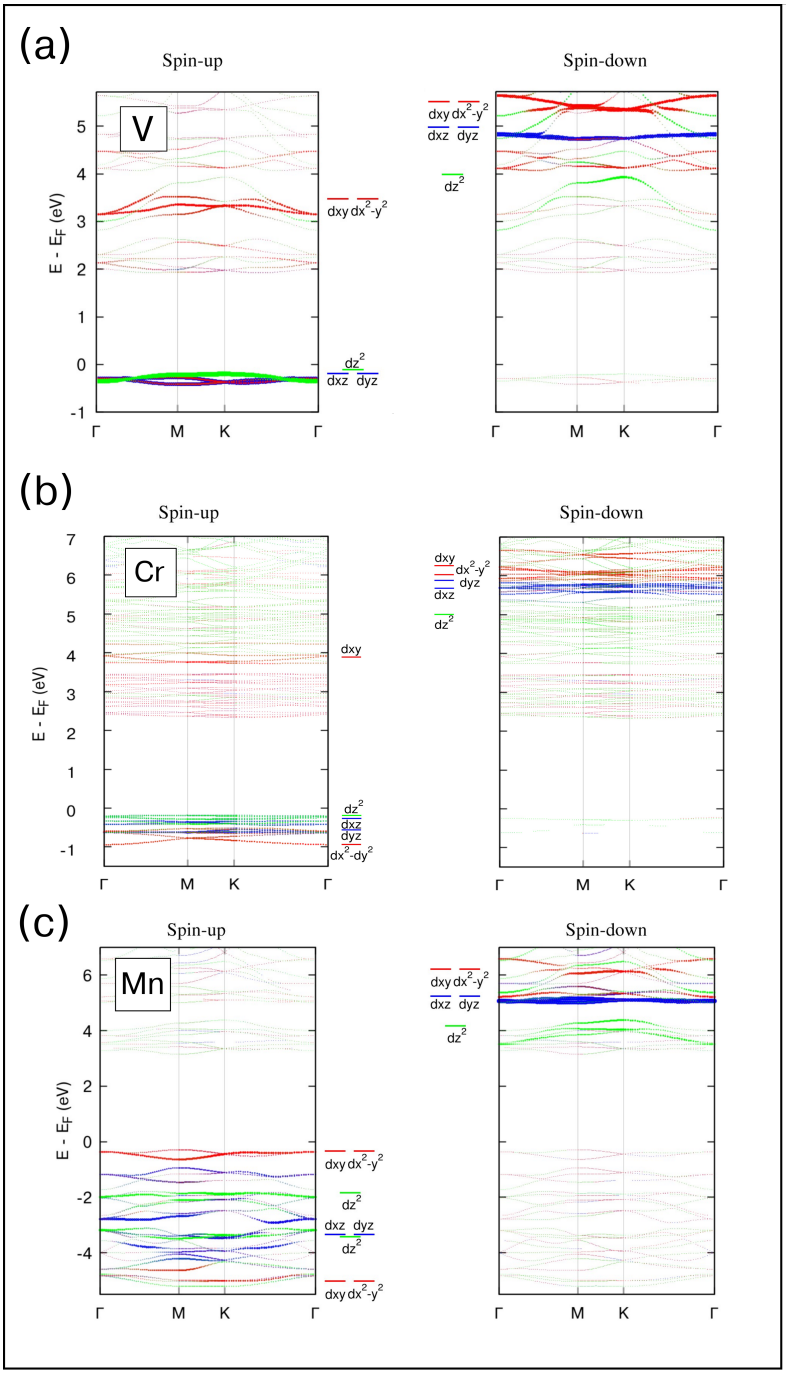

Figure E.4: Electronic band structure and PDOS for the ilmenenes below half-filling. Vanadium titanate, chromium titanate and manganese titanate are displayed in panels (a), (b) and (c), respectively.

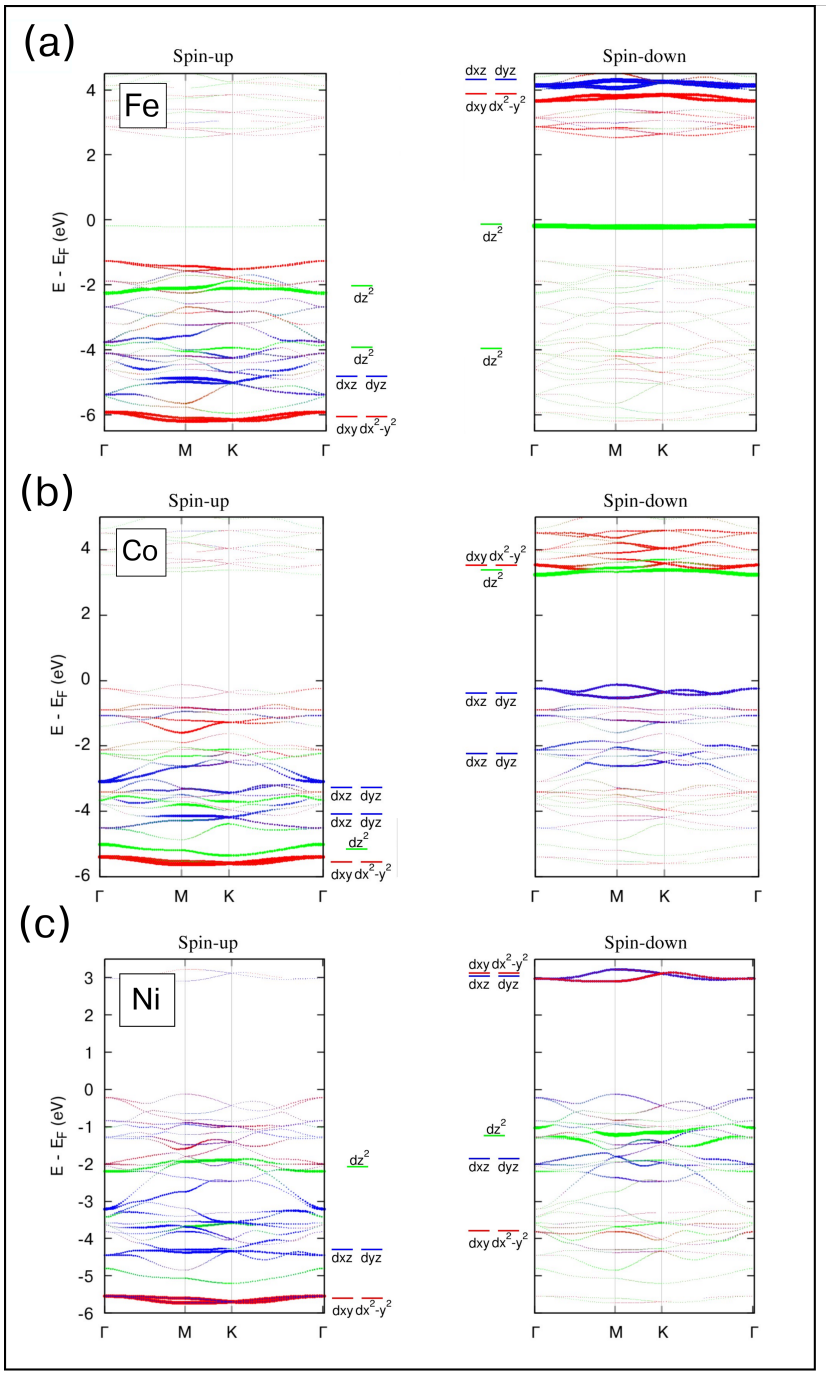

Figure E.5: Electronic band structure and PDOS for the ilmenenes above half-filling. Iron titanate, cobalt titanate and nickel titanate are displayed in panels (a), (b) and (c), respectively.

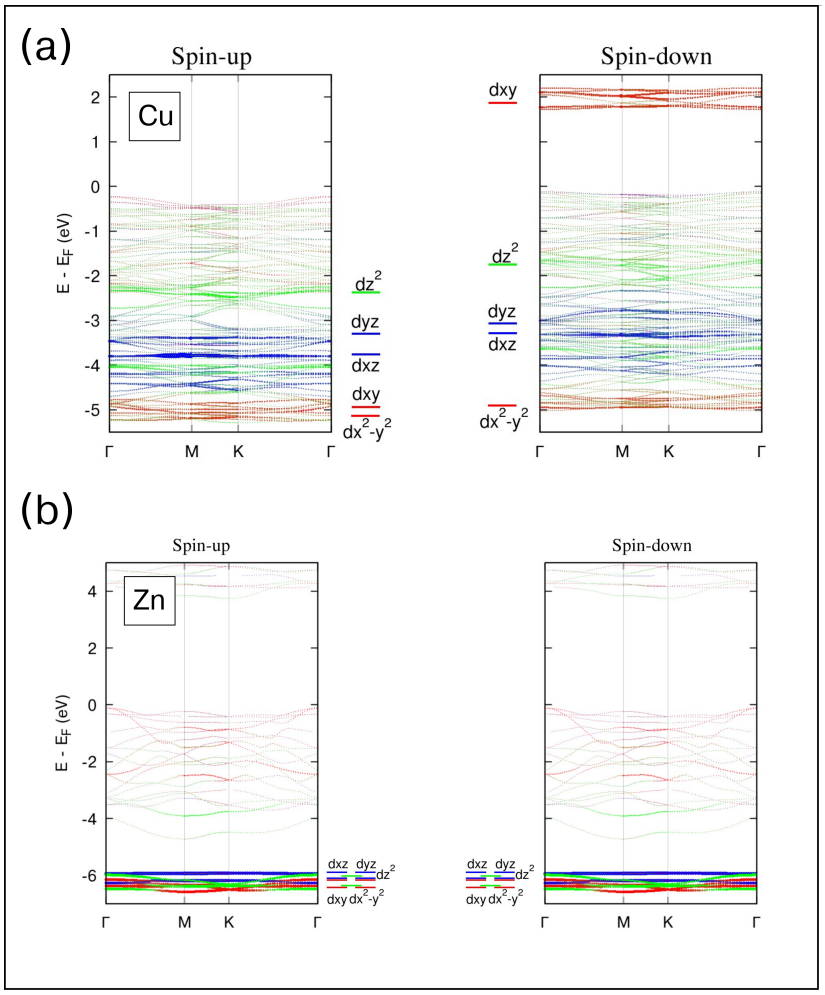

Figure E.6: Electronic band structure and PDOS of the brass metal ilmenenes copper titanate (panel (a)) and zinc titanate (panel (b)).

Appendix F

EXCITONS: Computation of the Correction Terms C_{cv}

In Chapter 8, we compute the correction terms C_{cv} of Eq. (8.5) for the semiconductors GaAs, GaN and MgO. To do so, instead of directly calculating the surface intergrals, from Eq. (8.4) we calculate the correction terms as the difference of the position- and momentum-operator cell integrals:

$$\mathbf{C}_{c\mathbf{k},v\mathbf{k}} = \langle c\mathbf{k}| \hat{\mathbf{p}} |v\mathbf{k}\rangle - i(\epsilon_{c\mathbf{k}} - \epsilon_{v\mathbf{k}}) \langle c\mathbf{k}| \mathbf{r} |v\mathbf{k}\rangle . \tag{F.1}$$

To compute the cell integrals, we calculate the Bloch wavefunctions φ using the Cohen-Bergstresser approach as in reference [109].

The Cohen-Bergstresser approach [124] is a pseudopotential approach that consists on solving the following Schrödinger equation

$$\epsilon_{v\mathbf{k}} c_{v,\mathbf{G}_i} = \sum_{i \neq j} V_p(\mathbf{G}_i - \mathbf{G}_j) c_{v,\mathbf{G}_j} + (\mathbf{k} + \mathbf{G}_i)^2 c_{v,\mathbf{G}_i}, \tag{F.2}$$

where $\epsilon_{v\mathbf{k}}$ are the eigenvalues, and the coefficients $c_{v,\mathbf{G}_i}(\mathbf{k})$ can be used to build the Bloch wavefunctions φ in Eq. (8.5):

$$\varphi_{v\mathbf{k}}(\mathbf{r}) = \sum_{\mathbf{G}} c_{v,\mathbf{G}}(\mathbf{k}) e^{i(\mathbf{k}+\mathbf{G})\mathbf{r}}. \tag{F.3}$$

The terms V_p in Eq. (F.2) are the Fourier components of the pseudopotential, which are decomposed into symmetric and antisymmetric parts by

$$\begin{aligned} V_p(\mathbf{G}_i - \mathbf{G}_j) = {} & V_s(|\mathbf{G}_i - \mathbf{G}_j| a/2\pi) \cos[(\mathbf{G}_i - \mathbf{G}_j)\mathbf{s}] \\ & - iV_a(|\mathbf{G}_i - \mathbf{G}_j| a/2\pi) \sin[(\mathbf{G}_i - \mathbf{G}_j)\mathbf{s}]. \end{aligned} \tag{F.4}$$

V_s and V_a are the symmetric and antisymmetric form factors, respectively. Provided

	$V_S(\sqrt{2})$	$V_S(\sqrt{3})$	$V_S(\sqrt{8})$	$V_S(\sqrt{11})$	$V_S(\sqrt{12})$	$V_A(\sqrt{3})$	$V_A(2)$	$V_A(\sqrt{11})$
GaAs	0	-0.23	0.01	0.06	0	0.07	0.05	0.01
GaN	0	0.226	0.001	0.157	0	0.305	0.219	0.060
MgO	-0.0956	0	0.0705	0	0.0191	0.2471	0	0.0136

Table F.1: Symmetric and antisymmetric form factors of the pseudopotential in Eq. (F.4), given in Rydbergs.

that these numbers are known, this pseudopotential approach can yield accurate results for the valence and conduction bands of semiconductors [109]. The vector $\mathbf{s}$ represents the position of an atom of the compound inside a Wigner-Seitz cell with the origin in the middle of the two basis atoms. In the case of GaAs, with the cell origin in the middle of both atoms, the position of the Ga atom is $\mathbf{s} = a/8(1,1,1)$.

In Table F.1, we collected the form factors we employed for GaAs [124], GaN [142, 143] and MgO [144]. The reciprocal lattice of all three compounds is a *bcc* structure, with $\mathbf{G} = m_1\mathbf{b}_1 + m_2\mathbf{b}_2 + m_3\mathbf{b}_3$, and $\mathbf{b}_1 = (2\pi/a)(-1,1,1)$, $\mathbf{b}_2 = (2\pi/a)(1,-1,1)$, and $\mathbf{b}_3 = (2\pi/a)(1,1,-1)$. For all the compounds under analysis, we only considered form factors for $|\mathbf{G}_i - \mathbf{G}_j| \leq 2\pi/a\sqrt{12}$.

List of publications

Most of the results discussed in this thesis are based on the following publications:

1. **M. Arruabarrena**, A. Leonardo, M. Rodriguez-Vega, G.A Fiete, A. Ayuela: "Out-of-plane magnetic anisotropy in bulk ilmenite $CoTiO_3$," Physical Review B **105**, 144425 (2022).
https://doi.org/10.1103/PhysRevB.105.144425

2. R.H Aguilera-del-Toro, **M. Arruabarrena**, A. Leonardo, A. Ayuela: "Magnetism in Two-Dimensional Ilmenenes: Intrinsic Order and Strong Anisotropy," arXiv:2211.01732 (2022)
https://doi.org/10.48550/arXiv.2211.01732

3. **M. Arruabarrena**, A. Leonardo, A. Ayuela: "Wigner-Seitz truncated TDDFT approach for the calculation of exciton binding energies in solids," arXiv:2303.13389 (2023)
https://doi.org/10.48550/arXiv.2303.13389

4. B.T. Fichera, B. Lv., K. Morey, Z. Shen, C. Lee, E. Donoway, A. Liebman-Peláez, A. Kogar, T. Kurumaji, M. Rodriguez-Vega, R.H. Aguilera-del-Toro, **M. Arruabarrena**, B. Ilyas, T. Luo, G. Zhang, J. Xu, F. Hao, A. Leonardo, A. Ayuela, J.G. Checkelsky, G.A. Fiete, J. Orenstein, N. Gedik: "Light-induced reorientation transition in an antiferromagnetic semiconductor," (In preparation).

Bibliography

[1] M. Arruabarrena, A. Leonardo, M. Rodriguez-Vega, G. A. Fiete, and A. Ayuela, "Out-of-plane magnetic anisotropy in bulk ilmenite $CoTiO_3$," *Phys. Rev. B*, vol. 105, p. 144425, Apr 2022.

[2] R. H. Aguilera-del Toro, M. Arruabarrena, A. Leonardo, and A. Ayuela, "Magnetism in two-dimensional ilmenenes: Intrinsic order and strong anisotropy," 2022.

[3] M. Arruabarrena, A. Leonardo, and A. Ayuela, "Wigner-seitz truncated tddft approach for the calculation of exciton binding energies in solids," 2023.

[4] W. Gerlach and O. Stern, "Das magnetische moment des silberatoms," *Zeitschrift für Physik*.

[5] W. Pauli, "Über den zusammenhang des abschlusses der elektronengruppen im atom mit der komplexstruktur der spektren," *Zeitschrift für Physik*, vol. 31, pp. 765–783, Feb 1925.

[6] G. E. Uhlenbeck and S. Goudsmit, "Ersetzung der hypothese vom unmechanischen zwang durch eine forderung bezüglich des inneren verhaltens jedes einzelnen elektrons," *Die Naturwissenschaften*, vol. 13, pp. 953–954, Nov 1925.

[7] "The quantum theory of the electron," *Proceedings of the Royal Society of London. Series A, Containing Papers of a Mathematical and Physical Character*, vol. 117, pp. 610–624, Feb. 1928.

[8] T. Moriya, "Ferro- and Antiferromagnetism of Transition Metals and Alloys," *Progress of Theoretical Physics*, vol. 33, pp. 157–183, 02 1965.

[9] J. J. Rhyne, *Bulk Magnetic Properties*, pp. 129–185. Boston, MA: Springer US, 1972.

[10] W. Heisenberg, "Zur theorie des ferromagnetismus," *Zeitschrift für Physik*, vol. 49, pp. 619–636, Sep 1928.

[11] Néel, M. Louis, "Propriétés magnétiques des ferrites ; ferrimagnétisme et antiferromagnétisme," *Ann. Phys.*, vol. 12, no. 3, pp. 137–198, 1948.

[12] J. Stöhr and H. Siegmann, *Magnetism: From Fundamentals to Nanoscale Dynamics*. Springer Series in Solid-State Sciences, Springer, 2006.

[13] P. Hohenberg and W. Kohn, "Inhomogeneous electron gas," *Phys. Rev.*, vol. 136, pp. B864–B871, Nov 1964.

[14] W. Kohn and L. J. Sham, "Self-consistent equations including exchange and correlation effects," *Phys. Rev.*, vol. 140, pp. A1133–A1138, Nov 1965.

[15] G. Bihlmayer, *Density Functional Theory for Magnetism and Magnetic Anisotropy*, pp. 895–917. Cham: Springer International Publishing, 2020.

[16] N. F. Mott, "The Basis of the Electron Theory of Metals, with Special Reference to the Transition Metals," *Proceedings of the Physical Society. Section A*, vol. 62, p. 416, jul 1949.

[17] A. M. Oleś, "Correlation effects in the cohesion and magnetic properties of transition metals," *Phys. Rev. B*, vol. 23, pp. 271–278, Jan 1981.

[18] A. M. Oles and G. Stollhoff, "Correlation effects in ferromagnetism of transition metals," *Phys. Rev. B*, vol. 29, pp. 314–327, Jan 1984.

[19] S. A. Tolba, K. M. Gameel, B. A. Ali, H. A. Almossalami, and N. K. Allam, "The DFT+U: Approaches, Accuracy, and Applications," in *Density Functional Calculations* (G. Yang, ed.), ch. 1, Rijeka: IntechOpen, 2018.

[20] R. J. D. Tilley, *Perovskites: Structure-Property Relationships*. John Wiley & Sons, 2016.

[21] R. Dubrovin, N. Siverin, M. Prosnikov, V. Chernyshev, N. Novikova, P. Christianen, A. Balbashov, and R. Pisarev, "Lattice dynamics and spontaneous magnetodielectric effect in ilmenite $CoTiO_3$," *J. Alloys Compd.*, p. 157633, 2020.

[22] Tien-Sheng Chao, Wei-Ming Ku, Hong-Chin Lin, D. Landheer, Yu-Yang Wang, and Y. Mori, "$CoTiO_3$ high-κ dielectrics on HSG for DRAM applications," *IEEE Trans. Electron Devices*, vol. 51, no. 12, pp. 2200–2204, 2004.

[23] J. H. Hwang, E. N. Son, R. Lee, S. H. Kim, J. I. Baek, H. J. Ryu, K. T. Lee, and J. M. Sohn, "A thermogravimetric study of $CoTiO_3$ as oxygen carrier for chemical looping combustion," *Catalysis Today*, vol. 303, pp. 13 – 18, 2018.

[24] M. Elliot, P. A. McClarty, D. Prabhakaran, R. D. Johnson, H. C. Walker, P. Manuel, and R. Coldea, "Order-by-disorder from bond-dependent exchange and intensity signature of nodal quasiparticles in a honeycomb cobaltate," *Nat. Commun.*, vol. 12, p. 3936, Jun 2021.

[25] B. Yuan, I. Khait, G.-J. Shu, F. C. Chou, M. B. Stone, J. P. Clancy, A. Paramekanti, and Y.-J. Kim, "Dirac Magnons in a Honeycomb Lattice Quantum XY Magnet $CoTiO_3$," *Phys. Rev. X*, vol. 10, p. 011062, Mar 2020.

[26] A. Puthirath Balan, S. Radhakrishnan, R. Kumar, R. Neupane, S. K. Sinha, L. Deng, C. A. de los Reyes, A. Apte, B. M. Rao, M. Paulose, R. Vajtai, C. W. Chu, G. Costin, A. A. Martí, O. K. Varghese, A. K. Singh, C. S. Tiwary, M. R. Anantharaman, and P. M. Ajayan, "A Non-van der Waals Two-Dimensional Material from Natural Titanium Mineral Ore Ilmenite," *Chemistry of Materials*, vol. 30, no. 17, pp. 5923–5931, 2018.

[27] M. Born and R. Oppenheimer, "Zur quantentheorie der molekeln," *Annalen der Physik*, vol. 389, no. 20, pp. 457–484, 1927.

[28] V. Fock, "Näherungsmethode zur lösung des quantenmechanischen mehrkörperproblems," *Zeitschrift für Physik*, vol. 61, pp. 126–148, Jan 1930.

[29] J. C. Slater, "The theory of complex spectra," *Phys. Rev.*, vol. 34, pp. 1293–1322, Nov 1929.

[30] C. Noguera, "Chapter 2 - clean oxide surfaces: a theoretical review," in *Oxide Surfaces* (D. Woodruff, ed.), vol. 9 of *The Chemical Physics of Solid Surfaces*, p. 39, Elsevier, 2001.

[31] B. Hammer, L. B. Hansen, and J. K. Nørskov, "Improved adsorption energetics within density-functional theory using revised perdew-burke-ernzerhof functionals," *Phys. Rev. B*, vol. 59, pp. 7413–7421, Mar 1999.

[32] J. P. Perdew, "Density functional theory and the band gap problem," *International Journal of Quantum Chemistry*, vol. 28, no. S19, pp. 497–523, 1985.

[33] J. P. Perdew, K. Burke, and M. Ernzerhof, "Generalized gradient approximation made simple," *Phys. Rev. Lett.*, vol. 77, pp. 3865–3868, Oct 1996.

[34] U. von Barth and L. Hedin, "A local exchange-correlation potential for the spin polarized case.," *Journal of Physics C: Solid State Physics*, vol. 5, p. 1629, jul 1972.

[35] B. Himmetoglu, A. Floris, S. de Gironcoli, and M. Cococcioni, "Hubbard-corrected DFT energy functionals: The LDA+U description of correlated systems," *International Journal of Quantum Chemistry*, vol. 114, no. 1, pp. 14–49, 2014.

[36] A. Rohrbach, J. Hafner, and G. Kresse, "Electronic correlation effects in transition-metal sulfides," *Journal of Physics: Condensed Matter*, vol. 15, p. 979, feb 2003.

[37] A. I. Liechtenstein, V. I. Anisimov, and J. Zaanen, "Density-functional theory and strong interactions: Orbital ordering in Mott-Hubbard insulators," *Phys. Rev. B*, vol. 52, pp. R5467–R5470, Aug 1995.

[38] S. L. Dudarev, G. A. Botton, S. Y. Savrasov, C. J. Humphreys, and A. P. Sutton, "Electron-energy-loss spectra and the structural stability of nickel oxide: An LSDA+U study," *Phys. Rev. B*, vol. 57, pp. 1505–1509, Jan 1998.

[39] M. Blume, R. E. Watson, and R. E. Peierls, "Theory of spin-orbit coupling in atoms I. Derivation of the spin-orbit coupling constant," *Proceedings of the Royal Society of London. Series A. Mathematical and Physical Sciences*, vol. 270, no. 1340, pp. 127–143, 1962.

[40] I. Dzyaloshinsky, "A thermodynamic theory of "weak" ferromagnetism of antiferromagnetics," *Journal of Physics and Chemistry of Solids*, vol. 4, no. 4, pp. 241–255, 1958.

[41] T. Moriya, "Anisotropic Superexchange Interaction and Weak Ferromagnetism," *Phys. Rev.*, vol. 120, pp. 91–98, Oct 1960.

[42] R. Karplus and J. M. Luttinger, "Hall Effect in Ferromagnetics," *Phys. Rev.*, vol. 95, pp. 1154–1160, Sep 1954.

[43] N. A. Sinitsyn, "Semiclassical theories of the anomalous hall effect," *Journal of Physics: Condensed Matter*, vol. 20, p. 023201, dec 2007.

[44] C.-Z. Chang, J. Zhang, X. Feng, J. Shen, Z. Zhang, M. Guo, K. Li, Y. Ou, P. Wei, L.-L. Wang, Z.-Q. Ji, Y. Feng, S. Ji, X. Chen, J. Jia, X. Dai, Z. Fang, S.-C. Zhang, K. He, Y. Wang, L. Lu, X.-C. Ma, and Q.-K. Xue, "Experimental Observation of the Quantum Anomalous Hall Effect in a Magnetic Topological Insulator," *Science*, vol. 340, no. 6129, pp. 167–170, 2013.

[45] S. Blügel and G. Bihlmayer, *Magnetism of Low-dimensional Systems: Theory*. John Wiley Sons, Ltd, 2007.

[46] M. Siemons and U. Simon, "Gas sensing properties of volume-doped $CoTiO_3$ synthesized via polyol method," *Sens. Actuators, B*, vol. 126, no. 2, pp. 595 – 603, 2007.

[47] R. E. Newnham, J. H. Fang, and R. P. Santoro, "Crystal structure and magnetic properties of $CoTiO_3$," *Acta Crystallographica*, vol. 17, pp. 240–242, Mar 1964.

[48] H. Watanabe, H. Yamauchi, and H. Takei, "Magnetic anisotropies in $MTiO_3$ (M = Co, Ni)," *J. Magn. Magn. Mater.*, vol. 15-18, pp. 549–550, 1980.

[49] K. Momma and F. Izumi, "*VESTA3* for three-dimensional visualization of crystal, volumetric and morphology data," *J. Appl. Crystallogr.*, vol. 44, pp. 1272–1276, Dec 2011.

[50] F. Schoofs, M. Egilmez, T. Fix, J. L. MacManus-Driscoll, and M. G. Blamire, "Structural and magnetic properties of $CoTiO_3$ thin films on $SrTiO_3$ (001)," *J. Magn. Magn. Mater.*, vol. 332, pp. 67–70, 2013.

[51] H. Raebiger, S. Bae, C. Echeverría-Arrondo, and A. Ayuela, "Control of hole localization in magnetic semiconductors by axial strain," *Phys. Rev. Materials*, vol. 2, p. 024402, Feb 2018.

[52] H. J. Kulik, "Perspective: Treating electron over-delocalization with the DFT+U method," *J. Chem. Phys.*, vol. 142, no. 24, p. 240901, 2015.

[53] F. Aguilera-Granja and A. Ayuela, "Magnetism and Distortions in Two-Dimensional Transition-Metal Dioxides: On the Quest for Intrinsic Magnetic Semiconductor Layers," *The Journal of Physical Chemistry C*, vol. 124, no. 4, pp. 2634–2643, 2020.

[54] S. A. Tolba, K. M. Gameel, B. A. Ali, H. A. Almossalami, and N. K. Allam, "The DFT+U: Approaches, Accuracy, and Applications," in *Density Functional Calculations* (G. Yang, ed.), ch. 1, Rijeka: IntechOpen, 2018.

[55] G. Kresse and J. Furthmüller, "Efficient iterative schemes for ab initio total-energy calculations using a plane-wave basis set," *Phys. Rev. B*, vol. 54, pp. 11169–11186, Oct 1996.

[56] G. Kresse and D. Joubert, "From ultrasoft pseudopotentials to the projector augmented-wave method," *Phys. Rev. B*, vol. 59, pp. 1758–1775, Jan 1999.

[57] T. Wakiyama, *Magnetic Anisotropy and Magnetostriction*, pp. 133–158. Berlin, Heidelberg: Springer Berlin Heidelberg, 1991.

[58] P. Bruno, "Tight-binding approach to the orbital magnetic moment and magnetocrystalline anisotropy of transition-metal monolayers," *Phys. Rev. B*, vol. 39, pp. 865–868, Jan 1989.

[59] S. Das, S. Voleti, T. Saha-Dasgupta, and A. Paramekanti, "XY magnetism, Kitaev exchange, and long-range frustration in the $J_{\text{eff}} = \frac{1}{2}$ honeycomb cobaltates," *Phys. Rev. B*, vol. 104, p. 134425, Oct 2021.

[60] P. Bruno, "Physical origins and theoretical models of magnetic anisotropy," *Magnetismus von Festkörpern und grenzflächen*, vol. 24, pp. 1–28, 1993.

[61] C. Kittel, *Introduction to Solid State Physics*. Wiley, 8 ed., 2004.

[62] G. Shirane, S. J. Pickart, and Y. Ishikawa, "Neutron diffraction study of antiferromagnetic $MnTiO_3$ and $NiTiO_3$," *J. Phys. Soc. Jpn.*, vol. 14, no. 10, pp. 1352–1360, 1959.

[63] G. Daalderop, P. Kelly, M. Schuurmans, and H. Jansen, "Magnetic anisotropy in Fe, Co and Ni," *J. Phys. Colloq.*, vol. 49, no. C8, pp. C8–93, 1988.

[64] G. H. O. Daalderop, P. J. Kelly, and M. F. H. Schuurmans, "First-principles calculation of the magnetocrystalline anisotropy energy of iron, cobalt, and nickel," *Phys. Rev. B*, vol. 41, pp. 11919–11937, Jun 1990.

[65] J. Enkovaara, A. Ayuela, L. Nordström, and R. M. Nieminen, "Magnetic anisotropy in Ni_2MnGa," *Phys. Rev. B*, vol. 65, no. 13, p. 134422, 2002.

[66] J. Enkovaara, A. Ayuela, L. Nordström, and R. M. Nieminen, "Structural, thermal, and magnetic properties of Ni_2MnGa," *J. Appl. Phys.*, vol. 91, no. 10, pp. 7798–7800, 2002.

[67] K. S. Novoselov, A. K. Geim, S. V. Morozov, D. Jiang, Y. Zhang, S. V. Dubonos, I. V. Grigorieva, and A. A. Firsov, "Electric Field Effect in Atomically Thin Carbon Films," *Science*, vol. 306, pp. 666–669, 2004.

[68] A. K. Geim and K. S. Novoselov, "The rise of graphene," *Nature Materials*, vol. 6, pp. 183–191, 2007.

[69] C. Gong, L. Li, Z. Li, H. Ji, A. Stern, Y. Xia, T. Cao, W. Bao, C. Wang, Y. Wang, *et al.*, "Discovery of intrinsic ferromagnetism in two-dimensional van der Waals crystals," *Nature*, vol. 546, no. 7657, pp. 265–269, 2017.

[70] B. Huang, G. Clark, E. Navarro-Moratalla, D. R. Klein, R. Cheng, K. L. Seyler, D. Zhong, E. Schmidgall, M. A. McGuire, D. H. Cobden, *et al.*, "Layer-dependent ferromagnetism in a van der Waals crystal down to the monolayer limit," *Nature*, vol. 546, no. 7657, pp. 270–273, 2017.

[71] N. D. Mermin and H. Wagner, "Absence of Ferromagnetism or Antiferromagnetism in One- or Two-Dimensional Isotropic Heisenberg Models," *Phys. Rev. Lett.*, vol. 17, pp. 1133–1136, 1966.

[72] K. R. Nikolaev, A. Y. Dobin, I. N. Krivorotov, W. K. Cooley, A. Bhattacharya, A. L. Kobrinskii, L. I. Glazman, R. M. Wentzovitch, E. D. Dahlberg, and A. M. Goldman, "Oscillatory Exchange Coupling and Positive Magnetoresistance in Epitaxial Oxide Heterostructures," *Phys. Rev. Lett.*, vol. 85, pp. 3728–3731, 2000.

[73] R. R. Gareev, D. E. Bürgler, M. Buchmeier, D. Olligs, R. Schreiber, and P. Grünberg, "Metallic-Type Oscillatory Interlayer Exchange Coupling across an Epitaxial FeSi Spacer," *Phys. Rev. Lett.*, vol. 87, p. 157202, 2001.

[74] M. N. Baibich, J. M. Broto, A. Fert, F. N. Van Dau, F. Petroff, P. Etienne, G. Creuzet, A. Friederich, and J. Chazelas, "Giant Magnetoresistance of (001)Fe/(001)Cr Magnetic Superlattices," *Phys. Rev. Lett.*, vol. 61, pp. 2472–2475, 1988.

[75] G. Binasch, P. Grünberg, F. Saurenbach, and W. Zinn, "Enhanced magnetoresistance in layered magnetic structures with antiferromagnetic interlayer exchange," *Phys. Rev. B*, vol. 39, pp. 4828–4830, 1989.

[76] X. W. Li, A. Gupta, T. R. McGuire, P. R. Duncombe, and G. Xiao, "Magnetoresistance and Hall effect of chromium dioxide epitaxial thin films," *Journal of Applied Physics*, vol. 85, no. 8, pp. 5585–5587, 1999.

[77] J. M. Taylor, A. Markou, E. Lesne, P. K. Sivakumar, C. Luo, F. Radu, P. Werner, C. Felser, and S. S. P. Parkin, "Anomalous and topological Hall effects in epitaxial thin films of the noncollinear antiferromagnet Mn_3Sn," *Phys. Rev. B*, vol. 101, p. 094404, 2020.

[78] A. Puthirath Balan, S. Radhakrishnan, C. F. Woellner, and et al., "Exfoliation of a non-van der Waals material from iron ore hematite.," *Nature Nanotech*, vol. 13, p. 602–609, 2018.

[79] S. Lany, "Semiconducting transition metal oxides," *Journal of Physics: Condensed Matter*, vol. 27, p. 283203, jun 2015.

[80] S. Lany, H. Raebiger, and A. Zunger, "Magnetic interactions of Cr−Cr and Co−Co impurity pairs in ZnO within a band-gap corrected density functional approach," *Phys. Rev. B*, vol. 77, p. 241201, Jun 2008.

[81] B. J. Morgan and G. W. Watson, "Polaronic trapping of electrons and holes by native defects in anatase TiO_2," *Phys. Rev. B*, vol. 80, p. 233102, Dec 2009.

[82] X. Huang, S. K. Ramadugu, and S. E. Mason, "Surface-Specific DFT + U Approach Applied to α-$Fe_2O_3(0001)$," *The Journal of Physical Chemistry C*, vol. 120, no. 9, pp. 4919–4930, 2016.

[83] L. Jiang, S. V. Levchenko, and A. M. Rappe, "Rigorous Definition of Oxidation States of Ions in Solids," *Phys. Rev. Lett.*, vol. 108, p. 166403, Apr 2012.

[84] G. Y. Gou, J. W. Bennett, H. Takenaka, and A. M. Rappe, "Post density functional theoretical studies of highly polar semiconductive $Pb(Ti_{1-x}Ni_x)O_{3-x}$ solid solutions: Effects of cation arrangement on band gap," *Phys. Rev. B*, vol. 83, p. 205115, May 2011.

[85] W. Kutzelnigg, "Book Review: Atoms in Molecules. A Quantum Theory. (International Series Monographs on Chemistry, Vol. 22). By R. F. W. Bader," *Angewandte Chemie International Edition in English*, vol. 32, no. 1, pp. 128–129, 1993.

[86] G. Henkelman, A. Arnaldsson, and H. Jónsson, "A fast and robust algorithm for Bader decomposition of charge density," *Computational Materials Science*, vol. 36, no. 3, pp. 354–360, 2006.

[87] Q. D. Gibson, H. Wu, T. Liang, M. N. Ali, N. P. Ong, Q. Huang, and R. J. Cava, "Magnetic and electronic properties of $CaMn_2Bi_2$: A possible hybridization gap semiconductor," *Phys. Rev. B*, vol. 91, p. 085128, Feb 2015.

[88] M. M. Piva, S. M. Thomas, Z. Fisk, J.-X. Zhu, J. D. Thompson, P. G. Pagliuso, and P. F. S. Rosa, "Putative hybridization gap in $camn_2bi_2$ under applied pressure," *Phys. Rev. B*, vol. 100, p. 045108, Jul 2019.

[89] C. Lane, M. M. Piva, P. F. S. Rosa, and J.-X. Zhu, "Competition between electronic correlations and hybridization in $camn_2bi_2$," 2021.

[90] W. Y. Liang, "Excitons," *Physics Education*, vol. 5, p. 226, jul 1970.

[91] G. H. Wannier, "The Structure of Electronic Excitation Levels in Insulating Crystals," *Phys. Rev.*, vol. 52, pp. 191–197, Aug 1937.

[92] Y.-M. Byun, J. Sun, and C. A. Ullrich, "Time-dependent density-functional theory for periodic solids: assessment of excitonic exchange–correlation kernels," *Electron. Struct.*, vol. 2, p. 023002, apr 2020.

[93] S. Kéna-Cohen, "Strong exciton-photon coupling in organic semiconductor microcavities," 01 2010.

[94] C. Zhang, H. Zhang, R. Wang, D. You, W. Wang, C. Xu, and J. Dai, "Exciton photoluminescence of $CsPbBr_3@SiO_2$ quantum dots and its application as a phosphor material in light-emitting devices," *Opt. Mater. Express*, vol. 10, pp. 1007–1017, Apr 2020.

[95] A. Swarnkar, R. Chulliyil, V. K. Ravi, M. Irfanullah, A. Chowdhury, and A. Nag, "Colloidal $CsPbBr_3$ Perovskite Nanocrystals: Luminescence beyond Traditional Quantum Dots," *Angewandte Chemie International Edition*, vol. 54, no. 51, pp. 15424–15428, 2015.

[96] H. Kim, S. Z. Uddin, N. Higashitarumizu, E. Rabani, and A. Javey, "Inhibited nonradiative decay at all exciton densities in monolayer semiconductors," *Science*, vol. 373, no. 6553, pp. 448–452, 2021.

[97] A. Miyata, A. Mitioglu, P. Plochocka, O. Portugall, J. T.-W. Wang, S. D. Stranks, H. J. Snaith, and R. J. Nicholas, "Direct measurement of the exciton binding energy and effective masses for charge carriers in organic–inorganic tri-halide perovskites," *Nature Physics*, vol. 11, pp. 582–587, Jul 2015.

[98] G. Onida, L. Reining, and A. Rubio, "Electronic excitations: density-functional versus many-body Green's-function approaches," *Rev. Mod. Phys.*, vol. 74, pp. 601–659, Jun 2002.

[99] S. Botti, F. Sottile, N. Vast, V. Olevano, L. Reining, H.-C. Weissker, A. Rubio, G. Onida, R. Del Sole, and R. W. Godby, "Long-range contribution to the exchange-correlation kernel of time-dependent density functional theory," *Phys. Rev. B*, vol. 69, p. 155112, Apr 2004.

[100] S. Sharma, J. K. Dewhurst, A. Sanna, and E. K. U. Gross, "Bootstrap Approximation for the Exchange-Correlation Kernel of Time-Dependent Density-Functional Theory," *Phys. Rev. Lett.*, vol. 107, p. 186401, Oct 2011.

[101] S. Botti, A. Schindlmayr, R. D. Sole, and L. Reining, "Time-dependent density-functional theory for extended systems," *Rep. Prog. Phys.*, vol. 70, p. 357, feb 2007.

[102] S. Rigamonti, S. Botti, V. Veniard, C. Draxl, L. Reining, and F. Sottile, "Estimating Excitonic Effects in the Absorption Spectra of Solids: Problems and Insight from a Guided Iteration Scheme," *Phys. Rev. Lett.*, vol. 114, p. 146402, Apr 2015.

[103] C. A. Ullrich and Z.-h. Yang, "Excitons in Time-Dependent Density-Functional Theory," pp. 185–217, Springer, Cham, 2014.

[104] Z.-h. Yang and C. A. Ullrich, "Direct calculation of exciton binding energies with time-dependent density-functional theory," *Phys. Rev. B*, vol. 87, p. 195204, May 2013.

[105] Y.-M. Byun and C. A. Ullrich, ""Assessment of long-range-corrected exchange-correlation kernels for solids: Accurate exciton binding energies via an empirically scaled bootstrap kernel"," *Phys. Rev. B*, vol. 95, p. 205136, may 2017.

[106] M. E. CASIDA, "Time-Dependent Density Functional Response Theory for Molecules," pp. 155–192, nov 1995.

[107] V. Turkowski, a. Leonardo, and C. a. Ullrich, "Time-dependent density-functional approach for exciton binding energies," *Phys. Rev. B*, vol. 79, no. 23, pp. 1–4, 2009.

[108] R. Resta, "Quantum-mechanical position operator in extended systems," *Phys. Rev. Lett.*, vol. 80, pp. 1800–1803, Mar 1998.

[109] B. Gu, N. H. Kwong, and R. Binder, "Relation between the interband dipole and momentum matrix elements in semiconductors," *Phys. Rev. B*, vol. 87, p. 125301, Mar 2013.

[110] Z.-h. Yang, F. Sottile, and C. A. Ullrich, "Simple screened exact-exchange approach for excitonic properties in solids," *Phys. Rev. B*, vol. 92, p. 035202, Jul 2015.

[111] J. Sun, J. Yang, and C. A. Ullrich, "Low-cost alternatives to the Bethe-Salpeter equation: Towards simple hybrid functionals for excitonic effects in solids," *Phys. Rev. Res.*, vol. 2, p. 013091, Jan 2020.

[112] J. Sun and C. A. Ullrich, "Optical properties of $CsCu_2X_3$ ($X = \mathrm{Cl}, \mathrm{Br}, \mathrm{and I}$): A comparative study between hybrid time-dependent density-functional theory and the Bethe-Salpeter equation," *Phys. Rev. Mater.*, vol. 4, p. 095402, Sep 2020.

[113] C. A. Ullrich, *Time-Dependent Density-Functional Theory: Concepts and Applications*. Oxford University Press, 12 2011.

[114] M. Casida and M. Huix-Rotllant, "Progress in Time-Dependent Density-Functional Theory," *Annual Review of Physical Chemistry*, vol. 63, no. 1, pp. 287–323, 2012. PMID: 22242728.

[115] E. Runge and E. K. U. Gross, "Density-functional theory for time-dependent systems," *Phys. Rev. Lett.*, vol. 52, pp. 997–1000, Mar 1984.

[116] R. van Leeuwen, "Mapping from densities to potentials in time-dependent density-functional theory," *Phys. Rev. Lett.*, vol. 82, pp. 3863–3866, May 1999.

[117] R. Del Sole and E. Fiorino, "Macroscopic dielectric tensor at crystal surfaces," *Phys. Rev. B*, vol. 29, pp. 4631–4645, Apr 1984.

[118] S. L. Adler, "Quantum Theory of the Dielectric Constant in Real Solids," *Phys. Rev.*, vol. 126, pp. 413–420, Apr 1962.

[119] N. Wiser, "Dielectric constant with local field effects included," *Phys. Rev.*, vol. 129, pp. 62–69, Jan 1963.

[120] A. Marini, C. Hogan, M. Grüning, and D. Varsano, "yambo: An ab initio tool for excited state calculations," *Computer Physics Communications*, vol. 180, no. 8, pp. 1392–1403, 2009.

[121] E. K. U. Gross and W. Kohn, "Local density-functional theory of frequency-dependent linear response," *Phys. Rev. Lett.*, vol. 55, pp. 2850–2852, Dec 1985.

[122] S. Rigamonti, S. Botti, V. Veniard, C. Draxl, L. Reining, and F. Sottile, "Estimating Excitonic Effects in the Absorption Spectra of Solids: Problems and Insight from a Guided Iteration Scheme," *Phys. Rev. Lett.*, vol. 114, p. 146402, Apr 2015.

[123] S. Baroni and R. Resta, "Ab initio calculation of the macroscopic dielectric constant in silicon," *Phys. Rev. B*, vol. 33, pp. 7017–7021, May 1986.

[124] M. L. Cohen and T. K. Bergstresser, "Band Structures and Pseudopotential Form Factors for Fourteen Semiconductors of the Diamond and Zinc-blende Structures," *Phys. Rev.*, vol. 141, pp. 789–796, Jan 1966.

[125] P. Giannozzi, S. Baroni, N. Bonini, M. Calandra, R. Car, C. Cavazzoni, D. Ceresoli, G. L. Chiarotti, M. Cococcioni, I. Dabo, A. D. Corso, S. de Gironcoli, S. Fabris, G. Fratesi, R. Gebauer, U. Gerstmann, C. Gougoussis, A. Kokalj, M. Lazzeri, L. Martin-Samos, N. Marzari, F. Mauri, R. Mazzarello, S. Paolini, A. Pasquarello, L. Paulatto, C. Sbraccia, S. Scandolo, G. Sclauzero, A. P. Seitsonen, A. Smogunov, P. Umari, and R. M. Wentzcovitch, "QUANTUM ESPRESSO: a modular and open-source software project for quantum simulations of materials," *J. Phys.: Condens. Matter*, vol. 21, p. 395502, sep 2009.

[126] J. Deslippe, G. Samsonidze, D. A. Strubbe, M. Jain, M. L. Cohen, and S. G. Louie, "BerkeleyGW: A massively parallel computer package for the calculation of the quasiparticle and optical properties of materials and nanostructures," *Comput. Phys. Commun.*, vol. 183, no. 6, pp. 1269 – 1289, 2012.

[127] Y.-H. Kim and A. Görling, "Excitonic Optical Spectrum of Semiconductors Obtained by Time-Dependent Density-Functional Theory with the Exact-Exchange Kernel," *Phys. Rev. Lett.*, vol. 89, p. 096402, Aug 2002.

[128] Y.-H. Kim and A. Görling, "Exact Kohn-Sham exchange kernel for insulators and its long-wavelength behavior," *Phys. Rev. B*, vol. 66, no. 3, p. 035114, 2002.

[129] R. Sundararaman and T. A. Arias, "Regularization of the Coulomb singularity in exact exchange by Wigner-Seitz truncated interactions: Towards chemical accuracy in nontrivial systems," *Phys. Rev. B*, vol. 87, p. 165122, Apr 2013.

[130] M. Parenteau, C. Carlone, and S. M. Khanna, "Damage coefficient associated with free exciton lifetime in GaAs irradiated with neutrons and electrons," *J. Appl. Phys.*, vol. 71, no. 8, pp. 3747–3753, 1992.

[131] M. Levinshtein, S. Rumyantsev, and M. S. Shur, "Properties of advanced semiconductor materials : GaN, AlN, InN, BN, SiC, SiGe," pp. 1–30, 2001.

[132] M. Feneberg, M. Röppischer, C. Cobet, N. Esser, J. Schörmann, T. Schupp, D. J. As, F. Hörich, J. Bläsing, A. Krost, and R. Goldhahn, "Optical properties of cubic GaN from 1 to 20 eV," *Phys. Rev. B*, vol. 85, p. 155207, Apr 2012.

[133] D. J. As, F. Schmilgus, C. Wang, B. Schöttker, D. Schikora, and K. Lischka, "The near band edge photoluminescence of cubic GaN epilayers," *Appl. Phys. Lett.*, vol. 70, no. 10, pp. 1311–1313, 1997.

[134] M. Jakobson, V. Kagan, R. Seisyan, and E. Goncharova, "Optical properties of "pure" CdS and metal-insulator-semiconductor structures on CdS at electrical operation," *J. Cryst. Growth*, vol. 138, no. 1, pp. 225–230, 1994.

[135] J. Voigt, F. Spiegelberg, and M. Senoner, "Band parameters of CdS and CdSe single crystals determined from optical exciton spectra," *Phys. Status Solidi B*, vol. 91, no. 1, pp. 189–199, 1979.

[136] J. F. Muth, J. H. Lee, I. K. Shmagin, R. M. Kolbas, H. C. Casey, B. P. Keller, U. K. Mishra, and S. P. DenBaars, "Absorption coefficient, energy gap, exciton binding energy, and recombination lifetime of GaN obtained from transmission measurements," *Appl. Phys. Lett.*, vol. 71, no. 18, pp. 2572–2574, 1997.

[137] P. Lautenschlager, M. Garriga, S. Logothetidis, and M. Cardona, "Interband critical points of GaAs and their temperature dependence," *Phys. Rev. B*, vol. 35, pp. 9174–9189, Jun 1987.

[138] R. A. R. Leute, M. Feneberg, R. Sauer, K. Thonke, S. B. Thapa, F. Scholz, Y. Taniyasu, and M. Kasu, "Photoluminescence of highly excited AlN: Biexcitons and exciton-exciton scattering," *Appl. Phys. Lett.*, vol. 95, no. 3, p. 031903, 2009.

[139] R. Haensel, G. Keitel, E. E. Koch, M. Skibowski, and P. Schreiber, "Reflection Spectrum of Solid Argon in the Vacuum Ultraviolet," *Phys. Rev. Lett.*, vol. 23, pp. 1160–1163, Nov 1969.

[140] D. M. Roessler and W. C. Walker, "Electronic Spectrum and Ultraviolet Optical Properties of Crystalline MgO," *Phys. Rev.*, vol. 159, pp. 733–738, Jul 1967.

[141] "The Elk Code." http://elk.sourceforge.net/.

[142] S. Bloom, "Band structures of gan and ain," *Journal of Physics and Chemistry of Solids*, vol. 32, no. 9, pp. 2027–2032, 1971.

[143] J. D. Ng and A. Danner, "Pseudopotential form factors and electronic band structures for AlAs, AlP, BAs, BP, 3C-SiC, and cubic-GaN," *Physica Scripta*, vol. 96, p. 055801, feb 2021.

[144] C.-Y. Fong, "Empirical Pseudopotential Method for Electronic Band Structure Calculations in Insulators," 1968.